Usefulness of quantitative susceptibility mapping (QSM) for the diagnosis of Parkinson's disease

Shingo Kakeda[1], Yu Murakami[1], Keita Watanabe[1], Issei Ueda[1], Atushi Ogasawara[1], Junji Moriya[1], Satoru Ide[1], Koichiro Futatsuya[1], Toru Sato[1], Kazumasa Okada[2], Takenori Uozumi[2], Sadatoshi Tsuji[2], Tian Liu[3], Yi Wang[3], Yukunori Korogi[1]

[1]Department of Radiology, University of Occupational and Environmental Health, . School of Medicine, 1-1 Iseigaoka, Yahatanishi-ku, Kitakyushu 807-8555, Japan
[2]Department of Neurology, University of Occupational and Environmental Health, School of Medicine
[3]Departments of Biomedical Engineering and Radiology, Cornell University, New York, USA

ABSTRACT

OBJECTIVE: Quantitative susceptibility mapping (QSM) and R2* mapping were compared to discriminate between patients with Parkinson's disease (PD) and controls and assessed the diagnostic accuracy of the two imaging techniques.

METHODS: Our institutional review board approved this study. The study population consisted of 21 PD patients and 21 age- and sex-matched controls. Two radiologists measured the QSM values and R2* rates in 7 brain structures (frontal white matter, thalamus, putamen, caudate nucleus, pallidum, substantia nigra, and red nucleus) of all participants.

RESULTS: The QSM values and R2* rates of the substantia nigra were significantly higher in PD patients ($p<0.01$); measurements in other brain regions did not differ significantly between patients and controls. For the discrimination of PD patients from controls, ROC analysis suggested that the optimal cutoff values for the substantia nigra, based on the Youden index, were >210 for QSM and >144 for R2*. The sensitivity, specificity, and accuracy of QSM were 90% (19 of 21), 86% (18 of 21), and 88% (37 of 42), respectively; for R2* mapping they were 81% (17 of 21), 52% (11 of 21), and 67% (28 of 42). Pairwise comparisons showed that A_z was significantly larger for QSM than R2* mapping (0.91 vs. 0.69, $p<0.05$).

CONCLUSION: QSM is more sensitive than R2* mapping for the detection of pathological changes in the substantia nigra. Our findings suggest QSM as a viable tool for the diagnosis and assessment of PD.

Discriminating brain microbleeds using phase contrast MRI in a multicentre clinical setting

Takoua Kaaouana[1,2], Ludovic de Rochefort[3], Thomas Samaille[1,2], Nathalie Thierry[4], Geneviève Chêne[4], Christine Delmaire[5], Didier Dormont[1], Marie Chupin[1]

[1]*CRICM, UPMC URMR_S975, INSERM U975, CNRS UMR7225, ICM, Inria, Paris, France,* [2]*CATI, Paris, France,* [3]*Univ. Paris-Sud, CNRS IR4M UMR8081, Orsay, France,* [4]*U897, INSERM, Bordeaux, France,* [5]*Neuroradiology department, CHRU Roger Salengro, Lille, France*

Background/Purpose: Brain microbleeds (BMBs) have emerged as a new imaging marker of small vessel diseases, mainly hypertensive vasculopathy and cerebral amyloid angiopathy, and they may have a crucial role in degenerative pathology such as Alzheimer's disease [1]. Composed of hemosiderin, BMBs can be efficiently detected with MRI sequences sensitive to magnetic susceptibility (e.g. gradient recalled echo T2*W images). Nevertheless, identification remains challenging because of confounding structures and lesions. Most T2*W hyposignals result from local magnetic field inhomogeneity and can be identified either as BMBs, veins or brain micro-calcifications (BMCs). Differential diagnosis of BMBs and BMCs requires an additional CT scan. Quantitative susceptibility mapping techniques were proposed to discriminate between diamagnetic and paramagnetic structures [2], but they require a full 3D dataset and a complex post-processing. Here, we introduce a fast 2D phase processing technique including unwrapping and harmonic filtering applicable on multicenter data acquired in standardized clinical setting to discriminate between paramagnetic BMBs and diamagnetic BMCs.

Methods: Experiments were performed on 11 patients with BMBs from the multicentre MEMENTO cohort. 2D GRE sequences from four Siemens and one Philips 3T systems were used to acquire 2.5mm thick axial brain slices, with 1mm×1mm in plane resolution and TR/TE/FA=650ms/20ms/20°.
To filter the field from background effects, we used a 2D approximation of harmonic filtering [3]. The field inside the brain, B, can be decomposed as the sum of internal variations, B_{in}, and variations induced by external sources, B_{out}. From Maxwell equations, the external field is harmonic inside the brain ($\Delta B_{out}=0$) and $\Delta B=\Delta B_{in}$. Here, to isolate local variations, a harmonic 2D filter was used. Slice-by-slice phase unwrapping was performed by forcing the point by point difference between]-π, π] when calculating the gradients, and the divergence was then calculated to get ΔB. The laplacian was set to 0 outside a mask generated with SPM imposing proper boundary conditions. Integration to recover B_{in} was then done in Fourier domain using a regularized inverse 2D Laplace filter (Tikhonov regularization, parameter set to 0.002).

Results: Phase wraps were efficiently removed. Harmonic 2D filter gets rid of background effects and preserves local phase variation. SPM masking prior to integration allows limiting artifacts at the brain boundaries. Both BMBs and mimicking BMCs are dot-like susceptibility inclusions detectable on the magnitude image that create dipole-like magnetic field patterns in the internal field map (Fig.1). For paramagnetic inclusions such as BMBs, dipolar effect is seen ring-like structure with a sign inversion (- + -), whereas it is (+ - +) for diamagnetic inclusions such as BMCs (Fig.2).

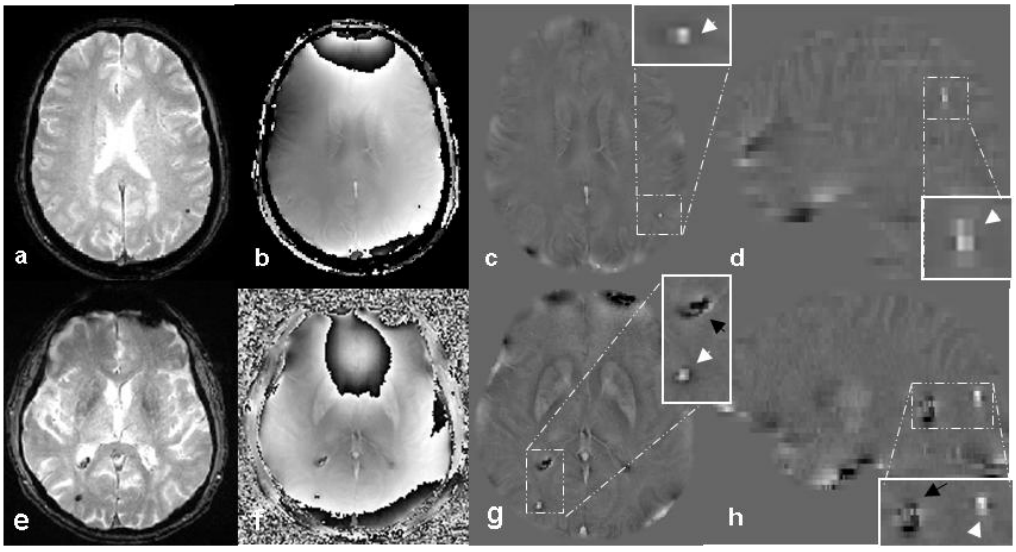

Fig. 1: Philips (a,b,c,d) and Siemens (e,f,g,h) sample cases. Magnitude image (a,e), native phase image (b,f), and internal field map; axial (c,g) and sagittal (d,h). Zoom in white rectangle showing a dipolar pattern BMB (white arrow) and a physiologic calcification of the choroid plexus (black arrow).

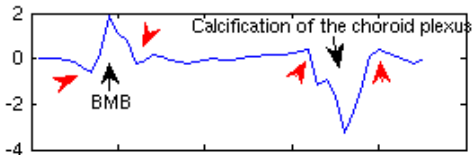

Fig.2: Sign inversion for either side of BMB and the calcification

Conclusion: We have shown that the 2D harmonic filter is keeping dipole patterns visible. It additionally allows removing different shimming at acquisition and/or reconstruction from multicenter datasets. Internal field map filtered in this way may provide an efficient tool for clinicians to detect BMBs and discriminate them from BMCs. Their fast calculation proved robust on phase images from 2D T2* clinical acquisitions.

References: 1: Greenberg S, et al. Neurology 2009, 8(2):165:174**.** 2: de Rochefort *et al*. MRM 2010 63:194. 3. de Rochefort *et al*. ISMRM 2010 4997.

Characterizing Cerebral Cavernous Malformation with Quantitative Susceptibility Mapping: A Feasibility Study

Huan Tan[1], Ying Wu[1], Abdul Ghani Mikati[2], Tian Liu[3], Yi Wang[3], Pottumarthi V. Prasad[1,2], Issam A. Awad[2], Robert R. Edelman[1,4]

[1.] NorthShore University HealthSystem, Evanston, IL [2.] The University of Chicago Pritzker School of Medicine, Chicago, IL [3.] Weill Cornell Medical College, New York, NY [4.] Northwestern University Feinberg School of Medicine, Chicago, IL

Background/Purpose: Cerebral cavernous malformation (CCM) is a common hemorrhagic vascular anomaly of the human brain, characterized by repetitive lesional hemorrhages. The CCM lesions contain iron-rich hemoglobin breakdown products that can be depicted by magnetic resonance (MR) with susceptibility weighted imaging (SWI). While SWI can assess lesion counts with great sensitivity, it does not evaluate changes in iron content within individual lesions[1]. A new MRI technique, quantitative susceptibility mapping (QSM)[2], allows quantitative evaluations of intra-lesional susceptibility changes related to leakage of iron-containing blood products. In the present study, we performed QSM in patients with CCM to characterize lesion burden in terms of lesion count and susceptibility values. The long term goal is to evaluate the potential of QSM as a new quantitative marker for monitoring CCM lesion progression and responses to treatments.

Methods: A total of 14 CCM patients were recruited for the study with institutional review board approval. 11 solitary and 3 familial cases were identified in our patient population. All imaging was performed on a Siemens 3T scanner (MAGNETOM Verio, Siemens Healthcare, Erlangen, Germany) with a 12 channel phased array head coil. A single three dimensional, multi-echo, T2*-weighted, spoiled gradient echo sequence was used for data collection for both SWI and QSM reconstruction. The imaging parameters were as follows: axial imaging plane with full brain coverage; 8 echo times with uniform spacing; TE [min, max] = [3.6, 45] ms; TR = 55 ms; flip angle = 15°; bandwidth = 240 Hz/Pixel; field of view = 240 mm, acquisition matrix = 256 x 256; slice thickness = 1.5 mm; number of slab encodings = 80. Data acquisition is accelerated by a factor of 2 with iPAT. The imaging time was 7 min 40 sec. Data reconstruction was performed offline. The QSM images were reconstructed with 4-8 echoes using a morphology-enabled dipole inversion (MEDI) algorithm[3]. Data from the longest echo time (TE = 45ms) was used for SWI reconstruction. Susceptibility values were measured using manually defined ROI masks.

Results: Figure 1 illustrates a solitary/sporadic and a multiple/familial CCM case. The CCM lesion can be identified on both QSM and SWI. 100% lesions was identified on QSM and SWI for sporadic cases, and 91% for familial cases, based on expert review. Table 1 shows the mean susceptibility values from five known iron-rich regions (without any known abnormality / presence of the CCM lesion) of the brain, which matched closely with the previous study in healthy volunteers[3]. The mean susceptibility values in CCM lesions varied from 0.28 – 0.75 ppm with an average of 0.46 ± 0.14 ppm across all patients. The total susceptibility varied from 48 - 2854 ppm·mm^3 with an average of 727 ppm·mm^3 across all patients. A linear relationship was observed between estimated lesion volume and total susceptibility, and but not between lesion volume and mean susceptibility (Figure 2). There was no significant difference in susceptibility calculations as a function of echo train length, suggesting the scan time may be shortened to 4 min 6 sec.

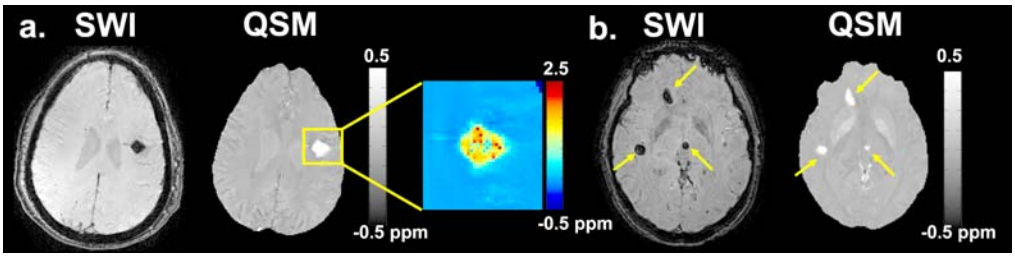

Figure 1.Examples of QSM and SWI from a sporadic (a) and a familial (b) CCM case. The susceptibility distribution within the solitary CCM lesion is magn`ified and shown in color. Larger lesions in the familial cases are highlighted by arrows.

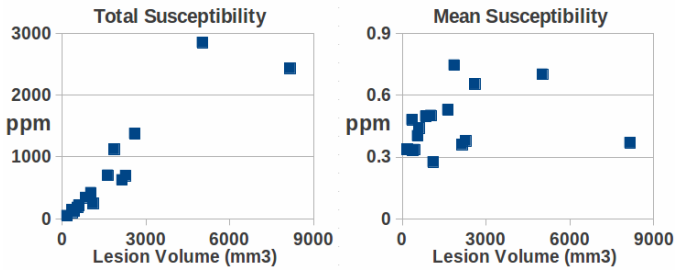

Figure 2. Scatter plots of estimated lesion volume and total / mean susceptibility.

Iron-Rich Region	Measured Susceptibility (ppm)	Literature[3] (ppm)
Red Nucleus	0.102 ± 0.01	0.077 ± 0.05
Putamen	0.096 ± 0.03	0.082 ± 0.02
Caudate Nucleus	0.083 ± 0.02	0.089 ± 0.02
Substanita Nigra	0.135 ± 0.02s	0.115 ± 0.03
Globus Pallidus	0.157 ± 0.03	0.187 ± 0.02

Table 1. Comparison between susceptibility measured in known iron-rich brain region and published literature[3].

Conclusion: Our preliminary results have demonstrated the QSM's ability to provide quantitative evaluation of CCM lesions. QSM offers a complementary strategy aiming to quantify local iron deposit within individual lesions, which is a potentially clinically useful measure of CCM lesion progression. In addition, QSM was previously shown to have reduced variation in terms of lesion size over a wide spectrum of echo times, when compared to SWI (4). Together, SWI and QSM may serve as novel imaging biomarkers to provide accurate lesion counts and allow long-term monitoring of CCM disease progression.

References: 1) de Champfleur et al. Neurosurgery, 2011. 2) Schweser et. al. Med Phys, 2010. 3) Liu et al. Magn Reson Med, 2011. 4). Liu et al. Radiology, 2012.

3D Model of the Optic Radiation using Susceptibility Weighted Imaging

R. Ehsan Hamtaei, BS and E. Mark Haacke, PhD
Wayne State University

Introduction: Up to 40% of patients with temporal lobe epilepsy (TLE) fail to respond to drug therapy or anterior temporal lobe resection (ATLR) is the most common operation and effective treatment [1]. The benefits of ATLR surgery must be weighed against the possible adverse effects including damage to white matter (WM) connections. The optic radiation is a key WM fiber tract which conveys visual information from the lateral geniculate nucleus (LGN) to the primary visual cortex. Fibers which represent the inferior visual field pass directly posteriorly from the LGN, whereas the ones which represent the superior visual field first pass anteriorly over the roof of the temporal horn of the lateral ventricle before turning backward (Meyer's loop) [2]. During ATLR, Meyer's loop is vulnerable to damage with between 48% and 100% of patients developing a postoperative visual field deficit due to contralateral superior quadrantanopia that precludes driving in up to 50% of patients even if seizure free [1]. The optic radiation is often difficult to find on conventional MRI. Currently, diffusion tensor imaging is being used along with tractography to trace the optic radiation and Meyer's loop to preserve it during surgery. The potential of susceptibility weighted imaging (SWI) to delineate the optic radiation has been discussed at 7T [3], at 3T [4] and with phase images [5]. In this work, we propose an alternate means to locate the optic radiation and identify it's different layers using both phase and SWI. Eventually a 3D model of the optic radiation can be created and complemented with local structural information for landmark purposes.

Methods: A male volunteer was scanned in a 3T Siemens VERIO scanner with a 3D double echo (TE1=6ms, TE2=20ms) gradient echo sequence with the following parameters: TR=29ms, FA=15^{o}, a resolution of 0.5x0.5x1 mm^{3} and an acquisition time of roughly 8mins. High pass filtered phase images were used to enhance the magnitude susceptibility contrast using the SWI technique [6]. Processed images of both echo times were reconstructed in three axial, coronal and sagittal planes separately. The optic nerves and the eyes were extracted in the axial plane using the first echo (TE=6ms) images. The optic radiation was extracted from the sagittal plane manually using the second echo (TE=20ms) images and a series of slices and 3D view (using VolView 3.4) showing the eyes, optic nerves and optic radiation tracts was created.

Results: In this work, we showed the potential of SWI for depicting the layered anatomical structure of the optic radiation. We created a 3D model of the optic radiation along with the optic nerves using only SWI images in order to show the feasibility of SWI for clinical applications such as planning surgery for epilepsy patients. We calculated the T2* value of the optic radiation tract to be 45ms ±4ms which is different than the surrounding white matter, SLF (Superior Longitudinal Fasciculus), which has a T2* value of 56ms ±4ms. Our calculations at 3T agree with those in previous reports [7].

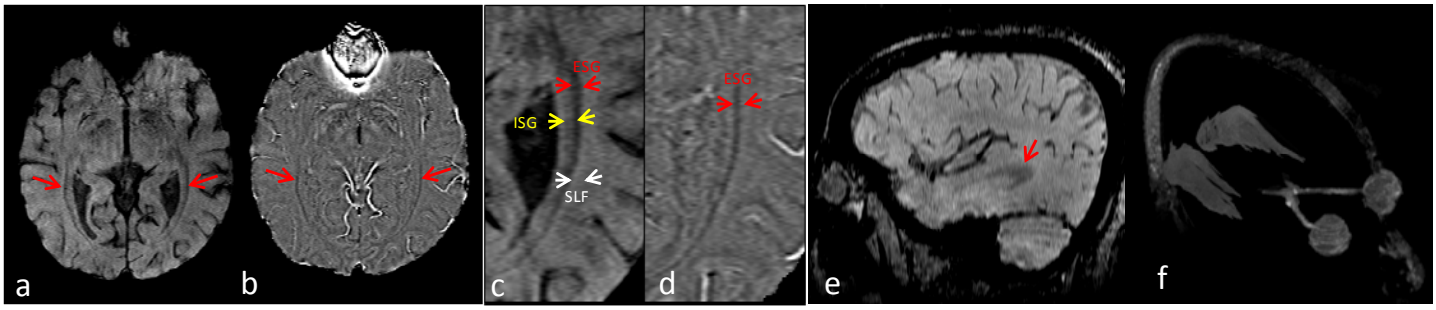

Figure 1. Red arrows show the optic radiation as a dark band in (a) magnitude image and (b) high pass filtered phase image. (c) and (d) show the zoomed SWI processed magnitude and high-pass filtered phase images respectively, showing the layered structure of the optic radiation. The yellow arrows show the layer known as internal sagittal stratum (ISG) and the red arrows show the external sagittal stratum (ESG) and it's surrounding white matter known as superior longitudinal fasciculus (SLF) [8]. The phase image shows the external sagittal stratum with excellent contrast. (e) is the sagittal view of the magnitude image, showing the course of the optic radiation tract. (f) shows a 3D representation of the optic radiation tracts on both sides along with the eyes and the optic nerves.

Discussion and Conclusions: There are different hypotheses about the possible sources of fiber bundle contrast in WM. The optic radiation fiber bundle not only shows a strong contrast in T2* weighted images with relatively lower T2* values compared with surrounding WM, but behaves differently in phase images. The current belief is that the myelin content, fiber micro-structure and orientation are the main contributors to the optic radiation contrast. At this point, the structure extraction is done manually. However, with the excellent contrast of the optic radiation tract and the well known structure of the optic nerves available in the data, this process should be able to be automated in the future. We expect these results to be a means to validate the DTI processing results and provide new insight into the optic radiation structure itself.

References: 1) Winston et al, Ann Neurol, 2012. 71(3): p. 334-41.; 2) Meyer, A. et al, Trans. Ass. Am. Phys., 1907. 22, 7—16; 3) Li et al, Neuroimage, 2006. 32(3): p. 1032-40; 4) Mori, N. et al, Invest Radiol, 2009. 44(3): p. 140-5; 5) Ide et al, Acad Radiol, 2012. 19(10): p. 1283-9; 6) Haacke et al, Magnetic Resonance in Medicine, 2004(52): p. 612–618; 7) Li et al, Magn Reson Med, 2009. 62(6): p. 1652-7. 8) Kitajima et al, AJNR Am J Neuroradiol, 1996. 17(7): p. 1379-83.

Feasibility of In vivo Quantitative Susceptibility Mapping (QSM) in the Kidneys

Huan Tan[1], Jon Thacker[2], Tian Liu[3], Yi Wang[3], Pottumarthi V. Prasad[1,4]

[1.] NorthShore University HealthSystem, Evanston, IL [2.] Northwestern University, Evanston, IL [3.] Weill Cornell Medical College, New York, NY [4.] The University of Chicago Pritzker School of Medicine, Chicago, IL

Introduction: Quantitative susceptibility mapping (QSM) offers a novel anatomical contrast proportional to the underlying susceptibility of the tissue[1,2]. The majority of the QSM applications have been in the brain as a result of the lengthy 3D multi-echo gradient echo (mGRE) acquisition. In this study, we have implemented a cross-pair prospective navigator technique to allow 3D mGRE acquisition of the kidney during free-breathing.

Methods: The cross-pair navigator consists of a pair of selective 90° and 180° radio frequency (RF) pulses resulting in a 1-D spin-echo projection. Only spins in the intersecting region of the two RF pulses (Figure 1a), excited by the 90° and refocused with the 180° RF, contribute to the navigator signal. The navigator was positioned over the right hemi-diaphragm (Figure 1b). Special precautions were taken to prevent the RF planar slabs from intersecting the kidneys. The data collection and navigator acquisition occurred within the same TR. Only data collected within the user-specified acceptance window was used in the final reconstruction. An example of a 20 sec navigator profile is shown in Figure 1c. The navigator parameters were: field of view = 400mm, acceptance window = 4mm, search window = 30mm, RF band thickness = 10mm.

Data were acquired in 7 healthy volunteers with the approval from our institutional review board. Two subjects received Furosemide (Lasix), a diuretic that improves the renal oxygenation. All experiments were performed on a 3T MRI system (MAGNETOM Verio, Siemens Healthcare, Erlangen, Germany) equipped with high performance gradient coils (45 mT/m maximum gradient strength, 200 mT/m/ms slew rate). The body and spine phased array coil were used for data acquisition.

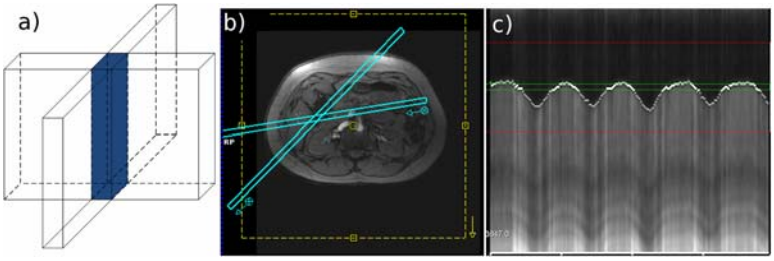

Figure 1.a) cross-pair navigator RF illustrations. b) navigator position. c) a 20-second navigator profile.

The QSM acquisition was performed using a 3D T2*-weighted, multi-echo spoiled gradient echo sequence. Full kidney coverage was achieved in either coronal or axial plane. Eight echoes were acquired with even spacing. The imaging parameters were: TE [min, max] = [4.03, 22.99] ms; TR = 78 ms; flip angle = 15°; bandwidth = 781 Hz/Pixel; field of view = 360 mm, acquisition matrix = 256x256; slice thickness = 2.5 mm; number of slab encodings = 24 - 48; iPAT = 2; 6/8 Partial Fourier along the slab encoding direction. The scan time ranged from 6 to 10 minutes depending on the subject's respiratory pattern. The QSM images were reconstructed offline using a morphology-enabled dipole inversion (MEDI) algorithm[3].

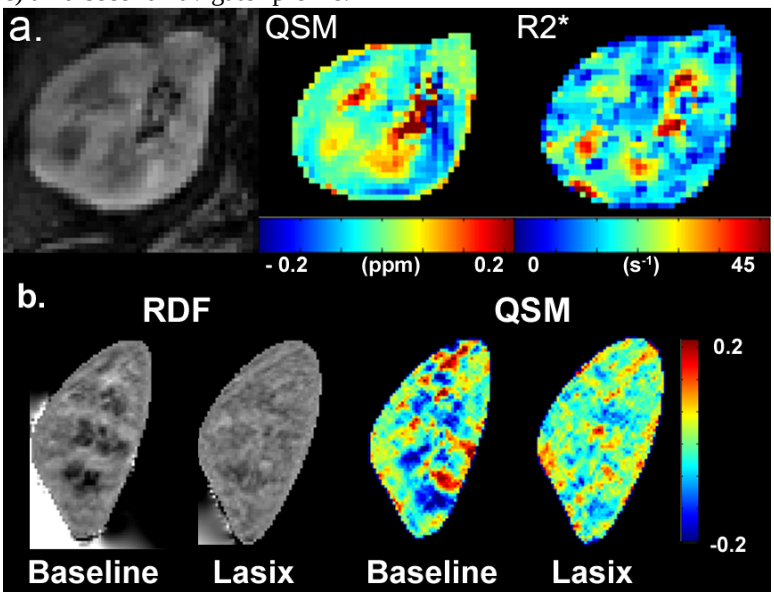

Figure 2. Preliminary renal QSM results in a healthy volunteer. a) Magnitude, QSM and R2* maps. b) Relative difference field (RDF) and QSM images from the furosemide challenge study.

Results: A representative single slice from the data in a healthy male volunteer (age of 50) is illustrated in Figure 2a: the magnitude (TE = 9.69ms), QSM and R2* maps are shown from left to right. Similar cortical-medullary contrast can be observed across all images. Higher susceptibility values were observed in the medulla than the cortex. Figure 2b illustrates a representative slice of the subject who underwent the furosemide challenge. Changes observed on the local field maps (RDF)[4] following furosemide suggest reduced susceptibility effect. QSM also showed differences pre- and post-furosemide. However, the spatial distribution of the local susceptibility values did not correlate with the cortical-medullary contrast seen on the magnitude / RDF image, which requires further investigation.

Conclusions: We have demonstrated the preliminary feasibility of obtaining QSM maps of the kidney using a prospective navigator-gated approach. Different susceptibility values were observed consistent with the renal anatomy. The preliminary studies with furosemide suggest that RDF maps may be sensitive to susceptibility difference between renal medulla and cortex which may be related to local blood oxygenation (BOLD effect). Further studies are necessary to fully validate this. The acquisition was affected by flow in renal vessels and off-resonance effects due to bowel gas.

Reference: 1) Shmueli et al. Magn Reson Med. 2009. 2) Rochefort et al. Magn Reson Med. 2010. 3) Liu et al. Magn Reson Med. 2011. 4) Liu et al. NMR Biomed. 2011.

Toward Probing Myocardial Microstructure Using Susceptibility Sensitized MRI of the Human Heart at 7.0 T: Assessment and Implications of Static Magnetic Field Variations

Till Hülnhagen[1], Fabian Hezel[1], Thoralf Niendorf[1,2]

[1]Berlin Ultrahigh Field Facility (B.U.F.F.), Max-Delbrueck Center for Molecular Medicine, Berlin, Germany, [2]Experimental and Clinical Research Center, a cooperation of the Charité Medical Faculty and the Max-Delbrueck Center for Molecular Medicine, Berlin, Germany

Introduction

Susceptibility weighted imaging (SWI) has attracted substantial research interest including the recent progress in fiber orientation tracking of the brain [1-4]. Recognizing this success it is conceptually appealing to extend research into the myocardial microstructure using SWI. Today, diffusion tensor imaging (DTI) is commonly used as a probe of myocardial microstructure. In vivo DTI of the heart remains challenging due to its propensity to cardiac motion [5, 6]. Myocardial fiber tracking using SWI holds the promise to be less sensitive to bulk motion versus diffusion weighted MR of the myocardium [7, 8]. *Ex vivo* MR microscopy of the isolated rat heart demonstrated that SWI provides an insight into the complex architecture of the heart musculature [9]. Because of the linear relationship between magnetic field strength (B_0) and microscopic susceptibility [10-12] it is conceptually appealing to pursue myocardial SWI at ultrahigh magnetic fields. Realizing the challenges and opportunities of SWI of the human heart in equal measure this work examines the basic feasibility of myocardial T_2* mapping at 7.0 T. To meet this goal, B_0 inhomogeneities across the heart are carefully examined at 7.0 T. This is essential to make sure that the susceptibility weighting is not dominated by macroscopic B_0 field inhomogeneities but rather by microscopic B_0 susceptibility gradients.

Methods

Volunteer experiments (n=8) were conducted using a 7.0 T whole body MR scanner (Magnetom, Siemens Healthcare, Erlangen, Germany). A 16 channel transceiver array tailored for cardiac MR was used for transmission and excitation [13]. Volume selective shimming was applied. For this purpose first and second order shim currents were calculated based on a cardiac triggered B_0 field map that was obtained as an axial stack covering the whole heart with a multi-echo gradient echo technique (TE=2.04ms and 4.08ms, matrix size=96x72, 18 slices). The shim volume was adjusted to cover ventricles and atria in the 4 chamber view together with a stack of short axis views of the heart. For myocardial T_2* mapping a cardiac triggered multi echo gradient echo technique ((TE=2.04-10.20)ms, spatial resolution=(1.4x1.4x4.0)mm^3) was used. For cardiac triggering a MR stethoscope (MRI.TOOLS GmbH,Berlin,Germany) was employed.

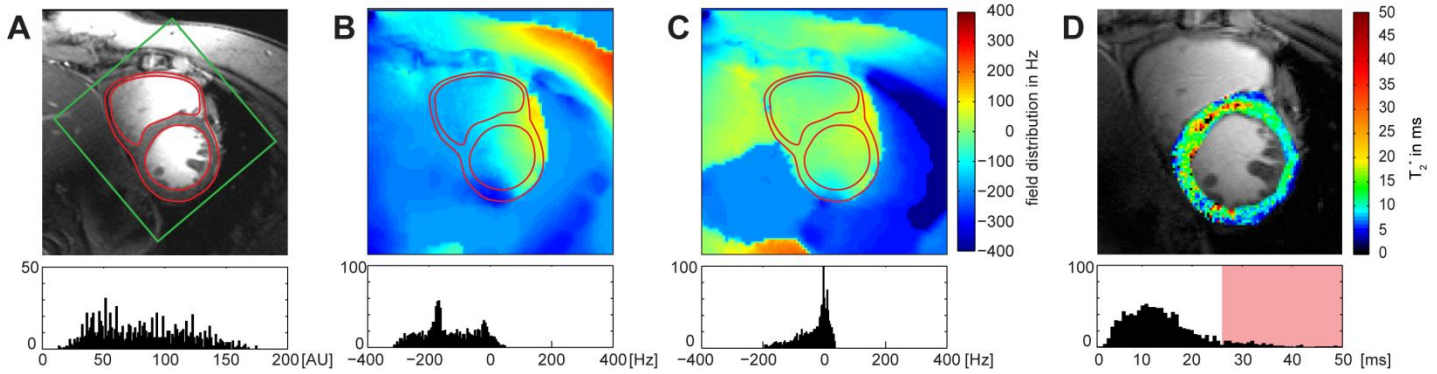

Figure 1: **A)** Mid-ventricular short axis view of the heart illustrating the positioning of the volume for volume selective shimming (marked in green) and **histogram of signal intensity in the left-ventricular myocardium B)** B_0 field map and **histogram of field distribution across left ventricle** after global shimming **C)** B_0 field map and **histogram of field distribution across left ventricle** after volume selective shimming **D)** Myocardial T_2*-map of a mid-ventricular short axis view of the human heart derived from susceptibility weighted imaging at 7.0 T together with a **histogram of T_2* values**. Please note the changes in T_2* in the septum (values shaded red in histogram).

Results

Fig. 1B and C show B_0-maps derived from a short axis view of the human heart after global and volume selective shimming. Global shimming revealed a mean peak-to-peak B_0 difference of approximately 400 Hz for a four chamber view and 300 Hz for a mid-ventricular short axis view. Volume selective shimming afforded a mean peak-to-peak B_0 difference of approximately 80 Hz across the entire heart for a four chamber view and a mid-ventricular short axis view, which is similar to the frequency variation previously reported for 3.0 T [14]. For myocardial anterior, anterolateral and inferoseptal segments a mean in-plane B_0 gradient of approximately 3Hz/mm was obtained which translates into an through-plane B_0 dispersion of approximately 12Hz/voxel for a 4mm slice thickness. This B_0 gradient implies that macroscopic intravoxel dephasing effects are of minor effect for the TE range used for T_2* imaging. Fig. 1D depicts a high spatial resolution T_2* map of a mid-ventricular short axis view which indicates the high sensitivity of susceptibility mapping at 7.0 T by visualizing differences in T_2* between endocardial and epicardial layers of the myocardium, which are pronounced for the septum.

Conclusions

Our results underscore the challenges of cardiac SWI at 7.0 T due to the propensity to macroscopic susceptibility artifacts, but demonstrate that these issues can be offset by using tailored shimming techniques together with dedicated acquisition schemes. The peak-to-peak frequency variation across the heart reported in this work suggests that cardiac SWI at 7.0 T is not dominated by macroscopic susceptibility gradients which provides encouragement for myocardial SWI at ultrahigh fields. Obviously, the use of even thinner slices and reduction in voxel size would further reduce the residual impact of through-plane gradients and intra-voxel dephasing B_0 gradients. To meet this goal we pushed the envelope by using a slice thickness as thin as 2.5mm together with an in-plane resolution of 1.1x1.1mm^2 for myocardial T_2*mapping. This slice thickness and in-plane resolution is afforded by the SNR advantage inherent to 7.0T. The corresponding voxel size is by a factor of eight smaller than commonly used for myocardial T_2* mapping at 1.5T and 3.0T. To conclude, since the susceptibility effects depend on the tilt angle between myocardial fibers and the external magnetic field strength [15-18] , SWI at 7.0 T holds the promise to contribute to explorations into *in vivo* visualization of myocardial fibers or into the examination of helical angulation of myocardial fibers [19].

References: [1] Langkammer et al. (2012) Neuroimage 62(3):1593, [2] Duyn et al. (2007) Proc Natl Acad Sci U S A 104(28):11796, [3] Lee et al. (2011) Neuroimage 57(1):225, [4] Deistung et al. (2013) Neuroimage 65:299, [5] Mekkaoui et al. (2012) JCMR 14:70, [6] Nielles-Vallespin et al. (2012) MRM, [7] Reese et al. (1995) MRM 34(6):786, [8] Wu et al. (2006) Circulation 114(10):1036, [9] Köhler et al. (2003) MRM 49(2):371, [10] Turner et al. (1993) MRM 29(2):277, [11] van der Zwaag et al. (2009) Neuroimage 47(4):1425, [12] Donahue et al. (2011) NMR Biomed 24(1):25, [13] Thalhammer et al. (2012) J Magn Reson Imaging 36(4):847, [14] Schaer et al. (2010) MRM 63(2):419, [15] Ogawa et al. (1993) Biophys J 64(3):803, [16] Reeder et al. (1998) MRM 39(6):988, [17] Ziener et al. (2012) Magn Reson Imaging 30(4):540, [18] Ziener et al. (2012) Phys Rev E Stat Nonlin Soft Matter Phys 85(5 Pt 1):051908, [19] Reichenbach et al. (2001) NMR Biomed 14(7-8):453.

$R2'$ and $\Delta R2'$ in Kidneys: Evaluation of BOLD based Susceptibility Contrast

Jon Thacker[1], Huan Tan[2], Pottumarthi Vara Prasad[1,2]
[1]*Biomedical Engineering, Northwestern, Evanston, Illinois,* [2]*Northshore University Health System, Evanston, Illinois*

Background/Purpose:

Blood oxygenation level dependent (BOLD) MRI is probably the most widely used susceptibility based contrast. However, T2* weighted imaging or R2* mapping are most commonly used to-date. In most organs, tissue oxygenation is supply limited and so evaluation of blood flow is commonly used. In the kidneys, since renal function (hence oxygen consumption) tracks blood flow (oxygen supply), evaluation of renal oxygenation is an important factor in understanding the overall health of the organ. Kidneys exhibit spatially inhomogeneous oxygenation; the medulla is poorly oxygenated relative to the cortex. Due to this inhomogeneous distribution, it is valuable to estimate this spatial map of oxygenation within the kidneys as opposed to evaluating at a global level. Typically, renal oxygenation is estimated by BOLD MRI through the use of R2* estimation [1]. R2* is comprised of two components: R2 and R2'. The dependence on R2 makes R2* mapping sensitive to changes in local tissue physiology other than changes in oxygenation. The other component, R2', is related to magnetic susceptibility and has been investigated for its sensitivity to renal oxygenation.

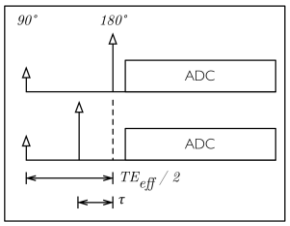

Figure 1: ASE Diagram

R2' can be directly estimated by using asymmetric spin echo (ASE) sequences [2,3]. The ASE-EPI sequence employs a spin echo with an EPI readout. The refocusing pulse is then shifted to give more local susceptibility weighting to the resulting image [3]. R2' can then be estimated by fitting the magnitude signal over multiple shifted echo times (τ). Previous implementation of the renal ASE-EPI sequence has been limited in spatial resolution as it employed single shot acquisitions [2]. This limitation is due to the fact that as matrix size increases, the readout train increases too. However, the readout length is limited by the effective TE/2, which is constrained to maintain a sufficient signal to noise ratio (Figure 1). This inherent limitation on spatial resolution can be an issue when attempting to differentiate renal anatomy.

A previous study [2] also acquired different τ values during a single breath-hold scan. This may limit the widespread utility due to the long breath-hold interval. This interval determines how many τ values can be sampled each breath-hold. By implementing a navigator-gated acquisition, the constraint on the number of phase encodings and τ values is lifted. In this study, we have implemented a navigator-gated, multi-shot (segmented) ASE sequence to facilitate free-breathing scans, improved spatial resolution and allow for an arbitrary number of τ values to be acquired.

Methods:

All experiments were performed on a 3T MRI system (MAGNETOM Verio, Siemens Healthcare, Erlangen, Germany) using the body and spine phased array coil. To-date data was acquired in 8 healthy subjects. A 2D navigator was employed to trigger data acquisition based on respiration. The navigator plane was positioned over the liver-lung interface to estimate kidney motion. Each 2D navigator image was reduced to a one-dimensional image, with the dark band representing the diaphragmatic level.

ASE-EPI image acquisitions were triggered during expiration (apex of the navigator profile). We used τ values ranging from 15 ms to 27.75 ms in steps of 0.75 ms, resulting in 18 images. The signal intensity was fit to the equation $S(\tau) = S_o \exp(-2\, R2'\, \tau)$ to estimate R2' for each voxel. An interleaved, 2-shot EPI readout trajectory was used. Further imaging parameters are as follows: effective TE=65ms, TR=1000ms, FOV=250mm x 250mm, Matrix=128 x 112, Slice Thickness=6mm, Bandwidth =1149 Hz/Pixel. Images were reconstructed to 256 x 224 by interpolation. Regions of interest (ROI) were drawn around the cortex and medulla to extract averaged $R2'$ values.

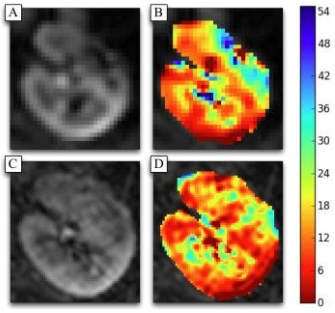

Figure 2: R2' Maps. (A,B) Single-shot breath-hold. (C,D) Segmented, Navigator gated. (A,C) Anatomic. (B,D) R2' maps

Three of subjects were imaged before and after furosemide administration to estimate $\Delta R2'$ for each region. $\Delta R2'$ was then estimated as $R2'_{region}\,(pre\ furosemide) - R2'_{region}\,(post\ furosemide)$. For these studies, the increment between each τ value was increased (from 0.75 to 1 ms) with τ ranging from 15 to 28 ms, resulting in 13 images. This reduction was implemented to minimize the total acquisition time especially post-furosemide when the subject's need to urinate. All other imaging parameters are the same as above.

Results:

Average values from 5 volunteers for R2' in the cortex and medulla were found to be $10.09 \pm 5.41\ s^{-1}$ and $17.38 \pm 8.49\ s^{-1}$, respectively. These values are consistent with the previous report [3]. Figure 2 shows the images from the same subject at both the smaller matrix size of 64x56 and the segmented version of 128x112. Improved delineation of the renal cortex and medulla was observed with the segmented ASE sequence.

Representative plots of signal vs. τ are illustrated in Figures 3.A,B (cortex) and 3.C,D (medulla) where the blue dots are the acquired data points and the red line is the fitted curve. $\Delta R2'$ in the cortex and medulla were found to be $-0.23 \pm 2.58\ s^{-1}$ and $7.28 \pm 1.62\ s^{-1}$ respectively, and the trends are consistent with experience to-date with ΔR2*.

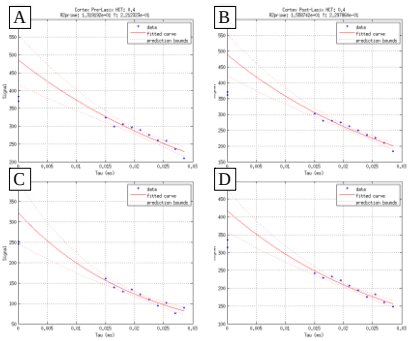

Figure 3: Representative R2' plots. (A,B) Cortex. (C,D) Medulla. (A,C) Pre-furosemide. (B,D) Post-furosemide.

Conclusion:

Navigator gated, segmented EPI based ASE-EPI sequences provide several benefits over previously demonstrated methods. Navigator gating allows for data to be acquired while subjects are freely breathing, increasing their comfort and allow multi-slice imaging. A navigator gated scan further allows for an unconstrained number of different τ values to be acquired, which should increase the quality of the R2' curve fitting. By segmenting the EPI readout train, higher spatial resolutions are achievable and allow for better differentiation between the anatomical structures of the kidney without increasing the effective TE and hence compromising SNR. Parallel imaging and partial Fourier encoding are two other techniques that can be used to improve resolution, though at the cost of SNR and resolution along the phase encode direction, respectively.

References:

[1] [*Magn Reson Imaging Clin N Am*. 2008 Nov;16(4):613-25], [2] [*NMR Biomed*. 2013 Jan;26(1):91-7], [3] [*Magnetic resonance in medicine* 2003 Oct;50(4):708-16].

Brachytherapy Seed Identification Using Susceptibility Mapping

Ying Dong[1], Zheng Chang[2], Gregory Whitehead[1] and Jim Xiuquan Ji[1]
[1]*Department of Electrical and Computer Engineering, Texas A&M University*
[2]*Department of Radiation Oncology, Duke University*

Background/Purpose:

Brachytherapy is a method to treat certain cancers (e.g., breast and prostate cancers) by directly inserting radioactive seeds into the malignant tissues. The seeds, composed by radioactive material and metallic shells, provide highly localized radiations. During the intra-operative and post-operative phases, CT or Ultrasound imaging are commonly used for guidance and verification. MRI is another promising imaging tool for this application. However, brachytherapy seeds and its surrounding areas normally appear dark in the magnitude MRI image. Identification of the seeds from other susceptibility artifacts or the cavities/voids in the tissue is a difficult problem, which can further hinder the radiation dose quantification. In this work, we propose to use an improved quantitative susceptibility mapping (QSM) method for seed identification. A unique feature of the proposed method is the use of an automatically defined mask to leave out the unreliable data in the regularized model fitting. Experimental results show that the proposed method can correctly locate the seeds and differentiate them from the tissue voids/structures.

Methods:

In MRI, the local magnetic field can be modeled as a convolution of the susceptibility distribution with a dipole kernel [1,2]

$$\boldsymbol{\psi} = \mathbf{C}\boldsymbol{\chi} \tag{1}$$

where $\boldsymbol{\psi}$ is the field map, $\mathbf{C}$ is convolution operator based on the dipole kernel, and $\boldsymbol{\chi}$ is the susceptibility distribution. In practice, the field map can be measured using a sequence of phase images acquired at different echo times. Determination of susceptibility is the inverse problem of Eq. (1). One effective method to recover $\boldsymbol{\chi}$ is a sparsity-constrained L_1 minimization in [1] where the problem is formulated as

$$\arg\min_{\boldsymbol{\chi}} \left\|\mathbf{C}\boldsymbol{\chi} - \boldsymbol{\psi}\right\|_2^2 + \lambda \left\|\mathbf{G}\boldsymbol{\chi}\right\|_1 \tag{2}$$

where $\mathbf{G}$ denotes the first order gradient operator to enhance smoothness of the solution. This method has worked well for QSM in applications using SPIO or liver iron quantifications where the susceptible materials are much smaller than the voxel size. However in our application, the seeds are significantly larger (on the order of millimeters). T2* decay can lead to signal loss over several nearby voxels. Therefore Eq. (2) cannot be directly applied, as the data will be very noisy and unreliable. We proposed to use an improved formulation which is similar to the one in [3] where the susceptibility is derived from.

$$\arg\min_{\boldsymbol{\chi}} \left\|\mathbf{W}(\mathbf{C}\boldsymbol{\chi} - \boldsymbol{\psi})\right\|_2^2 + \lambda \left\|\mathbf{M}\mathbf{G}\boldsymbol{\chi}\right\|_1 \tag{3}$$

where $\mathbf{W}$ is a weighting matrix and $\mathbf{M}$ is a masking matrix. The weighting matrix is defined based on the magnitude image. Specifically, the weight is proportional the image magnitude so that the noisy areas surrounding the seeds will have a small weight since the signal magnitude will be small. In addition, the background area outside the object are segmented and given a zero weight. The masking matrix is specified by applying a threshold to the magnitude image. As a result, the seeds and the surrounding areas are masked out so that they will not contribute to the smoothness constraint in Eq. (3). Because the susceptibility of the seeds is much higher than that of the tissues, there is a large phase gradient on the phase images surrounding the seeds. Therefore, the susceptibility map cannot be considered smooth in these regions anymore. The mask, as constructed, will avoid the unnecessary smoothness constraint over the seed regions. Solving Eq. (3) is achieved by a non-linear conjugated gradient with backtracking line-search. All data processing were performed in Matlab by MathWorks.

Results:

A phantom was constructed to simulate a prostate brachytherapy setup. The phantom was made of a piece of beef, with three inserted dummy brachytherapy seeds (seeds with the same shell materials and structures but no radioactive material inside). In addition, a plastic stick was inserted to simulate the tissue voids, and a bamboo tooth pick filled with water was inserted to simulate the capillary. A spin echo sequence with shifted 180 degree pulse (ΔTE = -0.3ms, 0ms, and 0.3ms) was used to measure the field map on a 4.7 T, 33cm-bore magnet. The image size is 128x128x6 with an FOV of 80x80x9 mm^3. The seeds and sticks were inserted along a direction orthogonal to the main magnetic field. The regularization parameter λ was chosen experimentally over a range from 10^{-6} to 10^{-4}.

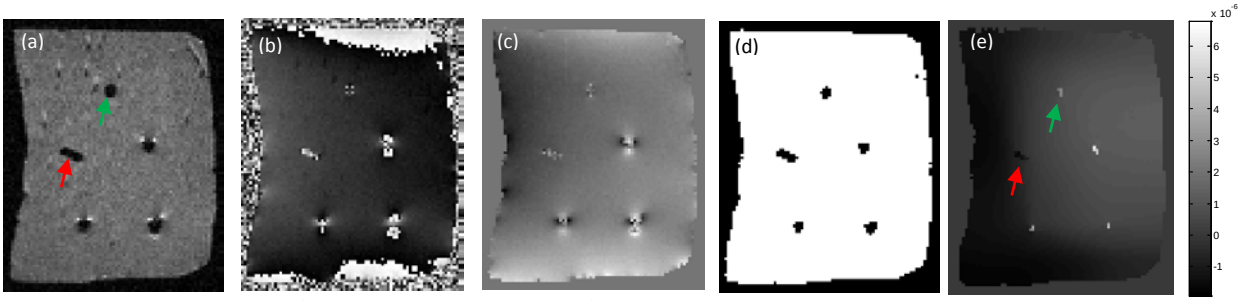

Fig. 1 (a) Magnitude and (b) phase images of the central slice. (c) Calculated field map, (d) mask, and (e) corresponding susceptibility map calculated using the proposed method. As shown, the seeds are clearly differentiated with voids. The red arrow indicates the plastic stick and the green arrow the bamboo stick. The other three inserted objects are seeds.

Fig. 1 shows the raw data and the deconvolution results. As shown, the proposed method can correctly locate the seeds and differentiates the seeds from the other simulated tissue voids and capillary. The maximal susceptibility calculated for the seeds is about 7ppm, which is smaller than the value in the literature. This could be due to the partial volume effect. Further work and improvement are still needed to obtain more consistent and accurate results.

Conclusion:

We proposed to use susceptibility mapping to identify brachytherapy seeds. The method adopts an improved weighted deconvolution method with an masking matrix specifically designed for the application. Experimental results show that the seeds can be identified and differentiated using the proposed method.

References:

[1] L. Rochefort, et. al, MRM, v63:194-206, 2010. [2] B. Kressler, et. al, IEEE med. Imag., v29:273-281, 2010. [3]J. Liu, et. al, NeuroImage v59:2560-2568, 2012.

Susceptibility-Based Estimation of Liver Iron Concentration Using a Fat-Referenced Approach

Diego Hernando[1], Samir D. Sharma[1], Debra Horng[2], Rachel Cook[3], Carol Diamond[4], Scott B. Reeder[1,2,3,5]
Departments of: [1]*Radiology,* [2]*Medical Physics,* [3]*Medicine,* [4]*Pediatrics,* [5]*Biomedical Engineering*
University of Wisconsin-Madison, Madison, WI, USA

Background/Purpose: Quantification of iron is critical for the diagnosis, staging and treatment monitoring of liver iron overload[1]. Unfortunately, current methods to quantify liver iron concentration (LIC) are either inaccurate (e.g. serum markers), invasive (e.g. biopsy), or have poor accessibility (e.g. susceptometry). MR-based quantification of magnetic susceptibility in the liver would enable a noninvasive and widely accessible measure of LIC that is independent of magnetic field strength[1-4]. However, quantification of susceptibility is challenging, due to the ill-posed nature of the inverse problem (i.e. mapping susceptibility from the measured B_0 field)[2]. Further, the presence of fat and large background B_0 inhomogeneities pose additional challenges for susceptibility mapping in the abdomen. The purpose of this work is to demonstrate the feasibility of MR-based LIC quantification using a simplified susceptibility-based, fat-referenced boundary approach[3,4].

Methods: We scanned: 1) phantoms consisting of vials with increasing concentrations of super-paramagnetic iron oxide (SPIO) immersed between layers of oil and water, and 2) twenty-seven subjects (9 controls and 18 subjects with liver iron overload). Spin-echo acquisitions (1.5T) provided R2-based reference in vivo LIC measurements (Ferriscan)[5]. Multi-echo 3D-SPGR sequences (1.5T and 3T) enabled fat-water separation and B_0-mapping. Phantom and liver iron concentrations were estimated from the B_0 map using a fat-referenced boundary approach[3,4]. The iron concentrations in phantoms were estimated from the difference in B_0 (ΔB_0) between the vials and the neighboring oil (assuming a saturation magnetization of SPIOs M_s=93 Am^2/kg). Liver susceptibility[3,4], and subsequently LIC[6,7], were estimated from ΔB_0 between the lateral right lobe of the liver and adjacent subcutaneous adipose tissue (SAT) (Figs. 1-2, Eq. 1)[3,4]. The estimated χ-LIC values were compared to Ferriscan-LIC.

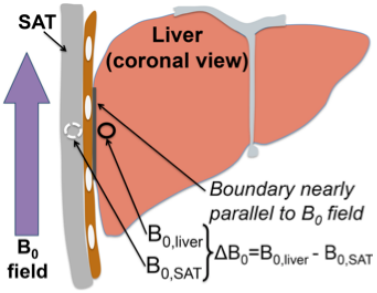

Figure 1: *Simplification of the QSM inversion. The field map difference (ΔB_0) between subcutaneous adipose tissue (SAT) and liver can be used to derive a localized estimate of LIC.*

$$LIC = 14.08\Delta B_0 - 4.07\Delta\chi_{base} \quad [1]$$

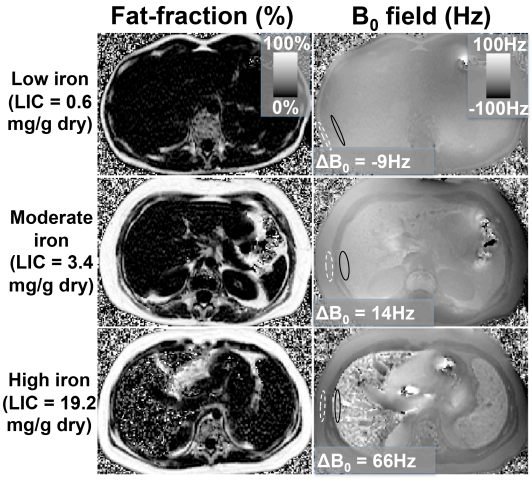

Figure 2: *The B_0 field difference (ΔB_0) was measured by placing one ROI in the subcutaneous adipose tissue (white ellipse) and another in the liver (black ellipse). The LIC was then calculated using Eq. 1.*

Results: Estimated phantom iron concentrations (Figs. 3-4) had good correlation and agreement with reference iron concentrations both in phantoms and in vivo. Underestimation in phantoms may be due to assumptions about saturation magnetization of SPIOs. Note that estimation of LIC using the boundary B_0 measurement approach leads to relatively large variability (particularly at 1.5T), including some negative LIC values. This is likely due in part to the presence of uncorrected background B_0 field variations, and possibly also to imperfect alignment of the boundary with B_0 (Fig. 1).

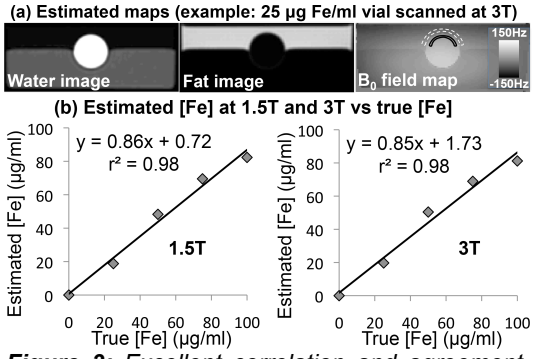

Figure 3: *Excellent correlation and agreement between susceptibility-based estimates in a phantom support the feasibility in vivo*

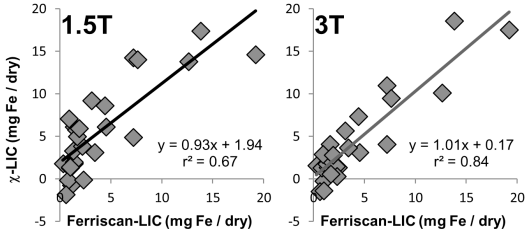

Figure 4: *In vivo susceptibility-based estimates of LIC is feasible. Preliminary results show very good correlation and agreement with Ferriscan.*

Conclusion: Susceptibility-based LIC estimation is feasible when using SAT as an internal reference. This approach may enable "fat-constrained" QSM in the abdomen by exploiting the presence of adipose tissue and using a fat-water separation technique.

References: (1) Brittenham GM. N Engl J Med 2011; (2) de Rochefort L, et al. MRM 2008; (3) Wang ZJ, et al. JMR 1999; (4) Taylor BA, et al. JMRI 2012; (5) St Pierre TG, et al. Blood 2005; (6) Schenck JF. Med Phys 1996; (7) Fischer et al, Ann N Y Acad Sci 2005.

Acknowledgements: We acknowledge support from the NIH (RC1 EB010384, R01 DK083380, R01 DK088925, and R01 DK096169) the Wisconsin Alumni Research Foundation (WARF) Accelerator Program, and the UW Institute for Clinical and Translational Research (ICTR), and GE Healthcare.

Are transverse relaxation rates and susceptibility maps equivalent in Parkinson's disease studies?

Jeam Haroldo Oliveira Barbosa[1], Antonio Carlos dos Santos[2], Vitor Tumas[2] E. Mark Haacke[3-4], Carlos Ernesto Garrido Salmon[1]
[1]*Faculdade de Filosofia, Ciências e Letras de Ribeirão Preto, University of Sao Paulo, Ribeirao Preto, São Paulo, Brazil,*
[2]*Faculdade de Medicina de Ribeirão Preto, University of Sao Paulo, Ribeirao Preto, São Paulo, Brazil,*
[3]*MRI Institute for Biomedical Research, Detroit, Michigan, United States,* [4]*Wayne State University, Detroit, Michigan, United States*

Introduction: The ability of iron to accept and donate electrons present in the human body, makes it essential for cellular homeostasis and various biological reactions. However, the excess of this metal in the brain may have deleterious effects by generating reactive oxygen species that cause oxidative stress[1]. Some studies of past decades have been found high iron concentration in parkinsonian brains from cadavers[2-5] of mainly region substantia nigra and globus pallidus. The iron quantification in vivo can thereby contribute to understand if this metal deposition is cause or consequence of Parkinson disease. There are a variety of MR techniques by which iron content in vivo tissue can be indirectly estimated. These include: transverse relaxation rates (R2 and R2*)[6] and quantitative magnetic susceptibility (QSM)[7-9,18]. Several research groups have applied MR techniques for the study of Parkinson disease, but the published results are inconsistent as showed in a recent review[10]. To our knowledge, none reported study has used all techniques for differentiate controls and patients at the same time. Our aim is evaluate which MR technique (relaxometry R2 or R2* and magnetic susceptibility (QSM)) is more adequate to differentiate healthy and Parkinson's disease.

Methods: Fourteen healthy controls (62.5±7.1 years) and fourteen Parkinson's patients (66.4±6.8 years) were recruited from the Hospital of Clinicas of University of Sao Paulo (Ribeirao Preto, Brazil). No significant difference between groups related to age (p=0.16). This study received the approval from the local Ethics Committee. The patients were selected by two experienced neurologists with expertise in extrapyramidal diseases; all patients were on stage 2 or 3 according to the Hoehn and Yahr scale. The imaging procedure was performed in a 3T MRI scanner. For R2 estimation, a Turbo Spin Echo sequence with 16 equally spaced echoes (12-196 ms) was used with TR=3000ms and resolution 0.479x0.479x2.0 mm^3. For R2* and QSM a gradient multi-echo sequence was used (TE=7.7, 19.7, 31.7, 43.7 ms) with TR= 48ms and the same spatial resolution. An algorithm was implemented in Matlab to draw regions of interest (ROIs), generate relaxometry maps and extract the mean values for each ROI. Several ROIs were drawn in the midbrain region: substantia nigra (SN), red nucleus (RN), globus pallidus (GP), putamen (PUT), caudate nucleus (CN), thalamus (THA), white matter (WM). The R2 and R2* were calculate from a mono-exponential fit point by point. The susceptibility maps were created by first phase unwrapping the data with FSL[11], then creating a mask to remove the sinuses using the bet2 tool on FSL[12]. SHARP filter[13]was used to remove background phase contributions (radius 6 mm, regularization parameter 0.05). The resultant phase images were processed using the SWIM algorithm[14] to create susceptibility maps using Matlab (SMART SWIM). The susceptibility values ($\Delta\chi$) were relative to a certain reference region in the white matter. A statistical unpaired t-test was applied to compare both groups (patient and control) using the software Origin Pro8.

Results: Figure 1 shows example of QSM maps for one control and one patient. The comparison between both groups for several ROIs considering the mean values of each parameter (R2, R2*, $\Delta\chi$) is represented in the figure 2. A linear correlation between $\Delta\chi$ and R2 or R2* was found independently of the group (Figure 3). The R2' values (R2*-R2) were also analyzed, but it didn't show significant difference in the analyzed ROIs.

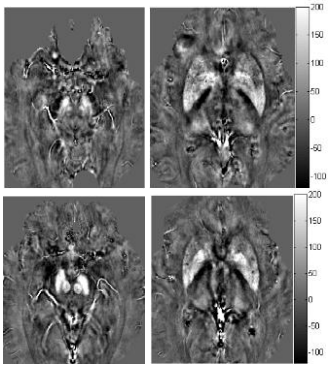

Fig. 1: Two axial slices of QSM for the midbrain and basal ganglia for healthy controls (above) and patient with Parkinson disease (below).

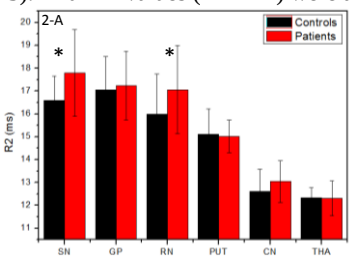

Fig. 2: Mean value and standart desviation of the evaluated parameters for both groups and several ROIs. A, R2. B, R2*. C, $\Delta\chi$. The (*) represent significance difference (p<0.05).

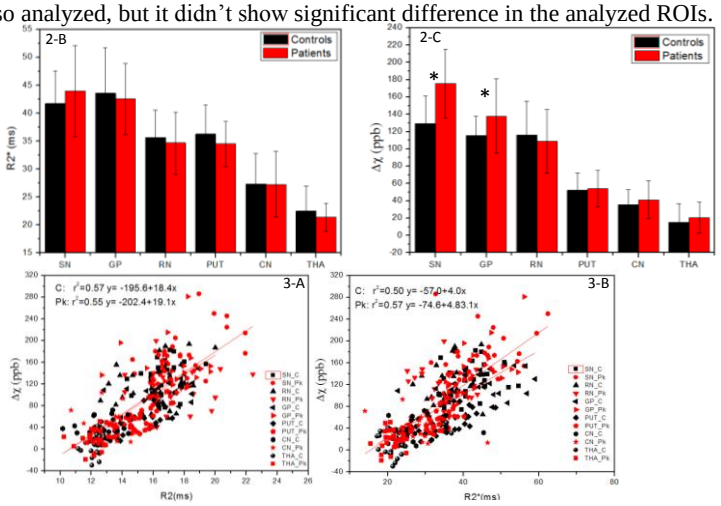

Fig. 3: Linear regresion between $\Delta\chi$ and relaxometry rates for all data in controls (C) and patients (Pk): A, R2. B, R2*.

Discussion: R2, R2* and $\Delta\chi$ values showed a not significant trend with age, because all subjects had more than 50 years and the iron concentration showed little change in elderly people for all regions[15]. Among all techniques just relaxometry R2 and QSM identified significance difference between controls and patients for substantia nigra (figure 2). This result is agreeing with other in vivo reports that studied SN compact with R2[16,17] and magnetic susceptibility[18]. Additionally, post-mortem studies also confirm for iron concentration in SN and SN compacta of healthy controls and patients[2-5]. We also found significance difference for R2 values in red nucleus and $\Delta\chi$ values in GP (figure 2). For R2* we didn't find significance difference between groups in partial agreement with others papers observed in a review[10]. This contradictory result can be explain because R2* measurement is influenced by other field source, unrelated to brain iron levels[19]. The correlation between the parameters of different MRI techniques evidenced a similar behavior between $\Delta\chi$ and R2 or R2* for both groups (figure 3).

Conclusion: R2 and QSM evidenced significance difference for controls and patients in specific region of substantia nigra. The transverse relaxation rates and susceptibility maps have high linear correlation. However the more recent papers had suggested QSM for study neurodegenerative disease, we showed that relaxometry R2 has also good results for differentiate controls and patients with Parkinson. Although we found significant differences between controls and patients, we still need to improve the sensitivity of all techniques with a goal to clinical application.

References: 1. Nancy and Andrews, The New Engle Jounal of Medicine, 341: 1986-95.1999. 2. Sofic E. et al. Neural Transmission, 74(3):199-205. 1988. 3. Dexter D.T. et al., Lancet, 21(2)(8569) pp.1219-20. 1987. 4. Dexter D.T. et al., J Neurolchem. 52:1830-1836. 1989. 5. Griffiths P.D., et al., Brain. 122:667– 673. 1999. 5. Sofic E., et al., Neurochem, 56:978-982. 1991. 6. Gorell J.M. et al., Neurology, 45: 1138 –1143. 1995. 7. Haacke E.M. and Reichenbach J.R ed., book. New Jersey, Wiley-Blackwell. 2011. 8. Shmueli, K., et al. Magn. Reson. Med. 62, 1510–1522, 2009. 9. Wharton, S., Bowtell, R., 2010. Neuroimage 53, 515-525. 10. Gröger A. and Berg D. J Neural Transm. 119(12): 1523-8. 2012. 11. Jenkinson, M., Magn. Reson. Med. 49 (1), 193–197. 2003. 12. Smith S.M., Human Brain Mapping, 17(3):143-155, 2002. 13. Langkmmer C. et al. (2012). Neuroimage 62, 1593-1599. 14. Haacke E.M. et al. (2010) J Magn Reson Imagin 32:663-676. 15. Hallgren B. and Sourander P., (1958), J. Neurochem. 13, 41-51. 16. Kosta P. et al., Neurol., 253: 26-32. 2006. 17. Ryvlin P. Arch Neurol. 52(6):583-8 1995. 18. Lotfipour A. K., et al., JMRI, 35(1), 48–55, 2012. 19. Schuff N. Mov. Disord. 24:S684-S690. 2009.

Quantitative Susceptibility Mapping (QSM) for Characterization of the Motor Cortex in Amyotrophic Lateral Sclerosis (ALS) and Other Motor Neuron Diseases

Andrew D Schweitzer[1], Tian Liu[1], Karen Zheng[1], Stephen Seedial[1], Alexander Shtilbans[2], Jennifer Greene[2], Mona Shahbazi[2], Dale Lange[2], Yi Wang[1], A John Tsiouris[1]

[1]*Dept of Radiology, New York Presbyterian Hosp, Weill Cornell Medical Center, New York, NY,* [2]*Dept of Neurology, Hospital for Special Surgery, New York, NY*

Background/Purpose:

Specific diagnosis of motor neuron diseases is often difficult due to lack of disease biomarkers. For amyotrophic lateral sclerosis (ALS), there currently exists no quantitative laboratory, imaging, or electrophysiological test that confirms disease presence or correlates with disease severity. Patients with ALS have been shown to have T2 hypointensity in the motor cortex, possibly due to the T2* effect of deposition of paramagnetic species such as iron (1). Quantitative susceptibility mapping (QSM) is a novel MRI technique whose pixel intensity directly reflects tissue susceptibility. We sought to determine whether patients with motor neuron disease demonstrate increased tissue susceptibility in the motor cortex when compared to a control group.

Methods:

Utilizing a 3.0T MRI system, morphology enabled dipole inversion was used to generate QSM images (2,3) for seven patients with upper motor neuron disease and 23 control patients. Motor cortices were drawn on axial images in a standardized fashion under the guidance of an experienced neuroradiologist. A semi-automatic program was used to refine the segmentation between motor cortices and adjacent white matter/CSF by applying a threshold. Mean motor cortex susceptibility was calculated, and the Wilcoxon rank sum test was used to evaluate for statistical differences between the groups.

Results:

Three patients had clinically confirmed ALS, one had confirmed primary lateral sclerosis (PLS), and three had unspecified upper motor neuron disease (possible ALS). In disease and control groups, mean ages were 58.3 and 56.6 and percent male were 71% and 57%, respectively. Mean motor cortex susceptibility was found to be significantly higher in patients with motor neuron disease than in control patients (41.6 and 28.5, respectively; p=0.002). Confirmed cases of ALS had the highest susceptibility (46.2), followed by motor neuron disease possibly ALS (40.7), then confirmed PLS (30.3), and the control group with the lowest susceptibility (28.5).

Conclusion:

QSM has the potential to be a quantitative imaging biomarker for patients diagnosed with motor neuron disease. Further study is necessary to determine whether QSM signal in the motor cortex correlates with disease severity in ALS and other motor neuron diseases.

References:

1. Oba H, Araki T, Ohtomo K, et al. Amyotrophic lateral sclerosis: T2 shortening in motor cortex at MR imaging. *Radiology* 1993:189:843-6.

2. Liu T, Lui J, de Rochefort, et al. Morphology Enabled Dipole Inversion (MEDI) from a single angle acquisition: comparison with COSMOS in human brain imaging. *Magn Reson Med* 2011:66(3):777-83.

3. Liu J, Lui T, de Rochefort, et al. Morphology Enabled Dipole Inversion for quantitative susceptibility mapping using structural consistency between the magnitude image and the susceptibility map. *Neuroimage* 2012:59(3):2560-8.

Validation of QSM for brain iron mapping in multiple sclerosis using postmortem studies

Hongfu Sun, Andrew Walsh, Kenneth Warren, Gregg Blevins, Edward Johnson, Jian Lu, Alan Wilman
University of Alberta, Edmonton, Canada

Background/Purpose: QSM is a new promising MRI method that has been proposed to quantify brain iron in vivo. Using postmortem healthy subjects, Langkammer et al. found high correlations for QSM in subcortical gray matter (GM) compared to chemical iron analysis (1). However, no postmortem studies have validated this correlation in multiple scleroses (MS), where susceptibility could be influenced by different pathological processes of the disease, such as demyelination, cellular infiltration, and edema. In this study, we examine the correlation of QSM performed in situ in postmortem MS subjects to Perls' ferric iron stain for subcortical GM.

Methods: *MRI Acquisition* 3D multiple gradient-echo acquisitions were collected at 4.7T from 3 MS male subjects (two in situ<28 hrs after death, subject 1: 60 yrs; subject 2: 63 yrs; one in vivo 1 yr before death, subject 3: 45 yrs). Acquisition parameters were: FOV 256×128-160×160 mm; spatial resolution 1×0.8-1×2 mm; 80 axial slices; TR 44 ms; 5 echoes with echo spacing 4.1 ms; first echo time 2.9-3.2 ms; flip angle 10°.
QSM Reconstruction Susceptibility maps were reconstructed based on the phase measures from 5 echoes acquired from 4 individual receiver channels, following three main steps: phase pre-processing, background field artifact removal, and susceptibility inversion. First, phase from the 4-channel array coil were combined after removing channel-phase-offsets (2). Channel-combined phase images from 5 echoes were then unwrapped with PRELUDE/FSL, followed by corrections of 2π jumps between echoes. A single field map was generated by fitting the unwrapped phase maps to echo times. The fitting residuals were used as a field reliability map after setting a proper threshold to exclude unreliable field measurements from ROI. Background field removal was then performed using a new method RESHARP ("Regularization Enabled Sophisticated Harmonic Artifact Reduction for Phase data") (3). Briefly, RESHARP performs the spherical mean value filtering on the phase images to remove harmonic background component, but with an additional Tikhonov regularization to refine the least-norm solution from the deconvolution step and to best suppress non-harmonic artifacts (e.g. unwrapping errors, phase offsets). Finally, single-angle dipole inversion for QSM was performed on the filtered field map using the total variation regularization approach (4). Deep gray matter structures were examined using ROI analysis in comparison to Perls' ferric iron staining outlined below.
Postmortem Histology The three MS postmortem brains were extracted and fixed in 18% formalin for at least two weeks then cut into 8 mm slices. Subject 1 was cut axially, while subject 2 and subject 3 were cut in coronal. Slices containing subcortical GM were photographed before and after staining with Perls' ferric iron reaction - slices were immersed in 1 liter of 2% hydrochloric acid mixed with 1 liter of 2% potassium ferrocyanide for 30 minutes. This stain detects iron stored in ferritin, which is in the ferric form. The normalized intensity differences between stained and unstained photographs were referred to as a relative optical density where a higher value corresponds to more iron staining.
Analysis ROIs of iron-rich subcortical GM were drawn around the boundary of the structures on the photographs. Susceptibility maps were then manually registered to the photographs and ROIs on QSM were drawn for the corresponding subcortical GM with the reference of the photographs. Each structure was measured on both left and right sides and on multiple slices whenever possible.

Results: As shown in Fig.1 top row, for subject 3, subcortical gray matter is well depicted and clearly delineated in both susceptibility map and Perls' iron staining photograph, with hyperintensities in susceptibility map corresponding well with hypointensities in Perls' iron staining. The correlation between susceptibility and optical density from Perls' iron staining for subject 3 is shown in Fig.1 graph with a very good linear correlation of R^2= 0.758. The other two in situ subjects had correlations of R^2 = 0.703 and 0.716.

Conclusion: QSM from postmortem MS subjects had strong linear correlations to brain iron as determined by Perls' ferric iron staining, and could potentially be used to indicate the iron status of subcortical gray matter structures in multiple sclerosis.

References: [1] Langkammer C et al. Neuroimage 2012;62(3):1593-9. [2] Robinson S et al. Magn Reson Med 2011;65(6):1638-48. [3] Sun H et al. ISMRM2013, Abstract# 693. [4] Wu B et al. Magn Reson Med 2012;67(1):137-47.

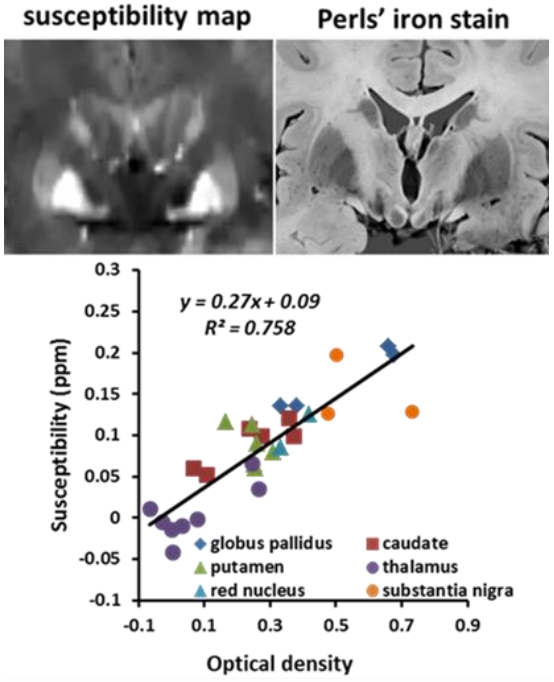

Fig. 1: Subject 3, coronal view of QSM vs. Perls' iron stain and their linear correlation.

Iron Clusters in white matter studied by microscopic MRI and histological methods

Guochun Fu[1], Tie-Qiang Li[1,2], and Jeff Duym[3]
[1]*Department of Clinical Science, Intervention and Technology, Karolinska Institute, Sweden,*
[2]*Institute of Biomedical Engineering and Instrument Science, Zhejiang University, China,*
[3]*Lab of Functional and Molecular Imaging, National Institute of Neurological Disorders and Stroke, USA*

Background: Susceptibility-weighted MRI at high magnetic field strength has recently been used to reveal cortical layer structures [1] and white matter heterogeneity *in vivo* [2]. Magnetic susceptibility differences have been widely considered to give rise to most of the contrast but the precise sources underlying the contrast is still poorly understood. Cell density and type, iron, and myelin contents may vary across the cortical regions and all can become the important sources for the susceptibility difference. For example, it has been demonstrated that magnetic susceptibility variations across some cortical layers are mainly associated with iron content, whereas the susceptibility contrast among different fiber pathways is largely related to the difference in myelin content. In this study, findings from microscopic MRI and histological studies of white matter specimens of the human brain, which may provide further clues for better understanding of the mechanisms underlying the susceptibility contrast in the brain.

Methods: Multiple white matter specimen of human brain were extracted from formalin-fixed males (age= 66-78) who died of non-neurological related causes. The samples were carefully washed with de-ionized water and sealed in 15 mm NMR tubes. The samples included different white matter tracts, such as corpus callosum, cingulum fiber bundle, white matter from visual and motor cortices. The MRI data acquisition was conducted using a 11.7T experimental MRI system (Bruker Biospin) with a dedicated home-build probe. Most of the MRI acquisitions were conducted over weekends to produce sufficient SNR by signal averaging. Typical scan protocol was based on a 3D multi-echo (4 echoes) gradient-recalled echo pulse sequence. Images with isotropic voxel size of 30 μm were readily achieved with overnight data sampling. Several samples were even scanned at 12.5 μm isotropic resolution. Perls' iron staining was performed in multiple tissue sections using DAB enhancement [3]. The post-processing of the MRI data was conducted off-line using home/made Matlab programs. The magnitude, phase, and derived susceptibility images from the MRI data were compared with the micrographic images of the iron staining.

Results: Similar patch structures with almost regular signal intensity variations were observed in different white matter regions in the acquired MRI images, although the total of volume of the structures is quite small. Typical size is in the range of 30-100μm estimated from the scattering patterns of the magnitude images. The variation patterns in the magnitude images were nearly opposite to these in the corresponding phase images. Line plots of the phase and magnitude data usually depict opposite contrast. Surprisingly, contrast patterns similar to the MRI phase images were also detected in the micrographs of the iron staining. The average bulk susceptibility of these cluster were about 0.19±0.07 ppm, as evaluated from the quantitative susceptibility mapping.

Conclusion: Based on the experimental observations, we can conclude the following: (1) Iron deposition in white matter is clustered and varies substantially across white matte regions; (2) The similar appearance of micrograph from iron staining and the phase images suggest that the patch structure is likely to be related to clusters of iron deposit in white matter; (3) Since both myelin and iron enhance T2* relaxation but contribute oppositely to the frequency shift, in the clusters the opposing contrast patterns between the magnitude and phase images indicate that the susceptibility contribution of the local iron is quite high compared to that from the myelin, whereas outside the clusters the dominant contribution is from the myelin content as indicated by the similar contrast between magnitude and phase images; (4) The above conclusion agrees with the observation that there is relative high bulk susceptibility value in the cluster structures; (5) Evidence from previous and current studies support the hypothesis that iron and myelin enhance R_2* relaxation, but myelin causes a frequency shift opposing that of iron. Therefore, combined analysis of R_2* and frequency shifts might allow quantitative determination of the relative contribution of iron and myelin to tissue susceptibility characteristics.

References:

[1]. J.H. Duyn et al. *PNAS*, 104:11796 (2007)
[2] Li,T.Q. et al. *Neuroimage*, 32:1032 (2006)
[3] Moos T. et al. *Histochem* 99:471 (1993)

R2* Relaxometry and Quantitative Susceptibility Mapping for The Assessment of Brain Iron Deposits in a Patient With Mitochondrial Membrane Protein-associated Neurodegeneration

Ulrike Löbel[1], Aracelli Meyer-Osores[2], Jan Sedlacik[1], Ferdinand Schweser[3], Regine Grosse[2], Andreas Deistung[3], Jürgen R. Reichenbach[3], Angela Schulz[2], Monika Hartig[4], Alfried Kohlschütter[2]

[1] *Neuroradiology, University Medical Center Hamburg-Eppendorf,* [2] *Clinic for Degenerative Brain Diseases, Children's Hospital, University Medical Center Hamburg-Eppendorf, Hamburg, Germany,*
[3] *Medical Physics Group, IDIR I, Jena University Hospital,Friedrich Schiller University Jena, Germany,*

[4] *Institute of Human Genetics, Technische Universität München, Munich, Germany*

Introduction:
During recent years, the number of diseases classified as neurodegeneration with brain iron accumulation (NBIA) has steadily increased (1,2). Although the underlying mechanisms linking the iron deposition to the neurodegeneration and clinical symptoms remain unclear, recent therapeutic trials have aimed at a reduction of the cerebral iron content (3). We monitored potential effects of iron chelating therapy (deferiprone) by Quantitative Susceptibility Mapping (QSM) and R2* relaxometry in a patient with mitochondrial membrane protein-associated neurodegeneration (MPAN) (4).

Patient and Methods:
A 13-year-old girl presented with a 6-year history of progressive loss of vision due to optic nerve atrophy and recent development of mild cognitive decline and gait abnormalities. In addition to bilateral atrophy of the optic nerve, the initial MRI showed low T2 signal of the globus pallidus (GP) and subtantia nigra (SN), suggestive of NBIA. MPAN was diagnosed by the molecular genetic finding of a compound heterozygous mutation of the mitochondrial *c19orf12* gene. The patient was treated with deferiprone (10 mg/kg p.o. per day). MRI was performed prior to initiation of therapy and after 8 months using R2* relaxometry and QSM at 3T. Quantitative susceptibility maps were calculated from 3D high-resolution gradient-echo phase data with the HEIDI algorithm (5). R2* relaxometry was performed using a 2D multi-echo gradient-echo sequence with 5 echo times, 4mm slice thickness and 1mm gap. ROI analysis was performed by manually defined regions of the GP and SN using MRIcro (Chris Rorden, Atlanta, GA). QSM and R2* values were compared with respect to healthy volunteers (3f, 2m, 21-26 years) for QSM and (36f, 30m, 18-84 years) for R2*.

Results:
Measurements for GP before and during treatment were as follows: R2* 88 vs. 85/s, susceptibility 0.37 vs. 0.35 ppm suggesting an iron content of 30 vs. 27 mg/100g. For SN: R2* 59 vs. 66/s and susceptibility 0.43 vs. 0.42 ppm suggesting an iron content of 34 vs. 33 mg/100g. QSM and R2* values were much higher as compared to healthy adults (Fig.1).

Discussion and Conclusion:
R2* relaxometry and QSM allow for quantification and monitoring of the brain iron content. While QSM showed decreased iron content in GP and SN during iron-chelating therapy, R2* values of the SN increased (indicative of increased iron) and were generally underestimated as compared to GP (QSM showed higher values for SN as compared to GP). This may be due to partial volume effects of the 2D MRI sequence used for R2* relaxometry which does not allow an accurate investigation of small structures. Based on the stable iron content as assessed by QSM and R2* relaxometry and the absence of side effects, the patient continues chelating therapy at an increased daily dose of deferiprone (20 mg/kg p.o.).

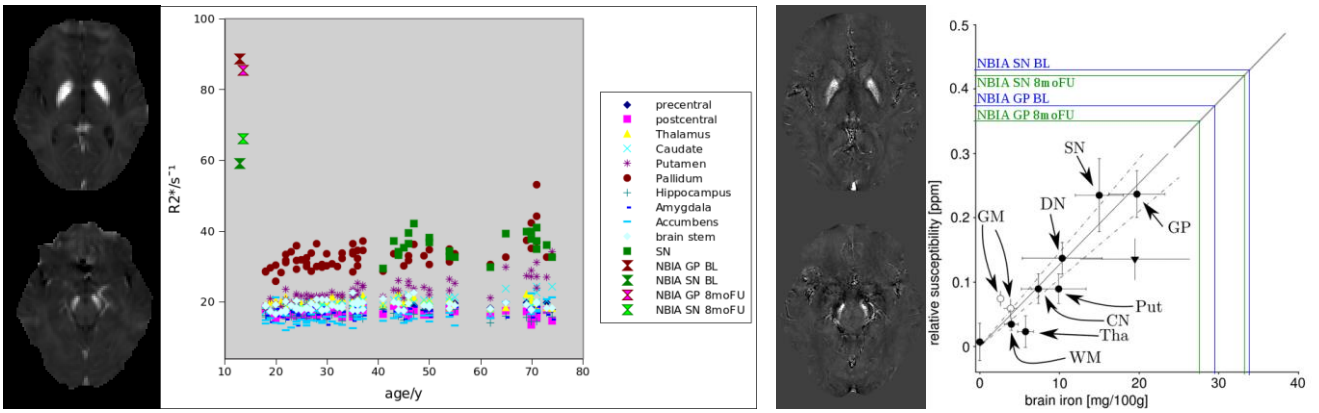

Fig.1: R2* maps and quantitative R2* values at baseline (BL) and 8 month follow up (8moFU) compared to normal controls (left) and QSM and quantitative susceptibility values in comparison with five healthy volunteers (right).

References: (1) Scheider SA et al. 2012, Mov Disord. 27:42, **(2)** Hartig M et al. 2011, Am J Hum Genet. 89:543, **(3)** Zorzi G et al. 2011, Mov Disord. 26:1756, **(4)** Schulte EC et al. 2013, Mov Disord. 28:224, **(5)** Schweser et al. 2012. Neuroimage.

The effect of dissolved oxygen on the magnetic susceptibility of blood

Avery J.L. Berman[1], Yuhan Ma[1], Richard D. Hoge[2], G. Bruce Pike[1]
[1]*Montreal Neurological Institute, McGill University,* [2]*IUGM/Université de Montréal*

Introduction: The paramagnetic nature of oxygen (O_2) can have significant effects on MR images; it creates large susceptibility differences between air cavities and tissue, and in turn, can lead to extensive areas of signal dropout. Despite this fact, in blood, the susceptibility of O_2 dissolved in plasma is commonly ignored since the amount of O_2 dissolved in plasma is normally very small and its contribution to the net susceptibility of blood is assumed negligible compared to that of the other major constituents – particularly deoxygenated red blood cells[1].

In a recent paper by Schwarzbauer and Deichmann (SD), the model of the susceptibility of blood was extended to include dissolved O_2[2]. SD theoretically predicted that when concentrations of dissolved O_2 in blood were sufficiently high, such as during the inhalation of elevated levels of O_2 (hyperoxia), dissolved O_2 would significantly contribute to the susceptibility difference between arterial blood and the surrounding tissue. Using their extended model and simulations, they found that in going from normoxia to hyperoxia, MR signal changes from arterial blood could be substantial and even comparable to venous BOLD contrast (where changes in the concentration of deoxyhemoglobin (dHb), not dissolved O_2, are the primary source of contrast). Traditionally, the model used to describe hyperoxic-induced signal changes was one where the reduction in paramagnetic dHb led to an increase in BOLD signal compared to baseline for veins and capillaries but no significant change for arteries[3]. Thus, the implications of SD's findings for fMRI studies using hyperoxia, such as calibrated BOLD, are profound and have led us to re-examine the model of the susceptibilities of blood and tissue proposed by SD.

Theory: For a mixture of substances in solution, such as in blood, the net volume magnetic susceptibility of the solution, $\chi_{V,net}$, is given by the weighted sum of the individual volume susceptibilities: $\chi_{V,net} = \sum \alpha_i \cdot \chi_{V,i}$, where the weighting factors, α_i, are the volume fractions of the substances in solution. In the SD model, the net susceptibility of blood, $\chi_{V,b}$, was divided into contributions from O_2, with a volume fraction α_{O_2}, and from red blood cells and plasma, with a volume fraction $1 - \alpha_{O_2}$. α_{O_2} was obtained from the plasmatic component of the blood O_2 content, given by the product $\varepsilon \cdot P_{O_2}$, where $\varepsilon = 3.1\times10^{-5}$ mL O_2/mL blood/mm Hg[4] is the solubility of O_2 in blood, and P_{O_2} is the partial pressure of O_2 in blood. However, the volume of O_2 in this particular expression is the volume the dissolved O_2 would occupy in the gaseous state at standard temperature and pressure (STP), it is *not* the physical volume occupied by dissolved O_2 in blood. In fact, when O_2 dissolves in a liquid such as plasma or water, the volume occupied by the O_2 in solution is orders of magnitude less than the volume occupied by the same number of moles in the gaseous state at STP. Therefore, SD's formulation severely overestimated α_{O_2}. Similarly, the susceptibility of tissue was divided into a baseline tissue component and a dissolved O_2 component with α_{O_2} again given by the product of the solubility of O_2 in blood and the P_{O_2} in tissue.

To compute the effect of dissolved O_2 on $\chi_{V,b}$, we first propose to simplify the problem by considering the O_2 dissolved in each water compartment of blood; specifically, the water in plasma and in red blood cells. The volume fractions can then be determined using data that is readily available, specifically, the mole fraction solubility of O_2 in water, $\bar{n}_{O_2:H_2O}$, as well as the partial molar volume of O_2 dissolved in water, $\bar{v}_{O_2:H_2O}$. For the range of P_{O_2} encountered under normoxia and hyperoxia, the dissolved O_2-water solution is very dilute, therefore, the partial molar volume of water can be approximated by the molar volume of water, v_{H_2O}. Using the terms listed above to compute α_{O_2}, we finally determine $\chi_{V,b}$ using a modified form of the susceptibility of blood provided by Spees *et al.*[1] whereby every appearance of the susceptibility of water, χ_{V,H_2O}, is replaced by $(1-\alpha_{O_2}) \cdot \chi_{V,H_2O} + \alpha_{O_2} \cdot \chi_{V,O_2}$. For the susceptibility of tissue, we use the same model as SD but with α_{O_2} in tissue computed using our formulation assuming tissue has the same solubility to O_2 as water.

Results: While there is a paucity of studies on the effect of dissolved O_2 on the susceptibility of either water or blood, a related experiment that measured the effect of dissolved O_2 in benzene was used to validate our formulation[5]. Using mole fractions and partial molar volumes of O_2 in benzene instead of water, our model predicted $\chi_{V,net}$ to within 0.2% and -10% of the experimentally measured values at a P_{O_2} of 665 mm Hg using the ^{1}H and ^{13}C resonances of benzene, respectively, versus 410% and 359% error using the SD model (where the mole fraction of O_2 was converted to the gaseous volume at STP). Given the good agreement between our formulation of the susceptibility and the measured values in benzene, one would expect similar results for dissolved O_2 in blood. Figure 1a shows the results of our formulation versus SD's formulation for the susceptibility of blood as a function of P_{O_2}. Figure 1b then shows how these susceptibilities correspond to the susceptibility differences, $\Delta\chi_V$, between blood and tissue along the vascular tree during hyperoxia and normoxia using the same physiological parameters as SD[2].

Conclusion: Although the susceptibility of blood is affected by the paramagnetic contribution from dissolved O_2 at elevated P_{O_2} (hyperoxia), the effect is far smaller according to our formulation than was originally suggested by SD. This results in a negligible change in the arterial blood-tissue $\Delta\chi_V$ going from normoxia to hyperoxia - unlike SD's result - and a change in the venous $\Delta\chi_V$ similar to that of SD's. This means that signal contrast will indeed be isolated to the venous and capillary sections of the cerebrovasculature during hyperoxia due to the decreased concentration of dHb alone - as was traditionally assumed. Furthermore, since the biophysical model of the BOLD signal used in hyperoxia-calibrated BOLD is dependent on contrast arising from dHb[3,6], the model is still valid since the paramagnetic effects of dissolved O_2 are negligible. Further experiments and simulations are being performed to verify these results.

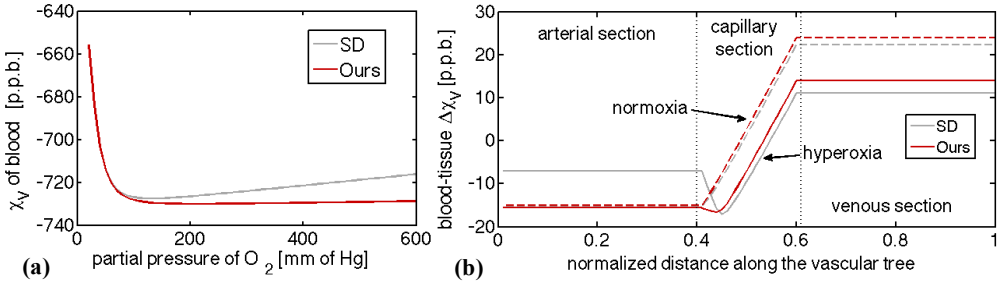

Figure 1: The volume magnetic susceptibility of blood as a function of P_{O_2} (a) and the resulting susceptibility difference between blood and tissue along the vascular tree (b). Both figures show comparisons of SD's formulation (grey) with our formulation (red). In (b), $\Delta\chi_V$ is shown for both formulations under hyperoxia (solid lines) and normoxia (dashed lines). In (b), the baseline oxygen extraction fraction was 0.35, hematocrit was 0.44, and arterial P_{O_2} was 110 mm Hg for normoxia and 550 mm Hg for hyperoxia.

References: [1] Spees *et al.*, MRM 45:533 (2001). [2] Schwarzbauer and Deichmann, NeuroImage 59:2401 (2012). [3] Mark *et al.*, NeuroImage 54:1102 (2011). [4] Severinghaus, J. Appl. Physiol. 46:599 (1979). [5] Delpuech *et al.*, JMR 36:173 (1979). [6] Hoge et al., MRM 42:849 (1999).

Quantitative Oxygenation Venography from MRI Susceptibility

Audrey P Fan[1,2], Berkin Bilgic[1,2], Louis Gagnon[1,2], Thomas Witzel[2], Himanshu Bhat[3], Bruce R Rosen[2], Elfar Adalsteinsson[1,2]

[1]Massachusetts Institute of Technology, Cambridge MA; [2]Athinoula A. Martinos Center for Biomedical Imaging, [3]Charlestown MA; Siemens Medical Solutions, Charlestown MA.

Purpose. The aim of this work is to address an unmet clinical need for noninvasive imaging of brain oxygenation in neurological disorders such as stroke and tumor [1]. MRI phase can be used to quantify oxygen saturation (SvO_2) in individual veins from the deoxyhemoglobin-induced susceptibility shift between vessels and brain tissue [2,3]. However, model-based SvO_2 imaging from phase is currently restricted to vessel segments with a limited range of orientations, preventing clinical use of the technique across the brain. Here we address these limitations and introduce quantitative oxygenation venograms that map SvO_2 along the brain vasculature.

Methods. *Acquisition*. We implemented a 3D gradient echo sequence with flow-compensation along each axis at all echoes [4]. Axial images were collected in three healthy volunteers with a 32-channel coil on a Siemens 3T Trio system (TR=14ms; TE=8.1, 20.3ms; resolution= 0.6x0.6x0.6mm^3; matrix= 384x336x224; BW= 260Hz/pixel) and phase images were reconstructed offline.

Susceptibility mapping. Phase images were spatially unwrapped with FSL Prelude [5] and background field was estimated by projection onto dipole fields for removal [6]. Quantitative susceptibility maps (χ) were then reconstructed with ℓ_1-regularization [7], which minimizes $||\mathbf{F}^H\mathbf{D}\mathbf{F}\chi - \boldsymbol{b}||_2^2 + \lambda \cdot |\mathbf{G}\chi|_1$. Here, b is the measured local field map, $D=1/3 - k_z^2/k^2$ is the dipole kernel in k-space, G is the gradient operator, F is the Fourier transform, and the weighting $\lambda=4.5\cdot10^{-4}$ was chosen by the discrepancy principle [8].

Vessel graphing. Venous structures in χ maps (thresholded at χ>0.15) were vectorized into a graph of nodes and edges by the Volumetric Image Data Analysis (VIDA) software (***Fig 1***) [9]. The graphed output was rendered into a volumetric mesh, or venogram, with accurate vessel thickness. **SvO_2**= $1-\Delta\chi_{vein\text{-}CSF}/(0.27ppm\cdot Hct)$ was averaged along each connected vein segment without branching and displayed in the venogram. Vein tilt angle was computed for each segment from the graph coordinates.

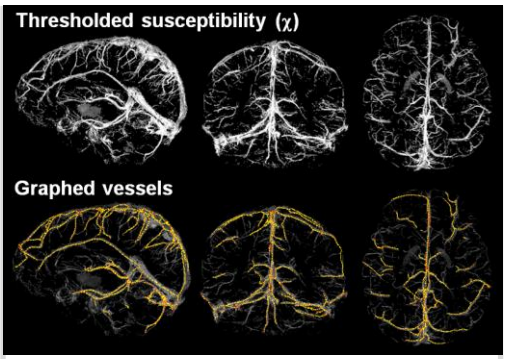

Fig1. Maximum intensity projection of QSM map (χ>0.15) and graphed venous vasculature.

Results. Quantitative SvO_2 venograms were created for each volunteer, from which we identified SvO_2 (%) in major anatomical vessels (***Fig2***). Mean SvO_2 from QSM (66.1±5%) was consistent with SvO_2 from model-based MR susceptometry (65.8± 4%) [3] for vessels parallel to the main field (B_0) in vivo (***Fig3***).

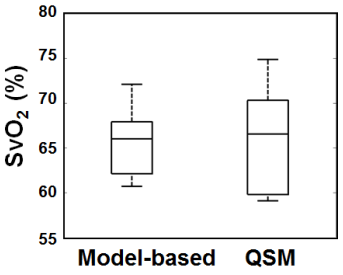

Fig3. Mean SvO_2 for 10 parallel vessels was not different between QSM and model-based MR susceptometry (p=0.91) in one healthy volunteer.

Marked improvement in SvO_2 accuracy was achieved for veins that were not parallel to B_0 through use of QSM. Mean SvO_2 in vivo varied between 64.3 and 69.1% across all vein tilt angles (***Fig4b***), which is consistent with <10% error over all tilt angles found in simulation (***Fig4a***). SvO_2 estimates from QSM exhibited substantially less angle-dependent variation compared with >15% error for tilt angles >40° observed in model-based MR susceptometry [10]. Future work aims to address residual SvO_2 bias for veins oriented at tilt angles which are severely undersampled by the dipole kernel (asterisks, ***Fig4a***); through use of priors based on vascular anatomy in the QSM reconstruction.

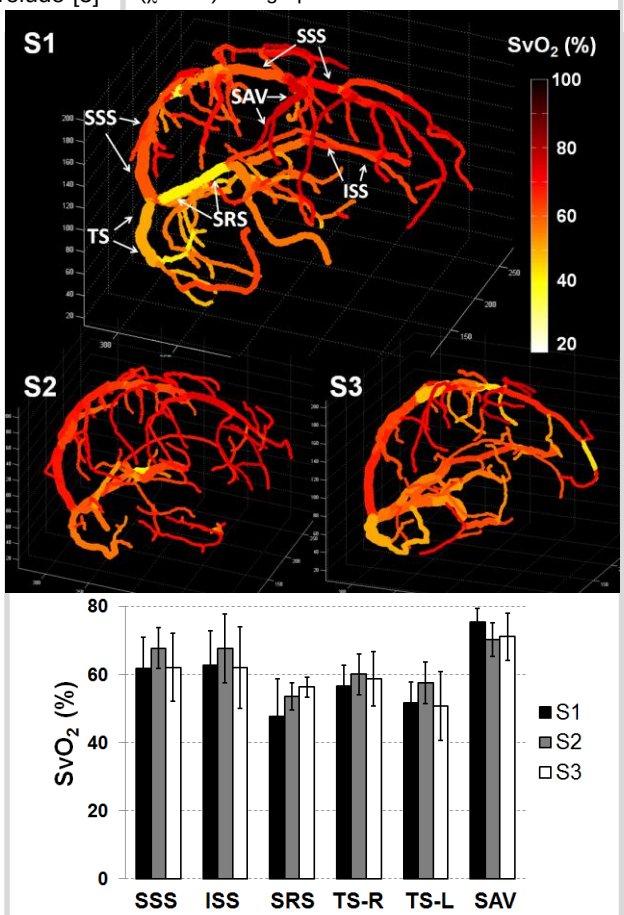

Fig2. Quantitative SvO_2 (%) mapped on venograms in three healthy volunteers. *In vivo* SvO_2 values are shown for superior (SSS) and inferior sagittal sinus (ISS), straight sinus (SRS), right and left transverse sinus (TS), and superior anastomic vein (SAV) for each subject.

Conclusion. Venograms which allow radiologists to directly read oxygenation along vessels of arbitrary orientation are shown for the first time, and may facilitate clinical use of SvO_2 imaging.

References. [1] Christen, *Am J Neuroradiol* 2012. [2] Fan, *Magn Reson Med* 2012. [3] Haacke, *Human Brain Mapp* 1997. [4] Deistung, *J Magn Reson Imag* 2009. [5] Jenkinson, *Magn Reson Med* 2003. [6] Liu, *NMR Biomed* 2012. [7] Bilgic, *Neuroimage* 2011. [8] Tsai, *J Neurosci* 2009. [9] Hansen *SIAM* 1998. [10] Li, *Magn Reson Med* 2012.

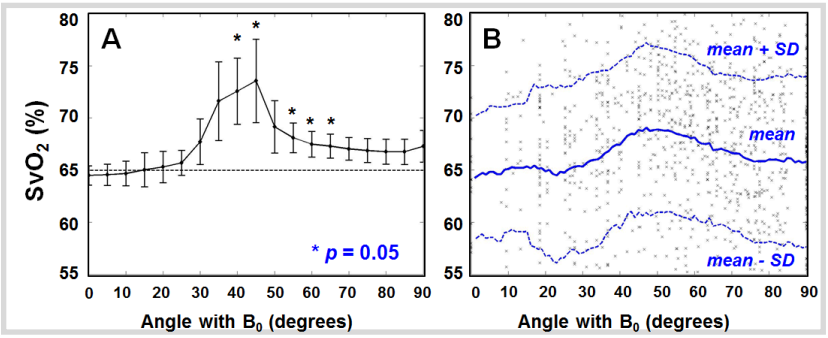

Fig4. Mean SvO_2 across vessel tilt angle from QSM in (a) numerical simulation and (b) in vivo for one healthy volunteer. Less than 10% SvO_2 error was observed across all angles in numerical simulation; mean SvO_2 ranged from 64.3-69.1% across vessel tilt angles in vivo. →

Effects of supplemental oxygen in QSM

Pinar S. Özbay[1, 2], Cristina Rossi[1], Manuel Redle[1], Roman Kocian[3], Klaas P. Prüssmann[2], Daniel Nanz[1]
[1]Diagnostic and Interventional Radiology, University Hospital Zürich [2]Institute of Biomedical Engineering, ETH Zürich
[3]Anesthesiology, University Hospital Zürich

Background/Purpose:

Inhalation of pure oxygen results in a lower deoxyhaemoglobin (dHb) / oxyhaemoglobin (oxy-Hb) ratio in venous blood and, therefore, in the neighborhood of veins, in lower susceptibility gradients and a higher signal in T2*-weighted images. The effects were demonstrated, among others, in Susceptibility Weighted Imaging (SWI) studies [1].
On the other hand, molecular oxygen, e.g., gaseous in skull cavities or dissolved, e.g. in the CSF, is paramagnetic and expected to induce opposite effects in corresponding regions [2]. Higher concentrations of paramagnetic oxygen dissolved in CSF under hyperoxia have been shown to cause incomplete CSF-signal suppression in standard T1w FLAIR imaging, which should be taken into account in studies under anesthesia. [3]. Quantitation of hyperoxia-induced effects is of pivotal interest in connection with calibration of the fMRI signal change, and when understanding opposite BOLD-signal trends in different regions of the brain [4, 5]. In both areas, QSM may yield to a degree independent information on oxygen saturation levels.
Here, we attempted to quantify susceptibility changes in the human brain that result from inhalation of molecular oxygen as assessed by QSM.

Methods:

3D T2*-weighted-multi-gradient-echo images of two healthy volunteers were acquired on a 3T system (age range: 23-26, FA=50°, TR=71ms, TE=3, 19, 35, 51, 67ms, isotropic voxel dimensions=1.8mm, matrix size: 128x128x65) while breathing medical air (normoxia) or pure oxygen (hyperoxia), respectively.
A whole-brain mask and tissue-segmentation masks were generated based on magnitude images at shortest TE with FSL/BET [6] and FSL/FIRST [7], respectively. Weighted phase increments per ΔTE (WPI) were calculated and their laplacian [8] was masked with the whole-brain mask. These "WPI_{LM}" images were point-wise divided in Fourier-space with a Fourier-transformed Laplacian kernel (threshold parameter σ = 0.08) to obtain unwrapped and high-pass filtered SHARP phase images [9]. SHARP images under hyperoxia were registered to those under normoxia with FSL/FLIRT [10, 11]. Quantitative Susceptibility Maps were calculated with an inverse regularization algorithm [12] and a threshold parameter α = 0.2. Susceptibility values (ΔX) were referenced in relation to that of frontal white matter (Fig1 e), which was defined to be zero. QS maps were segmented using tissue-segmentation masks. WM, GM and CSF ROIs were placed in segmented QS maps; values inside the ROIs, but outside the current segment of interest, were not included in the calculation of mean susceptibility values.

Results:

QS maps (b-e: FSL-segmented) are shown in Fig. 1, for one volunteer under normoxia. Average ΔX ROI values under normoxia and hyperoxia are given in Table 1 and plotted in Fig. 2. The normoxia values were in good agreement with literature values [13]. In grey matter hyperoxia generally induced lower susceptibility values compared to normoxia. In venous blood, ΔX values were significantly lower while increased values were found in CSF.

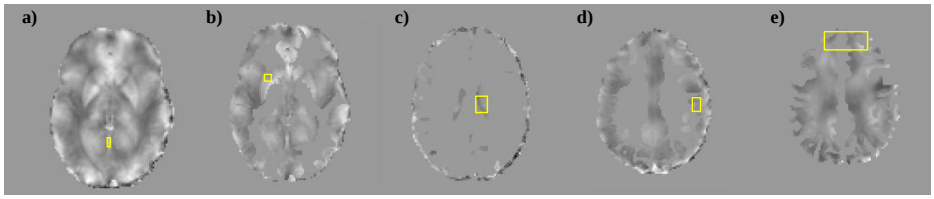

Fig1. Quantitative Susceptibility Maps, for one volunteer under normoxia, yellow squares show ROI selections a) vein b) putamen c) CSF d) grey matter e) white matter

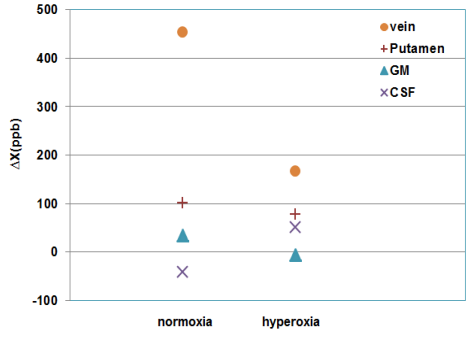

Fig2. ΔX values (y-axis) in ppb under normoxia and hyperoxia

Table1. Average ΔX ROI values, in ppb, in vein, putamen, GM and CSF under norm- and hyperoxia.

	vein	putamen	grey matter	CSF
normoxia	454	101	34	-41
hyperoxia	167	78	-6	50

Conclusion: Inhalation of molecular oxygen results in significantly more reduced susceptibility values in cerebral veins and gray matter than the change in the reference frontal white matter, however with a regional variation that most likely strongly depends on the relative distances from veins, oxygen-filled cavities and CSF with dissolved molecular oxygen. QSM might lead to an improved understanding in several research areas dealing with oxygenation-level variations.

References: [1] Rauscher et. al, MRM 54:87–95 (2005) [2] Pilkinton et. al, MRM, 66:794–801 (2011) [3] Mark et. al, NeuroImage 54:1102–1111, (2011) [4] Anzai et. al, AJNR 25:274–279, (2004) [5] Bianciardi et. al, Journal of Cerebral Blood Flow & Metabolism, 31:401–412 (2011) [6] Smith et. al, HBM 17(3):143-155, 2002. [7] Patenaude et. al, NeuroImage, 56(3):907-922 (2011) [8] Schofield et. al, OPTICS LETTERS 28(14):1194-95 (2003) [9] Schweser et. al, MRM 2012 [10] Jenkinson et. al, Medical Image Analysis, 5(2):143-156, 2001. [11] Jenkinson et. al, NeuroImage, 17(2):825-841, 2002 [12] Haacke et. al, JMRI 32:663–676 (2010) [13] Tang et. al, MRM (2012)

Functional QSM at 9.4T with single echo gradient-echo and EPI acquisition

Dávid Balla[1], Philipp Ehses[1,2], Rolf Pohmann[1], Juliane Budde[1], Christian Mirkes[1,2], G. Shajan[1], Richard Bowtell[3], Klaus Scheffler[1,2]

[1]High-field MR Centre, Max Planck Institute for Biological Cybernetics, Tübingen, Germany, [2]Department of Biomedical Magnetic Resonance, University of Tübingen, Tübingen, Germany, [3]Sir Peter Mansfield Magnetic Resonance Centre, University of Nottingham, Nottingham, United Kingdom

Background/Purpose: Functional QSM (fQSM) was recently proposed for the analysis of gradient-echo (GE) BOLD contrast acquired using zoomed EPI time-series at 7T [1,2]. Here we present fQSM and fMRI activation maps, obtained at 9.4T from full coverage GE-EPI and single echo "shifted" gradient-echo (esGRE) [3] experiments. The goal of this project was to test different acquisition strategies and optimize MR parameters for fQSM at 9.4T.

Methods: Experiments were performed on a 9.4T system equipped with a custom-built 16-channel transmit-coil and a 31-channel receive-array helmet [4]. The visual stimulation for fMRI consisted of a flickering checkerboard disk stimulus on a grey background. The motor-task was tapping of the thumbs of both hands with the four other fingers in quick cyclic runs. Both paradigms are expected to produce positive BOLD contrast in respective cortical areas in the magnitude time-series. Acquisition strategies: (1) esGRE sequence with interleaved slices [3] providing distortion-free T2*-weighted images with a TE of 18.7ms and a TR of 90ms; further parameters were: 1mm isotropic resolution, 12 slices, volume TR = 4.32s, 140 repetitions and 3-fold acceleration; (2) gradient-echo EPI (GE-EPI) with 1mm isotropic resolution, 28 slices, TE/TR = 25ms/3s, 200 repetitions and 3-fold acceleration. Processing included the offline reconstruction of magnitude and phase images from the multichannel, accelerated raw data in Matlab, followed by phase unwrapping [5], motion correction [6], temporal filtering for EPI [7], background field removal [8] and QSM calculation with thersholded k-space division (TKD) [9]. Activation maps were calculated using uncorrected T-test with $p<0.015$.

Results: The esGRE-fQSM and GE-EPI-fQSM activation maps presented in the figure (a), (c) and (e) demonstrate high sensitivity by showing supra-threshold values that are coincident with significant voxels in the corresponding fMRI maps, (b), (d) and (f). The noise in the maps is a result of the simple statistics, which deliberately avoided clustering, spatial smoothing etc. esGRE vs. GE-EPI: Pros esGRE – high structural fidelity (specificity) of fQSM and fMRI and simple data handling after acquisition due to minimal distortions (e.g. spatial registration is unproblematic). Cons esGRE – frequent application of the excitation pulse results in in-flow effects. Pros GE-EPI – the gain in contrast sensitivity due to signal sampling efficiency and the possibility to use long echo times. Cons GE-EPI – geometrical distortions and time varying ghost artifacts render spatial registration (e.g. at high spatial scale) difficult.

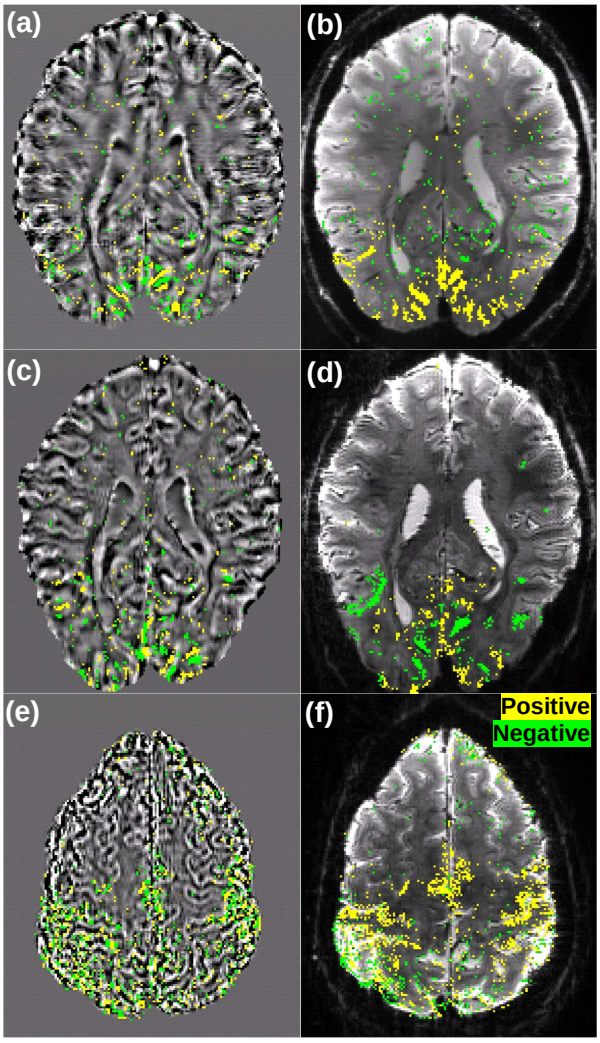

Conclusion: Functional QSM is feasible for data acquired with GE-EPI at 9.4T. Relative to previous studies, we presented data with full transverse brain coverage and proposed the fast esGRE acquisition technique as a useful alternative to GE-EPI, especially for fQSM at ultra-high fields.

References: [1] Balla et al. (2012) ISMRM #325; [2] Balla et al. (2013) ISMRM #300; [3] Ehses et al. (2012) ISMRM #329; [4] Shajan et al. (2013) MRM in press; [5] Schofield and Zhu (2003) Optics Lett. 28:1194; [6] Jenkinson et al. (2002) NeuroImage 17:825; [7] Hagberg et al. (2012) Neuroimage 59:3748; [8] Schweser et al. (2011) Neuroimage 54:2789; [9] Wharton et al. (2010) MRM 63:1292

Figure: Thresholded statistical significance maps of positive (yellow) and negative (green) contrast changes, projected onto the preprocessed average of the time-series. (a) esGRE-fQSM, (b) esGRE-fMRI, (c) GE-EPI-fQSM and (d) GE-EPI-fMRI during visual stimulation (T>2.3, same slice); (e) GE-EPI-fQSM and (f) GE-EPI-fMRI during motor activity (T>4).

March 25th 2013

Cerebral Metabolic Rate of Oxygen ($CMRO_2$) Quantitative Mapping Using Quantitative Susceptibility Mapping (QSM)

Jingwei Zhang[1], Tian Liu[1], Ajay Gupta[1], Pina C. Sanelli[1], Cynthia Wisnieff[1], Pascal Spincemaille[1], and Yi Wang[1]
[1]*Department of Radiology, Weill Medical College of Cornell University, New York, NY, United States*

Background/Purpose: Accurate measurement of cerebral metabolic rate of oxygen (CMRO2) is highly desired for the assessment of brain cell function in health and in stroke. $CMRO_2$ and the associated derived measure of oxygen extraction fraction, are known to be important markers of neuronal function, with elevations in oxygen extraction fraction (OEF) known to be a strong marker for stroke risk in patients with cerebral vascular occlusive diseases. Recently, a rigorous deconvolution technique called quantitative susceptibility mapping (QSM) has been developed to map tissue susceptibility. We propose to use QSM to map the concentration of paramagnetic deoxyhemoglobin [dHb] and hence $CMRO_2$.

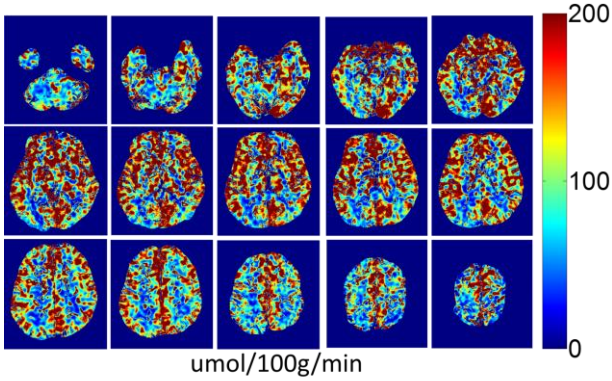

Fig.1. $CMRO_2$ maps for subject #1.

Theory: $CMRO_2$ is defined as the rate at which O_2 is consumed in the brain by metabolic processes. According to Fick's principle and oxygen mass conservation, we have $\mathbf{CMRO_2 = 4 * CBF * ([dHb]_v - [dHb]_a)}$, where CBF is cerebral blood flow (ml/100g/min), $[dHb]_v$ and $[dHb]_a$ represent dHb concentrations (umol/ml) in the draining vein and supplying artery respectively, and 4 accounts for 4 hemes per Hb with one oxygen molecule per heme. $[dHb]_a$ can be estimated as the product of arterial oxygen saturation (SpO_2) and hemoglobin concentration in the blood, [Hb]: $\mathbf{[dHb]_a = (1-SpO_2)*[Hb]}$. $[dHb]_v$ can be estimated by modeling the magnetic volume susceptibility of brain tissue with blood and bloodless tissue as the major components with their reported volume susceptibility values. We use SI units throughout. The volume susceptibility will be relative to water unless otherwise notice.

Table 1: $CMRO_2$ ROI measurement on gray matter, median±IQR

Subject #	CMRO2 (umol/100g/min)
1	123 (80-185)
2	115 (81-160)
3	118 (70-195)
4	123 (67-217)
5	126 (68-227)
6	116 (83-161)
7	122 (72-197)

$\chi_{QSM} = \lambda*\{[dHb]_v*4*\chi_{MDeoxyHeme} + [Hb]*\chi_{MGlobin} - [Hb]*V_{MHb}*\chi_{water}\} + \chi_0$, where χ_{QSM} is the susceptibility of voxels measured on QSM. χ_0 is the susceptibility of bloodless tissue within the voxels. λ is the volume fraction of blood within the voxels estimated from CBF[1]: $\lambda = (0.227*CBF - 7.27)/100$. V_{MHb} is the molar volume of Hb in solution. χ_{water} is the susceptibility of water relative to vacuum. $\chi_{MDeoxyHeme}$ and $\chi_{MGlobin}$ are the molar susceptibility of deoxygenated heme and globin protein respectively relative to vacuum[2]. Solved for CMRO2, we have

$$\mathbf{CMRO_2} \approx 4 * \mathbf{CBF} * \left[\frac{\chi_{QSM} - \chi_0 + \lambda*[Hb]*(V_{MHb}*\chi_{water} - \chi_{MGlobin})}{\lambda*4*\chi_{MDeoxyHeme}} - (1 - \mathbf{SpO_2}) * [\mathbf{Hb}]\right]$$

If QSM and CBF are both measured for two brain states that have different CBFs but the same CMRO2, CMRO2 can be determined as:

$$CMRO_2 = \frac{CBF_1 * CBF_2}{\lambda_1 * CBF_2 - \lambda_2 * CBF_1} * \frac{(\chi_{QSM1} - \chi_{QSM2}) + (\lambda_1 - \lambda_2)*[Hb]*[V_{MHb}*\chi_{water} - \chi_{MGlobin} - (1 - SpO2)*4*\chi_{MDeoxyHeme}]}{\chi_{MDeoxyHeme}}$$

Methods: Experiments were performed on healthy volunteers (N=5) on 3.0-T scanner (GE Healthcare). To achieve two brain states of the same CMRO2 but different CBF, all volunteers drank 20 ounces of iced coffee containing 0.2g caffeine. QSM was performed using a multi-echo 3D gradient echo (GRE) sequence (matrix size: 512×512×50, FOV: 240 ×240 mm2, slice thickness: 3 mm, 11 echoes, TE range from 4.3ms to 52.4ms equally spaced), and CBF was acquired using an ASL sequence (matrix size: 512×512×50, FOV: 240 ×240mm2, slice thickness: 3.8mm). QSM images were obtained from GRE data using the Morphology Enabled Dipole Inversion (MEDI) algorithm[3]. CBF images were obtained from ASL data. QSM and CBF were measured before and 35 minutes after the consumption of the coffee, and all images were co-registered to their corresponding pre-coffee QSM image coordinates. $CMRO_2$ maps were generated using method described above.

Results: From pre-to post-coffee, CBF values decreased about 40% in cerebral cortex in all volunteers ($p<0.001$). Examples of $CMRO_2$ in color are shown in Fig.1. The gray matter ROI measurements on CMRO2 maps are listed in Table 1.The results are consistent with values reported in prior papers[2].

Conclusion: This new QSM method for $CMRO_2$ mapping also demonstrates great clinical potential. The scans do not require contrast agent, breath holding, ECG gating, or CO_2 inhalation. The choice of drug challenge mechanism is flexible. Our preliminary data show that QSM is a promising method for determining [dHb] and then $CMRO_2$ mapping.

References: [1] Leenders, K.L. et al, Brain 113, 27-47, 1990. [2] Spees, W.M., et al, Magn Reson Med 45, 533-542. [3] Liu J, et al, NeuroImage 59:2560-8, 2012.

Rapid Background Phase Removal using Double-Echo Data

Saifeng Liu[1], Sagar Buch[1], and E. Mark Haacke[1,2]
[1]School of Biomedical Engineering, McMaster University, Hamilton, Ontario, Canada. [2]Department of Radiology, Wayne State University, Detroit, Michigan, United States

Introduction: Background phase removal is a critical step in quantitative susceptibility mapping (QSM)[1-4]. In most approaches, phase unwrapping is required, but phase unwrapping is sensitive to the presence of noise and is often time-consuming[2,3]. Any error in phase unwrapping will propagate into the QSM[5, 6]. Although phase unwrapping can be avoided using the Laplacian operator in SHARP, the accuracy of SHARP will be reduced, especially for regions near the edges of the veins [6,7]. We propose to bypass the normal phase unwrapping step using double-echo data.

Methods: The critical step in SHARP is to remove the unwanted background phase variations through a convolution process providing a phase image $\boldsymbol{\Phi'}$ which is essentially the difference between the phase value of a given pixel and the local average phase value. We propose using a moving baseline phase shift to create local regions of no aliasing. We calculate $\boldsymbol{\Phi'}$ only for those pixels which are sufficiently far away from any phase wraps. For the pixels which are close to phase singularities, $\boldsymbol{\Phi'}$ can be calculated through complex division between every pixel and the center pixel in the local spherical VOI. In this work, we set $\boldsymbol{\Phi'}$ to zero at the origin of any phase singularities. Combining all the steps, $\boldsymbol{\Phi'}$ was obtained and the local phase $\boldsymbol{\Phi_L}$ could be extracted from $\boldsymbol{\Phi'}$ through the usual SHARP deconvolution process. In the above calculations, it is assumed that the maximal phase change is less than 2π locally. This is satisfied when TE is short.

To test the proposed method, *in vivo* data was collected using a double-echo gradient echo sequence, with B_0=3T, TE_1=7.8ms, TE_2=20.8ms, resolution =0.5x0.5x1mm^3, matrix size=448x336x128, BW_1=399Hz/voxel, BW_2=100Hz/voxel, TR=30ms, FA=15^o. The brain mask was obtained using BET[8] in FSL. The singularities in the phase images were determined using the method outlined in (9). The phase at TE_1 was processed first to get $\boldsymbol{\Phi_L}(TE_1)$**.** Then the complex divided phase at TE_2-2TE_1=5.2ms was used to obtain $\boldsymbol{\Phi_L}(TE_2\text{-}2\cdot TE_1)$**.** Finally, $\boldsymbol{\Phi_L}(TE_2)$ was calculated as $\boldsymbol{\Phi_L}(TE_2\text{-}2\cdot TE_1)+2*\boldsymbol{\Phi_L}(TE_2)$**.** The radius of the spherical kernel in SHARP was kept to 6 pixels and the deconvolution was done through TSVD with a regularization threshold of 0.05. To compare the results, phase images at TE_2 were also unwrapped using Prelude in FSL[10] in 2D mode, and then processed using SHARP.

Results:

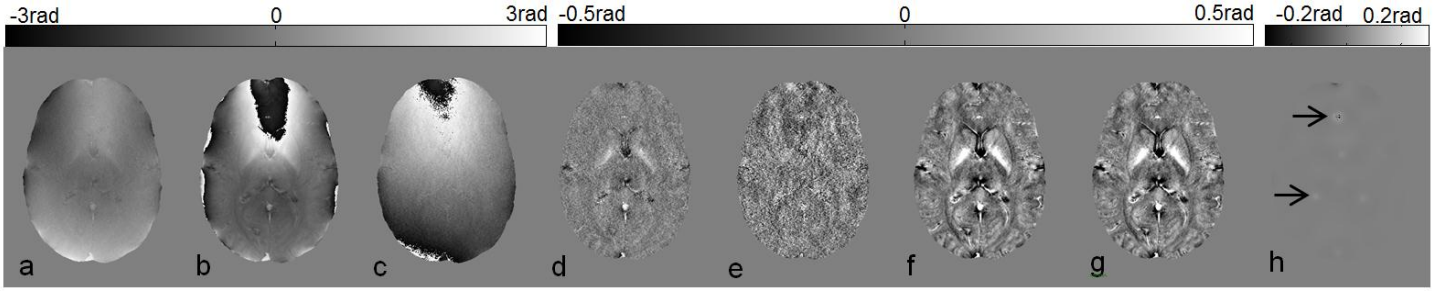

Figure 1. a) phase image at TE_1; **b)** phase image at TE_2; **c)** complex divided phase with an effective echo time of TE_2-2*TE_1; **d)** $\boldsymbol{\Phi_L}(TE_1)$ obtained from **a**; **e)** $\boldsymbol{\Phi_L}(TE_2\text{-}2TE_1)$ obtained from **c**; **f)** $\boldsymbol{\Phi_L}(TE_2)$ calculated as **e+2d**; **g)** $\boldsymbol{\Phi_L}(TE_2)$ obtained using SHARP with unwrapped phase at TE_2; **h)** difference between **f** and **g.** The major differences seen in **h**, (black arrows), are caused by the presence of phase singularities.

As shown in Figure 1, the local phase shifting approach yields effectively the same results as having performed a global phase unwrapping. The total computation time for the double echo data was around 2 minutes when the 2D phase unwrapping algorithm is used, and will be much longer if 3D phase unwrapping was applied. But the 2D phase unwrapping fails to unwrap the phase images completely. On the other hand, using the proposed method, the computation time is comparable to the 2D phase unwrapping algorithm, and the local phase of the whole brain was extracted properly.

Discussion and Conclusions: The robustness of QSM data processing is usually hampered by phase unwrapping, especially with the presence of phase singularities. A short echo time makes it possible to avoid much of the phase unwrapping problem, but short TE lowers the phase SNR and thus the susceptibility SNR in QSM. In the proposed algorithm, phase unwrapping at the longer TE was avoided by utilizing the shorter TE echo data to create an effective short TE from which one could locally correct for any possible aliasing. The proposed algorithm leads to almost the same result as SHARP with phase unwrapping but now the advantage of this method becomes more apparent as the phase singularities are properly handled (except for regions where the field is changing too rapidly, which remains a problem in both methods). In conclusion, the proposed algorithm helps to improve the efficiency and robustness of QSM.

References: [1] Neelavalli et al. JMRI(2009) 29:937–948; [2] Liu et al. NMR Biomed (2011) 24: 1129–1136; [3] Schweser et al. NeuroImage 54 (2011) 2789–2807; [4] Tang et al. MRM 2012 Jun 26; [5] Liu et al. MRM (2013) 69(2):467-76. [6] Schweser et al. MRM (2012) July 12. [7] Wu et al. MRM (2012) 67:137-147 [8] Smith, Human Brain Mapping (2002) 17(3):143-155. [9] Cusack et al. NeuroImage (2002) 16, 754-764 [10]Jenkinson, MRM (2003) 49:193-197.

Removal of Background Field Using Relaxation Method

Dong Zhou[1], Tian Liu, Pascal Spincemaille[1], and Yi Wang[1,2]
[1]*Department of Radiology, Weill Cornell Medical College, New York, New York, USA*
[2]*Department of Biomedical Engineering, Cornell University, Ithaca, New York, USA*

Background/Purpose: In quantitative susceptibility mapping (QSM), the magnetic susceptibility is mapped out by solving the field-to-source inverse problem using the phase data. Since only the tissue property is of interest, elimination of magnetic field caused by non-tissue sources is required [1,2,3]. This procedure, known as background removal, directly affects the calculated susceptibility values [4]. It is also a required pre-processing procedure for susceptibility weighted imaging [5].

Theory: The background field f_B satisfies Laplace's equation $\Delta f_B = 0$ and existing methods such as PDF and SHARP can be viewed as solvers for this partial differential equation (PDE). Here we solve the background field removal problem by directly solving the boundary value problem of the PDE using relaxation methods. Since the boundary values are not easily available, we make the approximation that $f_B = f_T$ on ∂M using the fact that the local field is typically one or two orders of magnitude smaller than the background field. Here ∂M denotes the boundary of the region of interest (ROI) and f_T denotes the total field. Laplace's equation is a well studied elliptic PDE and its boundary value problems can be solved successfully by various schemes such as finite difference methods, spectral methods, and finite element methods [6]. In this work, we use the successive over relaxation method.

Methods: Brain data of healthy subject is acquired using the gradient echo pulse sequence on GE 3T scanner with the following parameters: matrix size 256x256x116, voxel size 0.9375x0.9375x1.2 mm, FOV= 240 mm, flip angle 20, receiver bandwidth 62.5 kHz, 7 echoes, TE1 = 2.8 ms, TE = 5 ms, TR = 37.5 ms. For the SHARP method, a spherical averaging with radius 6 mm and a k-space kernel threshold 0.01 are used.

Results: In Figure 1, we show the local field f_L calculated from three different background removal methods: the SHARP method [8], the PDF method [2, 4], and the proposed relaxation method. For comparison purpose, the DC component of the local field is removed. Due to the spherical mean averaging used in the SHARP method, its calculated brain region is smaller. The three results show overall agreement on tissue structures while differences are mostly evident on the ROI boundaries. These differences are likely to be associated with the erroneous phase values near the ROI boundaries due to low signal-to-noise ratio and imperfect phase unwrapping.

Conclusion: We propose a new method to remove the background field by solving the PDE of the background magnetic field assuming simple boundary conditions. Preliminary results show that anatomic structural information is preserved from this procedure. Clarification of the subtle differences between the relaxation method and the existing methods will be included in a separate publication.

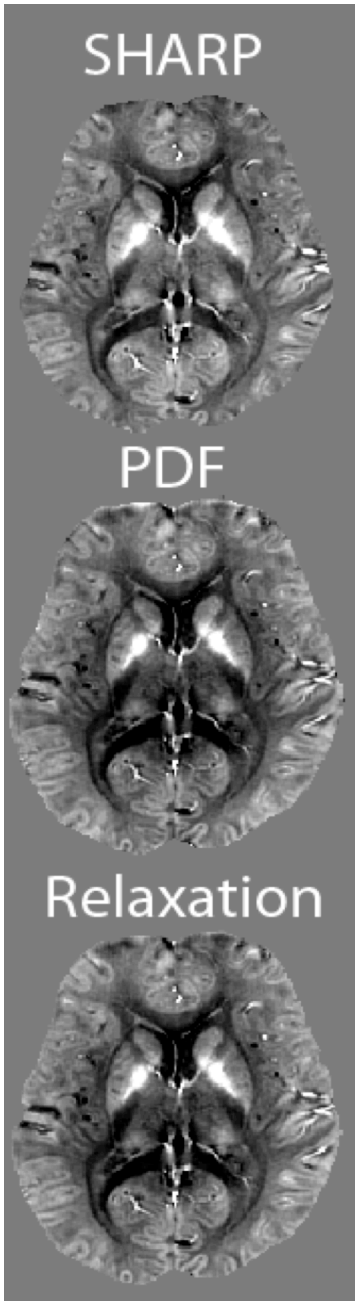

Figure 1. Local magnetic field from different methods.

References: [1] Marques and Bowtell 2005, Concepts in MR Part B (25) 65; [2] Liu et.al. 2011, NMR in biomedicine (24) 1129; [3] Schweser et.al. 2011, NeuroImage (54) 2789; [4] Wharton et.al. 2010, MRM (1304) 1292; [5] Haacke 2004 MRM (52) 612; [6] Press et.al. 2007, Numerical Recipes 3rd edition.

Edge-Extended Harmonic Phase Processing Incorporating Priors

Ryan Topfer[1, 2], Hongfu Sun[2], Alan H Wilman[1, 2]
[1]*Department of Physics,* [2]*Department of Biomedical Engineering, University of Alberta*

Background/Purpose: As inversion strategies for susceptibility mapping become ever more refined, how to best "pre-process" the field maps remains an open question. To isolate for the local field of interest, Sophisticated Harmonic Artifact Reduction for Phase Data (SHARP) [1] and Projection Onto Dipole Fields (PDF) [2] proceed in different ways to arrive, nevertheless, at similar results. A common pitfall to the two techniques is their failure to accurately map local field near the edges of the brain (e.g. cortex). Fortunately, since the background field is harmonic it is also, *ipso facto*, analytic (i.e. equal to its Taylor series representation). Hence, following SHARP by a three-dimensional Taylor expansion of the background field admits a recovery of the otherwise lost edge voxels [3]. However, given that the series expansion must be truncated and, furthermore, that the SHARP-filtered field is itself an estimation based on noise-corrupted measurements, a robust processing scheme should account for variable uncertainty in the field estimation. The addition of a phase regularization step in SHARP has been proposed [4]. Here, we employ a Taylor series expansion to recover edge voxels in the SHARP phase and impose a prior (model constraint) to further improve phase output.

1. $J_{SoS} = \left\| \boldsymbol{W_{SoS}} (\bar{\boldsymbol{I}} \varphi_{\text{local}} - \tilde{\varphi}_{\text{local}}) \right\|_2^2$
2. $\varphi^{EP} = \varphi^{IP} + \boldsymbol{d}^{\boldsymbol{T}} \boldsymbol{G}(\varphi^{IP}) + \frac{1}{2} \boldsymbol{d}^{\boldsymbol{T}} \underline{\boldsymbol{H}}(\varphi^{IP}) \boldsymbol{d}$
3. $J_{TC} = \left\| \boldsymbol{W_{TC}} \left(\bar{\boldsymbol{I}} \varphi_{\text{local}} - \widetilde{\Delta \varphi}_{\text{local}} \right) \right\|_2^2 + \lambda \sum_{n=1}^{N} \ln\left(1 + \frac{(\boldsymbol{\varphi_{local,n}} - \varphi_{\text{o}})^2}{2\boldsymbol{\sigma^2}}\right)$

Methods: Whole-head data were acquired at 4.7 T using a 2D susceptibility-weighted protocol. Magnitude data from the 4-element receiver were combined via sum-of-squares (SoS) and passed to FSL's Brain Extraction Tool [5] to form a binary tissue mask defining the ROI. Channel specific phase data were SHARP-processed individually: phase (masked and unwrapped [6]) was spherical mean value (SMV) filtered [7] (kernel radius 6 mm). Conventional SHARP images were formed for each channel (threshold parameter = 0.05) and combined via magnitude-weighted SoS. This is equivalent to minimizing cost function J_{SoS} (Equation 1) where $\boldsymbol{W_{SoS}}$ is a diagonal weighting matrix with entries equal to the channel magnitude data, $\tilde{\varphi}_{\text{local}}$ is the augmented vector formed by vertically concatenating the local phase estimates from each channel; $\bar{\boldsymbol{I}}$ is the stacked identity matrix (4N rows by N columns, where N is the number of voxels); and φ_{local}, the solution vector, is the channel-combined local phase.

For our proposed method, the SMV filtered phase from each channel was deconvolved - muting only the DC field component - and eroded by the radius of the spherical kernel, leaving reliable phase estimates strictly over a reduced portion of the full ROI. These local phase estimates were subtracted from the unwrapped images to provide estimates of the background over the reduced brain volume. Eroded voxels (*edge points*, EP) were paired with their nearest *internal point* (IP) neighbours within the reduced ROI for which 1st and 2nd order spatial derivatives of the phase could be estimated via finite differences. Using these derivatives and the IP-to-EP distances, the background phase estimate was extended to the whole ROI via a 2nd order 3-dimensional Taylor expansion (Equation 2: $\boldsymbol{\varphi^{IP}}$ denotes the background phase of an EP voxel; $\boldsymbol{d}$ represents the EP-to-IP distance vector ($\boldsymbol{d^T} = [\boldsymbol{d_x}\ \boldsymbol{d_y}\ \boldsymbol{d_z}]$); $\boldsymbol{G}$ is the three dimensional gradient operator and $\underline{\boldsymbol{H}}(\varphi^{IP})$ the 3-by-3 Hessian with entries consisting of the 2nd order partial derivatives evaluated at an IP voxel). Post-expansion background images were subtracted from the unwrapped images and regularized in the conventional SHARP way to yield channel-specific local phase estimates over the extended ROI.

To address the persistence noise and outliers in the image, as well as potential truncation effects of the series expansion, we introduce to the cost function a penalty term arising from the assumption that the local field is Cauchy (i.e. Lorentz) distributed . This new cost function (J_{TC}, subscript for "Taylor-Cauchy") appears in Equation 3, where φ_{o} is the central peak location; σ is the half-width at half-max of the central peak; n is the lexicographic voxel index and $\widetilde{\Delta \varphi}_{\text{local}}$ is the perturbed data ($\tilde{\varphi}_{\text{local}} + \varphi_{\text{o}}$). Distribution parameters were estimated based on the SHARP SoS image. Weighting matrix $\boldsymbol{W_{TC}}$ was formed by assigning Cauchy-derived probabilities to the EP voxels in addition to the channel magnitude weights applied across all voxels. Regularization parameter λ was chosen empirically as ($5x10^{-2}$) and φ_{local} was solved using an iteratively weighted least-squares algorithm [8] in tandem with conjugate gradients.

Figure 1

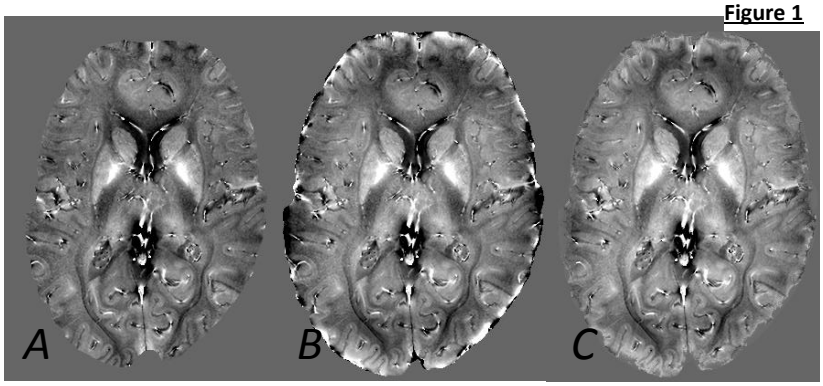

Results: Figire 1 demonstrates the results: (A) is the conventional SHARP SoS-combined image, (B) is the Taylor-recovered phase after combining receive channels using magnitude weights alone (i.e. solving Equation 1); (C) is the Taylor-extended phase incorporating the Cauchy prior.

Conclusion: Appending an extrapolation stage to SMV filtering admits recovery of voxels otherwise lost using the SHARP method while incorporating additional model constraints enables a treatment of outliers and uncertainty in fields map.

References: [1] F. Schweser. *NeuroImage*, vol. 54, pp. 2789–807, 2011. [2] T. Liu. *NMR in Biomed*, vol. 24, pp. 1129–36, 2011. [3] R. Topfer. ISMRM 2013, pp. 3856. [4] H. Sun. ISMRM 2013, pp. 169. [5] S. M. Smith, *Human Brain Mapping*, vol. 17, pp. 143–55, 2002. [6] M. Jenkinson, *Mag Res Med*, vol. 49, pp. 193–7, 2003. [7] L. Li. *JMRI*, vol. 148, pp. 442–8, 2001. [8] M. Sacchi *Geophys J. Int.*, vol. 129, pp. 651-656, 1997.

Susceptibility Mapping of the Sinuses and bones in the Head using Short TE

Sagar Buch[1], Saifeng Liu[1], Yu-Chung Norman Cheng[2], Jaladhar Neelavalli[2], E. Mark Haacke[1,2]
[1]*School of Biomedical Engineering, McMaster University, Hamilton, ON, Canada,*
[2]*Academic Radiology, Wayne State University, Detroit, MI, United States*

Introduction: Usually the focus of susceptibility mapping is the tissues inside the brain, and every effort is made to reduce background field induced by the air-tissue interfaces, usually with the skull region removed [1, 2]. However, in this work, we focus on what is usually thrown away, the sinuses. Using both simulated [2] and real data, we show that one can image these susceptibility objects when there is no signal from them (such as air in sinuses, teeth, bones, etc). Besides, because the susceptibility effects between air and tissue are so large, we are able to use short echo times to extract the susceptibility.

Method: Two MRI datasets were acquired using 3D SWI sequence with imaging parameters: TE=8.25msec (first scan) and TE=5.68msec (second scan), TR=20ms, FA=15°, B_0=3T (Siemens Verio) and resolution=0.5×0.5×2mm^3. The data were acquired sagittally. The 5.68ms data were complex divided into the 8.25ms data to produce phase with effective TE of 2.6ms, which had minimal phase aliasing. Remnant phase wraps were detected by thresholding and removed by adding ±2π. Susceptibility maps (χ(r)) were generated from the resultant phase images (φ(r)) using truncated k-space division with regularization threshold 0.2 as: $\chi(r)=\{FT^{-1}[g^{-1}(k)\cdot\varphi(k)]\}/(\gamma\cdot B_0\cdot TE)$, where $g^{-1}(k)$ represents the inverse of the Green's function $g(k)= 1/3-k_z^2/k^2$, B_0=3T using TE=2.6ms [1]. In order to test our hypothesis, phase images were simulated for a 3D brain model, which includes the basal ganglia, midbrain structures, major veins, grey/white matter, cerebro-spinal fluid and air-tissue interfaces at the brain sinuses with $\Delta\chi_{air\text{-}tissue}$=9ppm [3]. In order to demonstrate the value of preserving the phase information of the tissue outside the brain, we produced simulated SMs with and without applying the brain mask. To reduce streaking artifacts, a k-space iterative algorithm [4] (three iterations) was used in the reconstruction of the susceptibility maps (SM).

Results: The simulated phase of the brain model (Fig. 1a) and the SM in Fig. 1c show the sinuses clearly, whereas Fig 1b shows poor delineation of the sinuses if the phase information outside the brain is not fully preserved. The complex division result shows considerably less phase wraps around the air-tissue interfaces, allowing us to preserve the phase information even outside the brain (pericranium to scalp) (Fig. 1d). In Figs. 1e and 1f, the bone region shows negative susceptibility while the susceptibility values of the sinuses are much higher than other areas of the brain as we expected. The maps of brain sinuses can then be generated from SMs by simple thresholding.

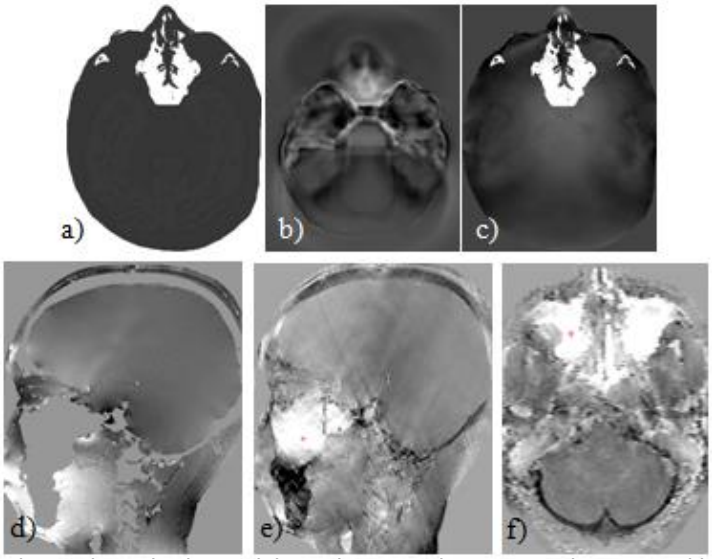

Fig 1: a) 3D brain model used to test the proposed concept, b) Measured SM resulting from the phase simulation after keeping phase only inside the brain, c) Measured SM resulting from the phase simulation after preserving the phase information inside the head (except for the sinuses) d) The resultant phase (TE=2.6ms) after complex division of TE=5.68ms and TE=8.25 phase data sets. e) and f) SMs generated by preserving the phase inside the head for the real data in e) sagittal and f) axial plane.

Discussions and Conclusions: The relevant local information about the brain is buried under the dominant phase effects caused by the high susceptibility difference at the air-tissue interfaces necessitating the application of filtering techniques like homodyne HPF or SHARP [5], which can alter the actual phase information. The sinus maps demonstrated in this abstract can be used to reduce this unwanted phase by generating the phase behavior using a forward calculation for any desired echo time. In order to extract the sinuses more accurately, the SM can be combined with the magnitude images to keep only those points that are clearly air and not tissue. Although higher resolution (0.5mm isotropic) will possess lower SNR, it will provide us with better phase information (with less partial volume effects) around the sinuses. We also use two in-phase images of 5.68ms and 8.25ms to ensure that the fat in the skull shows the correct phase behavior and is not contaminated by water/fat phase shifts. The two key points that make this extraction of sinuses possible are the short effective echo time and the inclusion of the phase information of the tissues outside the brain which provides the necessary missing information to reconstruct the 3D shape of the sinuses. Another important structure on the edge of the brain, the superior sagittal sinus which is usually the region of interest for oxygen saturation studies, could be better reconstructed in SMs if the phase outside the SSS on the skull region was preserved. Eventually, this method could be used to image teeth, bone (making imaging the spine more interesting for SM), and other structures with variable susceptibility that are generally viewed as a problem; now these structures can be viewed as an important source of information.

References: [1] Haacke et al., JMRI(2010);32:663–676. [2] Neelavalli, J. et al. JMRI (2009) 29:937-948. [3] Buch et al., ISMRM(2012):4462. [4] Tang et al. Magn Reson Med (2012). [5] Schweser, F. et al. NeuroImage 54 (2011) 2789–2807.

Noise Effects In Bayesian Quantitative Susceptibility Mapping Methods

Shuai Wang[1], Tian Liu[2], Weiwei Chen[3], Cynthia Wisnieff[2], Pascal Spincemaille[2], A.John Tsiouris[2], and Yi Wang[2]

[1] *University of Electronic Science & Technology of China*, [2] *Cornell University*, [3] *Huazhong University of Science & Technology*

Background/Purpose:

Quantitative susceptibility Mapping (QSM) has generated a lot of scientific interests[1,2]. Many clinically acceptable single orientation QSM methods have been proposed to solve the ill-posed problem to obtain the susceptibility map [3-10]. The forward problem is that the tissue local magnetic field is the convolution of the dipole kernel with the susceptibility distribution in image **r**-space ¢b =*d*⊗¡+*n* [Eq.1], (=¢b=¢b(**r**) is the local field relative to main field B_0, *d*(**r**) the dipole kernel,=¡(**r**) susceptibility distribution, *n*(**r**) noise) or multiplication in **k**-space as [7], ab = *D* ` +*N* [Eq.2] (=ab(**k**) = *F*¢b ,*F* is Fourier transform, *D*(**k**)=*Fd*, ` (**k**)=*F*¡, *N*(**k**)=*Fn)*. We propose to categorize various **Bayesian approach** inverse solutions for QSM into the following two categories**: I) using a general mathematical prior:** ¡=*argmin*{*E*+~*M*} [Eq.3] (*E* is the data fidelity term specifying the likelihood and *M* a general mathematical regularization term). Examples of *M* include the gradient L2 [8], gradient L1 [8,9], total variation norm, wavelet L1[5] and combination of two L1[5]. **II) using specific physical structure prior:** ¡=*argmin*{*E*+~*P*} [Eq.4] (*P* is a prior specific to a physical situation). Examples of *P* is a structural consistency between magnitude and susceptibility *P*=||*mG*¡||1 [Eq.5] [3,10].

Noise is the major cause of error for the QSM inverse solutions. The noise in the magnetic field data has a complex distribution and only when SNR>>1 can be approximated as Gaussian to render a simple weighting factor (w^2=SNR(**r**)^2, referred to as noise whitening) for noise effects in the field based data fidelity expression. In general, the data fidelity can be formulated (nonlinearly w.r.t. field) using complex MR data with Gaussian noise in real and imaginary parts[10].

Methods:

TVWA (Eq.3, *E*=||*z*||$_2^2$, *z*= *d*⊗¡−¢b and ~*M*=~||c¡||1+ TV(¡) [Eq.6][5]) and MGL1 (Eq.4, *E*=||*z*||$_2^2$ and Eq.5) were selected as the representatives of category I and II respectively. The noise whitening was illustrated with NTVWA (Eq.3, *E*=||*wz*$_n$||$_2^2$, *z*$_n$=exp(-*id*⊗¡)−exp(−*i*¢b) and Eq.6) and NMEDI (Eq.4, *E*=||*wz*$_n$||$_2^2$ and Eq.5). Exhaustive parameter search for optimal recon was used for all QSMs. **1) A Zubal numerical phantom** with an additional lesion was constructed with known susceptibility. The Gaussian noise and the noiseless field perturbation are both simulated in complex and use Eq.2 at B_0=3T and TE=20ms. The lesion magnitude, noise level and background were set to the average value of five *in-vivo* images of same imaging parameters. **2) Consecutive patients (n=50)** (with IRB approval) were used to evaluate the noise whitening effects in category I & II. Multi Echo 3D gradient data were acquired with TE1/ΔTE/TR= 5.7/6.7/57ms, number of TE=8; 20° flip, 41.67Hz bandwidth, 24cm FOV, and resolution = 0.57x0.75x2 - 0.7x0.7x0.7mm^3. A neuroradiologist (10 yrs' experience) reviewed all images blinded to reconstruction methods. Image quality was scored (1=corrupted by artifacts; 2=extensive artifacts; 3=substantial artifacts interfering perception; 4=minor artifacts not interfering perception; 5=free of artifacts). Wilcoxon test was used to assess statistical significance.

Results:

There were substantial streaking artifacts in all recons from noisy data compared to noiseless data. The root mean square error (RMSE) in lesion relative to true susceptibility was 135.56%, 9.82%, 110.82%, 2.06% for TVWA, NTVWA, MGL1, and NMEDI respectively. The overall QSM image scores for TVWA, NTVWA, MGL1, and NMEDI were 2.24±0.62, 3.54±0.64, 3.34±0.85, and 4.02±0.65 respectively. The overall image qualities were statistical different between with and without noise whitening ($p<0.02$).

Conclusion:

The noise causes server artifacts in QSM inverse solution. Bayesian approach allows noise whitening to reduce artifacts. Gaussian noise in the complex MR signal domain can be accounted for in the data fidelity term of a QSM methods formulated in the Bayesian approach. The general mathematical prior may be improved with a prior specific to the imaging physical situation. For the illustrated QSM method, NMEDI using the Bayesian approach with a physical structural consistency prior provides the best QSM image quality.

References:

1.Liu T, et al, MRM 2009;61:196. **2.**Schweser F, et al, Neuroimage 2011;54:2789-2807. **3.**Liu J,et al, Neuroimage. 2012.59:2560. **4.**Li W,et al, Neuroimage 2011;55:1645. **5.**Wu B, et al,MRM 2012;67:137. **6.** Shmueli K, et al, MRM 2009;62:1510. **7.** Salomir R, et al, ConceptMR 2003;19B:26. **8**.Kressler B,et al, IEE TMI 2010;29:273. **9**.De Rochefort L, et al, MRM 2010;63:194. **10**.Liu T, et al, MRM 2012, doi: 10.1002/mrm.24272.

Gd-Enhanced Susceptibility Contrast and Anisotropy in the Three-pool Model of White Matter

Russell Dibb[1,2], Wei Li[3], Gary Cofer[1], and Chunlei Liu[3,4]

[1]*Center for In Vivo Microscopy, Duke University Medical Center, Durham, NC, United States,* [2]*Biomedical Engineering, Duke University, Durham, NC, United States,* [3]*Brain Imaging & Analysis Center, Duke University Medical Center, Durham, NC, United States,* [4]*Radiology, Duke University Medical Center, Durham, NC, United States*

Purpose: Quantitative susceptibility mapping (QSM) is a valuable tool in magnetic resonance (MR) histology and is capable of visualizing myelin loss in central nervous system[1]. QSM is greatly improved by using contrast agents at high field. Characterizing the influence of contrast agents and field strength will aid in the effective use, comparability, and consistency of QSM to quantify myelination using MR histology. Compartmental uptake of these contrast agents may further allow us to probe the microstructure of white matter (WM).

Methods: Six C57BL/6 mice were perfused[2] first with a mixture of 0.9% saline and one of six different concentrations of ProHance (Bracco Diagnostics, Princeton, NJ), and then formalin-fixed with 10% buffered formalin (Buffered Formalde-Fresh; Fisher Scientific). Skulls were removed from the body with the brain intact. Data for each brain specimen were acquired using a multi-gradient-echo sequence (TE_1/TE_{10} = 5.0/31.1ms, TR/FA/BW = 500ms/90°/62.5kHz, 86μm isotropic resolution) at field strengths of 2, 7, and 9.4 T. Four excitations were acquired at 2T to achieve adequate SNR. R_2* maps were calculated for each data set using the multi-echo signal information. The signal phase data underwent unwrapping, background phase removal[3], and a deconvolution operation[4] to invert the frequency map and calculate the magnetic susceptibility distribution. The susceptibility maps were then normalized by the applied field. Since frequency offsets and magnetic susceptibility are referenced to the carrier frequency of the RF excitation pulses, the adjacent cortical gray matter was used as an internal reference to allow for useful comparisons to be made between datasets. Volume of interest (VOI) labels from the Waxholm Space (WHS) mouse brain atlas[5] were linearly registered to each data set, and then manually corrected using magnitude images and susceptibility maps. The labels were then registered to the image volumes to prevent interpolation of the original data from each specimen. A previously acquired WM fiber orientation map from a normal, male, C57BL/6 mouse was likewise registered to each individual data set. The fiber angle maps were divided into 18 bins, each having roughly the same fiber angle with respect to the B_0. Mean susceptibility values were then calculated from the WM voxels in each fiber angle map bin. Using a wide range of literature-based values for microstructural properties, a model was constructed to characterize the orientation-dependent contrast at various concentrations of Gd. The model data are not meant to represent a best-fit analytical solution as was developed in a different study that examined orientation-dependent frequency mapping[6].

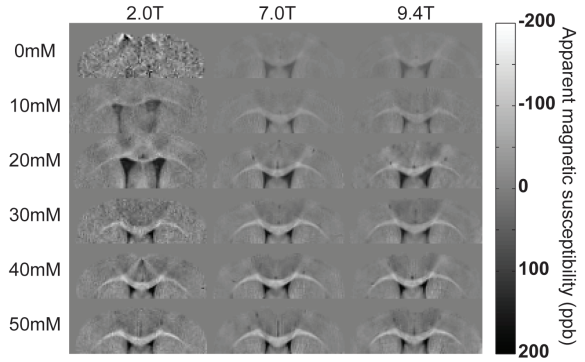

Fig. 1 Field-normalized susceptibility maps show the corpus callosum of mouse brain specimens perfused with six concentrations of Gd and scanned at three field strengths.

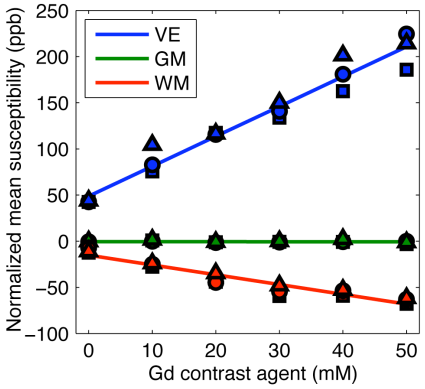

Fig. 2 Dependence of field-normalized susceptibility on Gd concentration at 2T (squares), 7T (circles) and 9.4T (triangles). The regions depicted are corpus callosum white matter (WM), ventricles (VE), and cortical gray matter reference (GM).

Results and Discussion: Field-normalized susceptibility maps in Fig. 1 show the corpus callosum from six Gd-perfused specimens scanned at each field strength. For each dataset, Fig. 2 charts the mean susceptibility of the VOIs representing the corpus callosum white matter (WM), ventricles (VE), and cortical gray matter reference (GM). Two other WM regions and one other GM region (not shown) were also analyzed and produced similar results. Higher magnetic fields yield similar susceptibility contrast and confirm that the susceptibility-field relationship is linear. The susceptibility-Gd relationship, on the other hand, is more complex. Increasing the concentration of Gd enhances WM-GM contrast substantially. The apparent susceptibility of GM remains unchanged at approximately zero ppb (Fig. 2) due to the carrier frequency of the RF fluctuating to match the resonance frequency of the specimen. All WM regions in this study, however, appear relatively more diamagnetic as the concentration of Gd increases since the rate of *absolute* susceptibility increase is smaller in WM than GM. At first glance, this enhancement appears to be approximately linear. However, this is merely a conglomerate result of averaging the underlying nonlinear contrast mechanisms built into the complex WM tissue structure. The three-pool model of white matter suggests that signal contributions arise from multiple, distinct water pools: a myelin pool, an extracellular "mixed" pool, and an intracellular axon pool[7]. The myelin sheath restricts Gd diffusion into the axon; thus, paramagnetic Gd is located primarily in the WM extracellular pool. The signal contribution of this pool is then diminished due to intensified R2* decay. By comparison, the GM reference is relatively more paramagnetic as Gd is able to disperse more homogeneously throughout the tissue. This reasoning concerning the source of WM-GM contrast is only the tip of the iceberg, and further work is required to examine the time-dependent nature of susceptibility contrast due to WM water pools with differing relaxation rates. Furthermore, susceptibility contrast is heavily influenced by WM fiber orientation. Fig. 3A plots the apparent mean susceptibility of WM in the hippocampal commissure (HC) at 7T. The five orientations shown are denoted in Fig. 3B, which is a histogram of the fraction of voxels that make up each angle map bin. Some data points are absent due to a lack of fibers that were nearly parallel to B_0 (deep blue). The model is most accurate for well-represented fiber orientations within the data, such as the nearly perpendicular axon fibers within the HC (orange/red). Both the model and the actual data show perpendicular fibers as being more diamagnetic than parallel fibers, which is likely due to the magnetic anisotropy of the myelin lipid bilayer[8]. At high concentrations of Gd, this anisotropy is nonlinearly enhanced 3-4 fold. These findings suggest that combining contrast agents with QSM will aid in probing the microstructure of WM axons.

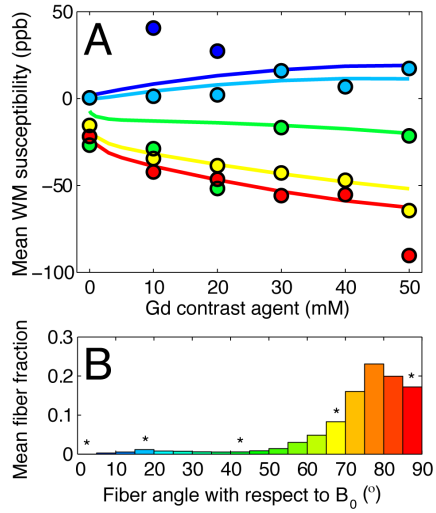

Fig. 3 A: Dependence of model (lines) and actual (circles) WM susceptibility data on fiber orientation and Gd concentration at 7T. B: Fraction of hippocampal commissure WM voxels in each angle bin. The asterisks denote which data are shown in plot A.

Conclusion: Field-normalized magnetic susceptibility maps of the adult mouse brain verify that the susceptibility-field strength relationship is linear. Gd greatly improves WM-GM susceptibility contrast, and the complex structure and orientation of WM introduce non-linear effects to this enhancement. Additional work is under way to characterize the time- and orientation-dependent effects of WM structure on magnetic susceptibility contrast and will further augment the utility of QSM in MR histology.

References: [1] Liu C, et al. *NeuroImage*. 2011; 56(3):930-8. [2] Johnson GA, et al. *Radiology*. 2002; 222(3):789-793 [3] Schweser F, et al. *NeuroImage*. 2010; 54(4):2789-807. [4] Li W, et al. *NeuroImage*. 2011; 55(4):1645-56. [5] Johnson GA, et al. *NeuroImage*. 2010; 53(2):365-372. [6] Wharton S and Bowtell R. *Proc Natl Acad Sci USA*. 2012; 109(45):18559-64. [7] Lancaster JL, et al. *J Magn Reson Imaging*. 2003; 17(1):1-10. [8] Li W, et al. *NeuroImage*. 2012; 59(3): 2088-97.

Acknowledgements: All work performed at the Duke Center for *In Vivo* Microscopy and funded by NIBIB P41 EB015897 and NIBIB T32 EB001040.

Towards in vivo manganese quantification at 14.1T using Susceptibility Mapping

Rajika Maddage[1], Jose P. Marques[1,2], Diana Khabipova[1] and Rolf Gruetter[1,2]
[1]Laboratory for Functional and Metabolic Imaging, Ecole Polytechnique Fédérale de Lausanne, Lausanne,
[2]Department of Radiology, Universities of Lausanne and Geneva, Lausanne and Geneva,

Introduction: Manganese Enhanced MRI (MEMRI) has been increasingly used in animal neuroimaging thanks to manganese T_1 shortening property and analogy to calcium [1]. Recently it was shown that at higher magnetic field strength, MEMRI can be also exploited by using manganese's susceptibility induced frequency shift [2]. By considering manganese as a simple isotropic susceptibility contrast agent, quantitative susceptibility maps (QSM) would offer the opportunity to obtain quantitative manganese uptake maps at high resolution.

The present work investigates *in-vivo* the level of phase contrast and quantitative susceptibility mapping enhancement as a function of manganese dose at 14.1T in the rodent brain.

Methods: Scans were performed on a 14.1T/26 cm scanner (Varian/Magnex Scientific) using a home built quadrature surface coil as RF transceiver. Phase images and corresponding QSM were obtained using a 3D Gradient Echo sequence with a respiration triggering scheme to reduce respiration induced artefacts: TR=27ms (32 phase encoding steps acquired per respiration cycle), TE=16ms, resolution=78*78*78μm^3, acquisition time ≈8 hours. Phase images were unwrapped and background field contributions originating from imperfect shimming and air tissue interfaces were filtered using the SHARP algorithm [3]. Gradient echo data were co-registered using FLIRT [4]. QSM were computed using an l2 regularized single orientation method [5]. As previous results based on T_1 mapping before and after manganese infusion have shown that no enrichment is expected in white matter tracts [2], the corpus callosum was used as reference ($\chi = 0$).

Experiments were carried out on four adult rats weighting 225-250g. Manganese solution (120mM) was infused via the tail vein (1.0mL/h) under 2% isoflurane anesthesia. Each rat received the following dose (n=1): 0, 40, 75, 125mg/kg. MRI scans were performed 24h post Mn^{2+} systemic administration under 2% isoflurane anesthesia and animal temperature maintained at 37.5°C±0.5.

Results and discussion: In vivo phase images were of excellent quality and showed high contrast in both axial and coronal planes (figure. 1a and 1b respectively). 24h post manganese infusion, enhancement of the hippocampus from the lowest dose of 40mg/kg was already visible in both phase and QSM with clear delineation of the dentate gyrus (DG) (white arrows in figure. 1a). Such enhancement with increased SNR and CNR progressed with increasing doses of Mn^{2+} (figure.1) thanks to the T_1 shortening. Regions in which Manganese deposition has been demonstrated in the past using T_1 mapping (regions rich in granule cells such as the granule cell layer of the hippocampus, the olfactory bulb and the cerebellum), appear bright in the quantitative susceptibility maps demonstrating their increased paramagnetism after enrichment.

Future work will focus on comparing the enrichment measured using quantitative susceptibility maps and that estimated from T_1 mapping.

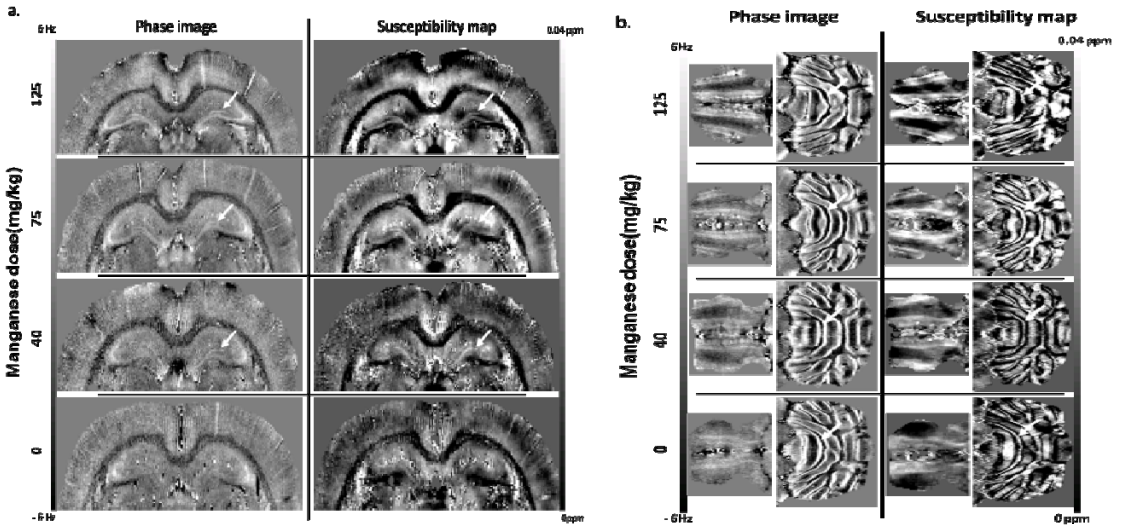

Figure 1 : In vivo phase image and corresponding magnetic susceptibility map of the cortex and hippocampus in axial plane (a.) and olfactory bulb, cerebellum in coronal plane (b.) at different manganese doses, 24h post manganese infusion. White arrows point out to the dentate gyrus and the granule layer of the cerebellum.

References: [1] Tucciarone, NeuroImage 2009; [2] Maddage, ISMRM, 2010; [3] Schweser, Neuroimage 2011; [4] Jenkinson, Neuroimage 2002; [5] de Rochefort, MRM 2010. Supported by CIBM of the UNIL, UNIGE, HUG, CHUV, EPFL and the Leenaards and Jeantet Foundations.

Precision Limit of Contrast Agent with R_2^* (Magnitude) and Quantitative Susceptibility Mapping (Phase)

Hongchen Wang[1], Xavier Maître[1], Luc Darrasse[1], and Ludovic de Rochefort[1]

[1]*Imagerie par Résonance Magnétique Médicale et Multi-Modalités (UMR8081) IR4M, CNRS, Univ Paris-Sud, Orsay, France*

Background/Purpose: Apparent transverse relaxation rate R_2^* and magnetic susceptibility χ [1-2] are distinct measurable parameters that can be used to quantify paramagnetic and superparamagnetic contrast agents. R_2^* mapping requires several echo times in a gradient-echo scan and is based on the analysis of signal amplitude decrease. Quantitative Susceptibility Mapping (QSM) [3-4] uses magnetic field mapping, which can be extracted from the phase data of an identical multi-echo dataset. Here, phantom experiments and simulation are performed to compare the precision of contrast agent concentration with R_2^* and susceptibility methods.

Methods: Phantoms with two types of contrast agents (CAs) were realized, Gd-DOTA (Dotarem; Guerbet, France) and superparamagnetic iron oxide nanoparticles (SPIO) (Endorem; Guerbet, France), used in particular for their transverse relaxation effects. Twelve centimeter long, 13 mm diameter cylindrical tubes were filled with solutions of various CA concentrations and were immersed in a cylindrical container filled with water. Gd concentrations ranged from 2.5 mM to 20 mM and SPIO from 25 µM to 200 µM. Experiments were conducted at 1.5T (Achieva, Philips, The Netherlands). The tubes were placed aligned with the main magnetic field in an 8-channel head coil. A multi-echo gradient-echo sequence with the following parameters was applied: $TR/TE_1/\Delta TE$ = 641/1.79/2.45 ms, 15º flip angle, 32 echoes, FOV = 192 mm, 1.5 mm in plane resolution, 5 mm thick slices and a 1.3 kHz bandwidth-per-pixel. These parameters provided proton-density contrast for the first echo so that subsequent processing had no influence from longitudinal relaxation. T_2^* reconstruction was performed using a nonlinear least squares method; and frequency shifts (in Hz) were reconstructed using a weighted linear least squares method of phase over echoes [3]. Magnetic susceptibility was assumed to be 3 times the normalized frequency shifts, as it should be for a cylinder aligned with B_0. Regions-of-interest were drawn over the tubes to determine mean and standard deviations (SD) of R_2^* and frequency effects. SD were converted into concentration error and compared. Additionally, to compare experimental errors with theory, the R_2^* and phase fitting procedures were applied to an exponential decay simulating T_2^* relaxation. Gaussian noise added to real and imaginary parts with same variance as in the experiment so that to get SNR=25 for the first echo. Procedure was repeated 1024 times and simulated R_2^* and phase SD were obtained.

Results: A molar relaxivity r_2^* = 5.2 $s^{-1}mM^{-1}$ and a molar susceptibility χ_m = 363 $ppm.M^{-1}$ (~ an effect on frequency of 7.7 $Hz.mM^{-1}$) were measured for Gd (Fig.1). The slopes were comparable with slightly lower amplitude than phase effects. A molar relaxivity r_2^* = 202.3 $s^{-1}mM^{-1}$ and a molar susceptibility χ_m = 3216 $ppm.M^{-1}$ (~ a molar effect on frequency of 68.4 $Hz.mM^{-1}$) were measured for SPIO (Fig.2). Amplitude effects were higher than phase effects for SPIO. When converted to concentration using these calibration slopes, SD increased with concentration both for amplitude-derived and phase-derived methods (Fig.1d and 2d). Qualitatively on images amplitude-derived concentration are noisier than phase-derived concentration. While amplitude-derived precision varied from 0.1 to 1.4 mM for Gd, and from 2.7 to 15 µM for SPIO, phase-derived concentration varied from 0.02 to 0.5 mM for Gd, and from 1.5 to 7 µM for SPIO. Regardless on the CAs used, phase-based concentration measurement was between 2.4 and 6 times more precise for Gd, and between 1.5 and 4.2 times for SPIO. From these data, precision limit for this setup was estimated to be 18 µM and 1.5 µM for phase-derived concentration for Gd and SPIO, respectively. While measured and theoretical SD agreed for Gd experiments (Fig.1d), measured SD for SPIO were not completely explained by the theory (Fig.2d), although the trend for more precise concentration measurement using phase was also observed.

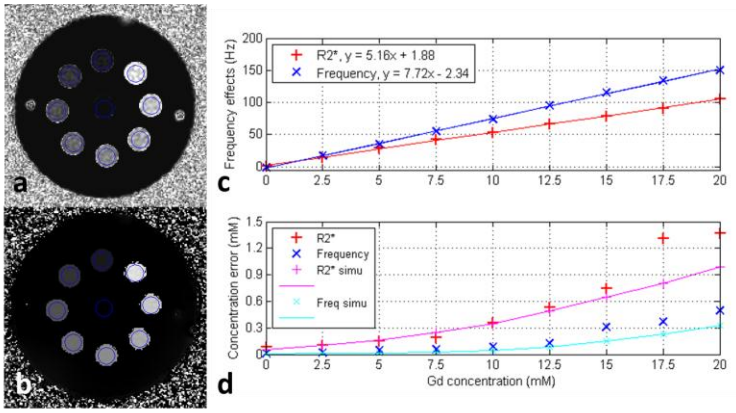

Fig.1: Amplitude-derived (a) and phase-derived (b) concentration maps for Gd phantom. Measured R_2^* and frequency shift (c) both linearly increase with concentration. Their associated concentration SD (d: points) also show an increase with concentration. Amplitude and phase-based contrast had similar frequency effects. Phase-based quantification had a smaller error. Simulated concentration SD (d: solid lines) had the same tendency.

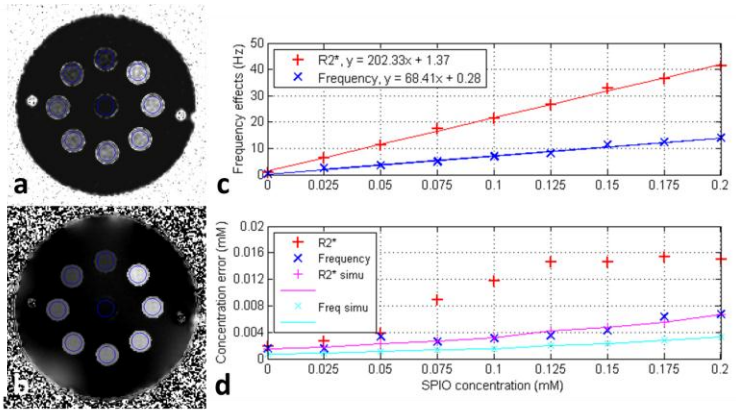

Fig.2: Amplitude-derived (a) and phase-derived (b) concentration maps for SPIO phantom. Measured R_2^* and frequency shift (c) both linearly increase with concentration. Their associated concentration SD (d: points) also show an increase with concentration. Phase-based contrast showed a smaller frequency effect and smaller SD. Simulation (d: solid lines) had the same tendency, but smaller values.

Conclusion: We have experimentally shown on a clinical system with standard imaging parameters and setup that, in the ideal case of cylinders oriented along the main field, phase-derived concentration (susceptibility phase shifts) was between 1.5 and 6 times more precise than amplitude-based quantification (susceptibility phase dispersion). The precision difference between simulation and measurement for SPIO would require analyzing potential other sources of noise. These results suggest that QSM reconstruction may be more precise than R_2^* mapping to detect and quantify paramagnetic and superparamagnetic CAs. However, additional studies would be required to estimate the effective QSM precision, in particular the noise propagation considering shape factors [2]. A combination of phase and magnitude in multi-echo gradient-echo scans would ideally yield enhanced quantification and detection for molecular MRI involving paramagnetic and superparamagnetic CAs.

References: 1. Haacke, MRI, Wiley-Liss, 1999. **2.** de Rochefort *et al.*, Med Phys 2008. **3.** de Rochefort *et al.*, MRM 2010. **4.** Shmueli *et al.*, MRM 2009.

On the influence of particle size in MR iron quantification

Jan Sedlacik[1], Jürgen R. Reichenbach[2], Ferdiand Schweser[2]

[1]Department of Neuroradiology, University Medical Center Hamburg-Eppendorf, Hamburg, Germany

[2]**Medical Physics Group, Medical Physics Group, Institute of Diagnostic and Interventional Radiology I, Jena University Hospital-Friedrich Schiller University Jena, Jena, Germany.**

Introduction: Due to diffusion effects, the transverse relaxivity caused by small iron particles depends on the particles' size.[1] In the case of very small particles (<100 nm), the effective relaxivity (r_2*) is similar to the irreversible relaxivity (r_2), and r_2' is small. On the other hand, for large particles (>100 nm), r_2* is similar to the reversible relaxivity (r_2') and r_2 becomes small. Consequently, the same amount of iron can cause very different relaxation rates compromising relaxation-based iron quantification measurements. However, the bulk frequency shift is supposed to be determined by the average magnetic susceptibility of the solution and, therefore, independent of particle size, aggregation or distribution. The purpose of this work was to investigate this theoretical behavior in a phantom experiment and to discuss implications for future *in vivo* studies.

Methods: Two kinds of iron-oxide particles were investigated: Micromod (plain iron-oxide particles, 250 nm in diameter) and Feridex (dextran-coated iron-oxide cores, 5 nm in diameter). The smaller particles mimicked non-aggregated iron stores like freely dissolved ferritin (6 nm diameter)[2]. The larger particles mimicked agglomeration of iron stores in cells, like hemosiderin. The phantom consisted of a spherical bowl filled with 5L saline solution. Four 50 mL Falcon tubes were placed in the bowl's center parallel to the main magnetic field. The tubes were filled with saline and electrostatically and sterically stabilized iron-oxide particle suspensions resulting in homogeneous suspensions with iron concentrations (IC) of 0, 0.33, 0.67 and 1mg/kg. Irreversible (R_2), reversible (R_2') and effective (R_2*) transverse relaxation rates were assessed by analyzing magnitude images (e.g., left-most panel in Fig.1) acquired with a gradient echo sampled spin echo (GESSE) MRI sequence,[3] using 23 echoes with TE=46-134 ms, ΔTE=4 ms and spin echo time=82 ms. The MR frequency shifts caused by the iron particles were determined from background-field corrected GESSE phase images (e.g., right-most panel in Fig.1). Background-field correction was achieved by 7th degree 2D polynomial fitting of the tubes' surrounding.

Results: All MR-based quantities showed highly linear correlation with IC (R^2>0.94, p<0.002). Slopes of R_2, R_2' and R_2* with respect to IC, i.e., relaxivities r_2, r_2' and r_2*, were lower for the small particles (Feridex; Fig.2-left) and higher for the large particles (Micromod; Fig.2-right). In contrast to the relaxivities, linear regression of the frequency shifts revealed very similar slopes for small and large iron oxide particles (Fig.3).

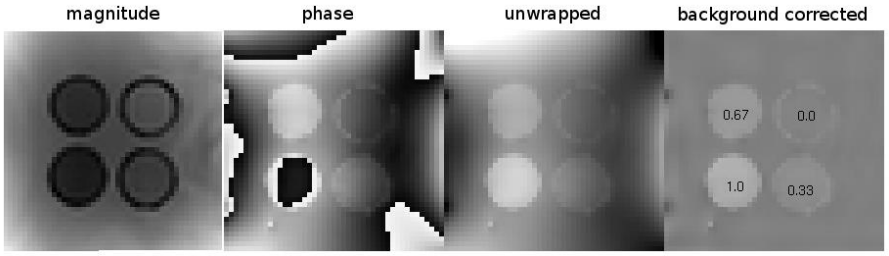

Fig.1: GESSE magnitude (left-most) and phase data (second from left). Phase was unwrapped (second from right) and corrected for background field (right-most). IC of tubes is denoted in mg/kg in right-most image.

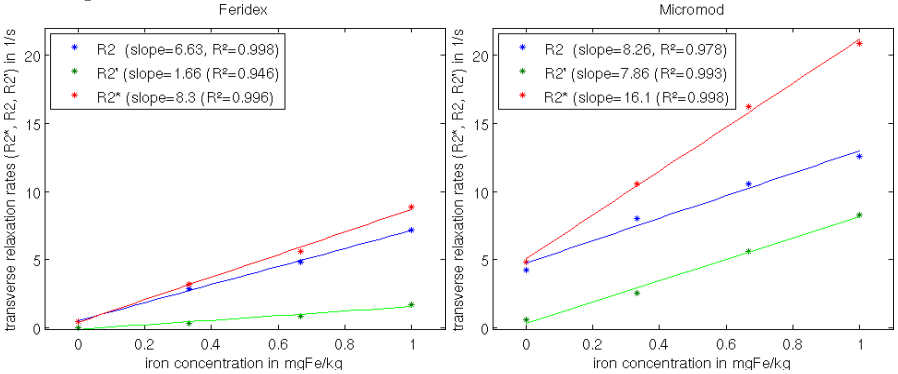

Fig.2: Transverse relaxation rates vs. iron concentration. Linear regression yielded relaxivities (slopes) that were different for the two different sized particles.

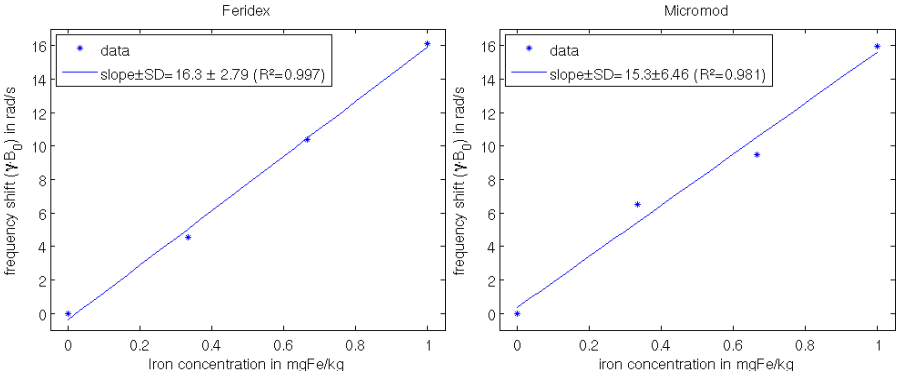

Fig.3: Frequency shift vs. iron concentration. Linear regression yielded equal slopes for both particle sizes.

Discussion: The much higher r_2 compared to r_2' of the small particles implies that in this case the transverse relaxation process is dominated by diffusion. The large particles showed nearly equal r_2 and r_2' relaxivities indicating that transverse relaxation of these particles is less affected by diffusion. The similar slopes of the linear regression of frequency shifts clearly demonstrate the insensitivity of this quantity with respect to particle size. However, the frequency shift is well known to be very sensitive to the shape of samples and their orientation with respect to the main magnetic field. To allow direct comparison between IC and frequency shift, orientation and shape was kept constant in this study. For heterogeneous samples, e.g., *in vivo* measurements, the phase may be converted to the underlying shape-independent magnetic susceptibility distribution using quantitative susceptibility mapping (QSM) techniques.[4]

Conclusion: Results suggest that the use of MR phase data with subsequent QSM yields more robust estimates of the IC than R_2* and R_2. However, R_2* and R_2 may be useful to assess the aggregation and distribution of iron stores in the tissue matrix.

References: [1] Ziener C et al. 2012. Phys Rev E Stat Nonlin Soft Matter Phys. 2012 May;85(5-1):051908. [2] Harrison PM and Arosio P, 1996. *BBA-Bioenergetics*, 1275(3), 161–203. [3] Yablonskiy DA. 1998. *Magn Reson Med.* 39: 417-428. [4] Schweser F et al., 2011. *NeuroImage*, 54(4):2789–2807.

Correlations among R2*, susceptibility, and FA in white matter of the human brain

Guochun Fu[1], Masaki Fukunaga[2] and Tie-Qiang Li[1,3]

[1]*Department of Clinical Science, Intervention and Technology, Karolinska Institute, Sweden,*

[2]*Lab of Functional and Molecular Imaging, National Institute of Neurological Disorders and Stroke, USA*

[3]*Institute of Biomedical Engineering and Instrument Science, Zhejiang University, China,*

Background: High resolution MRI at 7T suggests that T2* contrast may be sensitive to brain composition, microstructure, and fiber orientation [1-3]. Preliminary studies [4,5] based on T2* relaxation rate (R2*=1/ T2*) and diffusion fractional anisotropy (FA) measurements indicate that there might exist correlation between them. However, recent studies based on quantitative susceptibility mapping in combination with microscopic measurements showed that the T2* heterogeneity in white matter is only in part reflect its myelin content [6]. In this study, we further explored the quantitative correlations among R2*, susceptibility, and FA in the brains of normal volunteers by using in vivo diffusion tensor imaging and multi-echo R2* measurements at 3 and 7T.

Methods: The experiments were conducted on whole body GE Signa 3 and 7T MRI systems equipped with Twin-Speed gradient sets. Signal reception at 3 and 7T was performed using 16 and 32-channel whole-brain detector arrays (NOVA Medical Inc, MA), respectively. Whole brain diffusion tensor imaging (DTI) measurements were performed at 3T with 3 repeat measurements. R2* mapping was conducted at both 3 and 7T with at least 2 repeats. The R2* measurements at 7T were also carried out at two different orientation angles (0° and 30°) by tilting the detector. 12 normal volunteers (aged 23-52, 5 females) were studied on both scanners. The FA and R2* mapping at 3T were performed at the same slice location. The 3T protocol included the following: 1) 3 repeated sets of R2* mappings using an EPI style readout to acquire 20 gradient echoes. The acquisition parameters were: 56 transverse slices of 2 mm thick, in-plane resolution of 1x1mm^2, TR=4.1s, TE was varied from 8.4 to 49.4ms; 2). Three sets of DTI measurements based on the single-shot SENSE EPI method. The acquisition parameters were: 56 contiguous axial slices of 2mm thick with locations coinciding with those of the R2* measurements, in-plane resolution of 2x2 mm^2, TR=13s, b=1000s/mm^2, an optimized DTI scheme with 6 T2-weighted and 50 diffusion-weighted scans. The same R2* mapping protocol was also used on the 7T. To facilitate the co-registration between the 3T and 7T MRI data, facial stickers were used when positioning the volunteers into the magnets. Experiments at 3 and 7T lasted 120 and 90 minutes, respectively. The FA and R2* maps were extracted by standard non-linear curve fitting procedures. To mitigate the effect of macroscopic inhomogeneities on R2* mapping, a model based on first-order correction was used [3]. For each R2* mapping data set, the even and odd echoes were evaluated separately. Therefore, the triple measurement protocol produced 6 sets of R2* maps. Motion correction and image co-registration were performed by using the AFNI software packages. The inverse Fourier algorithm [7] was used for QSM.

Results: R2* and FA maps measured at 3T can be precisely co-registered. Since they were measured by at the same slice locations, the extracted parameter maps are of high quality and similar contrast in white matter. As estimated from the repeated measurements, the uncertainties (std/mean)for the R2* measurements at 3 and 7T were about 2 and 3%, respectively. The uncertainty in the measured FA values in white matter was about 4%. scatter plot of R2* versus FA values for ROIs (circular areas of 78 mm^2) randomly selected in brain white matter. Based on the analysis of 160 ROIs per subject, the estimated correlation coefficients between the average R2* and FA were 0.32 and 0.53 for the 3 and 7T data, respectively. The correlation coefficients between the average bulk susceptibility and FA were -0.19 and -0.32 for the 3 and 7T data, respectively. Both R2* and bulk susceptibility showed significant dependence on the fiber orientation. White matter fiber tracts with anterior-posterior direction (perpendicular to B_0) have higher relaxation rates than those with inferior-superior direction (parallel to B_0) and are more diamagnetic.

Conclusion: The correlation coefficient between R2* and FA measured at 7T are much higher than those at 3T, despite the increased scatters apparently associated with the imperfect co-registration between 3T DTI and 7T R2* data. This suggests that at higher magnetic field strength, R2* and QSM become more sensitive measures of FA. The significant correlation between R2* and FA suggests that high field QSM may be used as an alternative to DTI for the discrimination of fiber bundles based on their myelination, which can be readily performed at higher resolution. However, R2* and susceptibility anisotropy makes their relationship with FA quite complicated. Even under the assumption of cylindrical symmetry [8], a minimum of 2 independent measurements with different head rotations are necessary to derive orientation independent parameters.

References: [1] T. Q. Li et al. *Magn Reson Med*, **62**:1652 (2009); [2] M. Fukunaga et al. *Proc Natl Acad Sci USA.* . **107**:3834 (2010);[3 P. Sati et al. *NeuroImage* 59 979 (2012)**;** [4] T. Q. Li et al. *Proc. Intl. Soc. Mag. Reson. Med* 17 (2009)**;** [5] A. Cherubini et al. *Magn Reson Med* **61**: 1066 (2009)**;** [6] C. Liu et al. *Neuroimage* **56**, 930 (2011)**;** [7] K. Shmueli, et al. *Magn Reson Med*, **62**:1510:22 (2009). [8] X. Li et al, *NeuroImage* **62** 314 (2012).

Structural Disordering as a Mechanism of Phase Contrast in Multiple Sclerosis Lesions

Dmitriy A Yablonskiy, Jie Luo, Alexander L Sukstanskii, and Anne H Cross

Washington University, St. Louis, MO, USA

Background/Purpose: Phase images obtained by gradient echo (GE) MRI provide image contrast distinct from T1 weighted (T1W) and T2 weighted (T2W) images. One of the emerging applications in phase imaging is studying multiple sclerosis (MS) e.g. [1-3]. Herein we provide theoretical explanation of the phase contrast in MS lesions based on the mechanism that relates MRI signal phase not only to tissue magnetic susceptibility but to tissue microarchitechture at the cellular and sub cellular levels [4].

Theory: Tissue magnetic properties are usually defined in terms of magnetic susceptibility χ that has contributions from magnetic susceptibility inclusions such as proteins, lipids, deoxyhemoglobin, iron, etc. In the presence of external magnetic field, magnetic susceptibility inclusions become magnetized and induce their own magnetic field that shifts Larmor resonance frequencies of neighboring water molecules. This shift Δf is usually described in terms of a Lorentzian sphere: $\Delta f / f_0 = 4/3\pi\chi$, where f_0 is the base Larmor resonance frequency. However, as it was demonstrated in [4], for white matter, where the distribution of induced magnetic fields is mainly determined by magnetic susceptibility of myelin sheath and intra-axonal filaments that run mostly parallel to axonal axis, the Generalized Lorentzian approach rather than Lorentzian sphere approximation should be used to describe susceptibility induced MR signal frequency shift. Herein we demonstrate that this mechanism can explain most of the phase lesions in MS. Figure at left shows our theoretical result derived from computer Monte-Carlo simulations of the effect of increasing axon damage on phase/frequency of MR signal. a) Schematic of an intact axon (internal cylinder) covered by myelin sheath (bold outline of the internal cylinder) in an extra-cellular space between bold and outer cylinder with radius R_0. b) "mildly" damaged axon – fragments of the original myelin sheath are slightly scattered. c) "severely" damaged axon - fragments of the sheath are scattered randomly. Lower panel -- dependence of the Lorentzian Factor (*LF*) in the MR signal frequency shift $\Delta f / f_0 = LF \cdot \chi$ on a "level of distraction" (δR – average fragments' distance from the center).

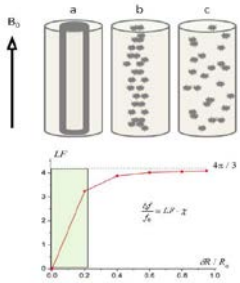

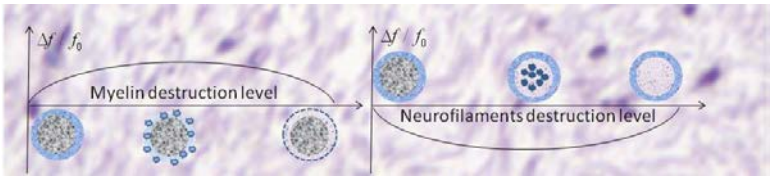

Figure at left represents schematic structure of the MR signal phase/frequency change with MS lesion severity for two types of tissue destruction: left panel – pure myelin injury ($\chi > 0$), right panel – pure injury to neurofilaments ($\chi < 0$). Minimal myelin injury which may not be apparent on standard T2W and T1W images will appear positive by phase, corresponding to the initial ascending portion of the left figure (and also lower panel Fig. 1). For moderately severe lesions with predominant myelin injury (center of the left figure), phase will also be positive. However, axon destruction is often also present, and the relative degree of myelin and neurofilament destruction will affect the sign of the phase change. Severe lesions such as persistent black holes, with a high TDS score and significant destruction of both myelin and axons might disappear on phase images.

Methods: Three RRMS and three SPMS patients were imaged using a Siemens 3T Trio MRI scanner. Three dimensional (3D) version of the GEPCI technique [5] was used to generate frequency and R2* maps along with GEPCI-FLAIR, GEPCI T1f and T1w images [6]. Lesion severity was assessed based on the lesion Tissue Damage Score (TDS) introduced in [5].

Results and Discussion: Typical results are presented in figure below. Upper panel – data obtained from a subject with SPMS. GEPCI-FLAIR image is T2* map with suppressed CSF signal. GEPCI T1f image has superior contrast between GM and WM. Rectangles outline MS lesions. Orange rectangle represents example of MS lesion that is seen only on phase image (bright contrast) and GEPCI T1f image with negative dark contrast. Blue rectangle outlines small MS lesion that is barely seen on FLAIR and GEPCI-FLAIR but is well visible on phase image. Red rectangle outlines severe MS lesion (very high, red, TDS score) that is seen on T1W, FLAIR and GEPCI FLAIR but does not have a footprint on phase image. A magnified view of this lesion is shown in inset upper right of GEPCI T1f image along with overlaid GEPCI TDS score (shown as a color bar). Lower panel - data obtained from a subject with RRMS showing multiple lesions (red rectangles) with intermediate TDS scores (color overlaid on GEPCI T1f image). Here, lesions seen on FLAIR are also seen on GEPCI Phase. Area within orange oval corresponds to partial volume effect from the ventricle in the adjacent slice.

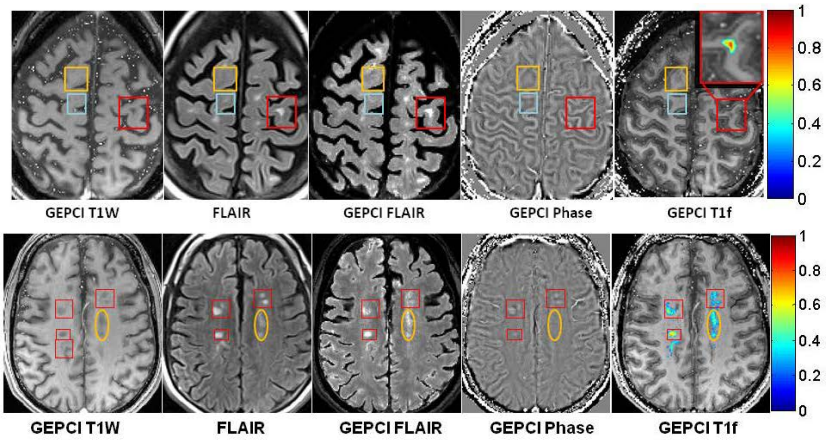

Conclusion: We have proposed theory of phase contrast in MS. Our theory predicts that the phase contrast in MS lesions could appear because of the well-known MS pathology affecting white matter integrity, such as injury to the myelin sheath, even without its removal from the affected area, thus preserving tissue magnetic susceptibility. Contrary to an expectation that the phase contrast in MS lesions should always increase in magnitude with lesion worsening (as happens for all known MR magnitude imaging contrast mechanisms), our theory and results demonstrate that the phase contrast can actually disappear with extreme tissue destruction.

References:

1. Hammond, K.E., et al., Annals of Neurology, 2008. 64(6): p. 707-713. **2**. Haacke, E.M., et al., J Magn Reson Imaging, 2009. 29(3): p. 537-44. **3**. Yablonskiy, D.A., et al., Proc Natl Acad Sci U S A, 2012. 109(35): p. 14212-7. **4**. He, X. and D.A. Yablonskiy, Proc Natl Acad Sci U S A, 2009. 106(32): p. 13558-63. **5**. Sati, P., et al., Neuroimage, 2010. 51(3): p. 1089-97. **6**. Luo, J., et al., Neuroimage, 2012. 60(2): p. 1073-1082.

Origin of B_0 orientation dependent R_2^* (=1/T_2^*) in white matter: the effects of magnetic susceptibility, magic angle, tissue iron and temperature

Se-Hong Oh[1], Young-Bo Kim[2], Zang-Hee Cho[2] and Jongho Lee[1]
[1]Department of Radiology, Perelman School of Medicine, University of Pennsylvania, Philadelphia, PA, USA,
[2]Neuroscience Research Institute, Gachon University, Incheon, Korea

Background/Purpose: Recently, R_2^* in white matter has been shown to change based on the relative angle between B_0 and fibers [1-4] and a model with magnetic susceptibility anisotropy in myelin has been proposed as the origin of the contrast [4]. The angular dependence has been shown to follow $M_{SA}(\theta) = c_{ind} - c_{iso} \cdot \cos 2\theta + c_{ansio} \cdot \cos 4\theta$ (Eq. 1) where the first term is an orientation independent term, the second term is from isotropic susceptibility, and the third term is from anisotropic susceptibility [4]. The origin of the orientation dependence has been suggested as myelin [5,6]. However, other sources of magnetic susceptibility, most notably iron, may have additional contributions to the orientation dependent R_2^*. Additionally, the magic angle effect [7] may be another origin of the orientation dependent R_2^* and can result in the same angular dependency as Eq. 1 when it is combined with isotropic susceptibility: $M_{MI}(\theta) = c_{ind} + c_m \cdot (3\cos^2\theta - 1)^2 - c_{iso} \cdot \cos 2\theta$ (Eq. 2) where the second term is from the magic angle effect. In this study, we performed experiments to estimate the contribution of the magic angle effect and tissue iron to B_0 orientation dependent R_2^*. Furthermore, the effects of temperature on the R_2^* and ΔR_2^* ($= R_{2\parallel}^* - R_{2\perp}^*$) was also studied to understand the contrast difference between in-vivo (38°C) and ex-vivo (21°C).

Methods: ***Magic angle vs. susceptibility anisotropy***: To separate the magic angle effect from the magnetic susceptibility effect, both GRE and SE are acquired in a fixed specimen with corpus callosum (CC). Data were acquired at 12 different orientations (0 to 180°). For R_2 estimation, a 2D SE with a single echo was acquired 7 times with different TEs. For R_2^* estimation, a 3D multi-echo GRE sequence was used. For each angle, the averaged R_2 and R_2^* values were calculated in CC ROIs to generate orientation dependent curves (Fig. 1, red and magenta). These curves were then fitted to a suscept-aniso model (Eq. 1) and a magic-iso model (Eq. 2) to calculate the goodness of fit. In the magic-iso model, the contribution of orientation dependent R_2 from the magic angle effect was expected to stay the same in the R_2^* measurement since R_2^* is sum of R_2 and R_2'. As a result, the regression result of the magic angle regressor obtained from the R_2^* measurement was removed from the R_2 curve of the magic-iso model before calculating the goodness of fit. As a control for white matter, an ROI in basal ganglia (BG) was chosen and tested for the orientation dependent R_2^*. ***Iron extraction***: To estimate the contribution of tissue iron to the orientation contrast, we compared ΔR_2^* before and after iron extraction. Iron was removed from tissue using iron chelating solution [8]. ***Temperature***: To measure the contribution of temperature to R_2^* and ΔR_2^* contrasts, the specimen was scanned at room (21°C) and body (38°C) temperatures. Scanning was performed at two orientations: one with the CC parallel to B_0 ($R_{2\parallel}^*$) and the other perpendicular to B_0 ($R_{2\perp}^*$). Two ROIs (CC and BG) were used for the analysis.

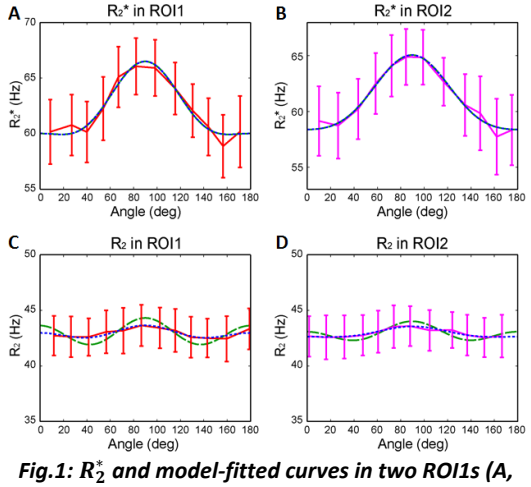

Fig.1: R_2^* and model-fitted curves in two ROI1s (A, B). R_2 and model-fitted curves in two ROIs (C, D). Suscep-aniso: blue-dotted, Magic-iso: green-dashed

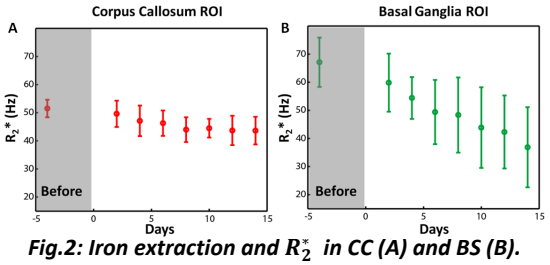

Fig.2: Iron extraction and R_2^* in CC (A) and BS (B).

Iron		Before	After (day 14)	p-value
Corpus Callosum	$R_{2\parallel}^*$	51.3 ± 3.1 Hz	43.6 ± 4.9 Hz	< 0.001
	$R_{2\perp}^*$	47.5 ± 2.7 Hz	39.2 ± 3.5 Hz	< 0.001
	ΔR_2^*	4.0 ± 2.9 Hz	4.5 ± 4.3 Hz	0.151
Basal Ganglia	$R_{2\parallel}^*$	67.1 ± 8.8 Hz	36.9 ± 14.2 Hz	< 0.001
	$R_{2\perp}^*$	66.6 ± 8.3 Hz	36.4 ± 14.2 Hz	< 0.001
	ΔR_2^*	0.5 ± 8.6 Hz	0.5 ± 14.2 Hz	0.992

Table1: Effects of iron on R_2^* and ΔR_2^*

Temperature		21 °C	38 °C	p-value
Corpus Callosum	$R_{2\parallel}^*$	51.5 ± 3.1 Hz	47.5 ± 3.0 Hz	< 0.001
	$R_{2\perp}^*$	47.5 ± 2.7 Hz	41.5 ± 2.1 Hz	< 0.001
	ΔR_2^*	4.0 ± 2.9 Hz	5.9 ± 2.6 Hz	< 0.001
Basal Ganglia	$R_{2\parallel}^*$	67.1 ± 8.8 Hz	58.4 ± 8.9 Hz	< 0.001
	$R_{2\perp}^*$	66.6 ± 8.3 Hz	58.7 ± 7.6 Hz	< 0.001
	ΔR_2^*	0.5 ± 8.6 Hz	-0.3 ± 8.3 Hz	0.101

Table2: Effects of temperature on R_2^* and ΔR_2^*

Results: ***Magic angle vs. susceptibility anisotropy***: The R_2^* curves (Figs. 1A and 1B) clearly demonstrate B_0 orientation dependence. They show much larger signal variations than the R_2 curves in Figs. 1C and 1D suggesting the susceptibility effect is the primary origin of the contrast. When the two models were fitted to the R_2^* curves, the adjusted R^2 resulted in the same values confirming R_2^* alone cannot distinguish the two models. When the two models were fitted to the R_2 curves, however, much reduced adjusted R^2 values were found in the magic-iso model (-0.75 in ROI1 and -2.49 in ROI2) as compared to the suscep-aniso model (0.77 in ROI1 and 0.89 in ROI2). These results suggest the magic angle is not the origin of the B_0 orientation dependency. BG showed little or no orientation dependency that can be explained magnetic susceptibility anisotropy (maximum R^2 = 0.51). ***Iron extraction***: In both ROIs, R_2^* values were dropped substantially over the iron extraction period. The R_2^* reductions were much larger in BG yielding 30.2 Hz reduction compared to 7.9 Hz in CC (Fig.2). Despite the large changes in R_2^*, ΔR_2^* measured before and after the iron extraction, showed limited change (Table1) suggesting iron is not the origin of B_0 dependent R_2^*. ***Temperature***: Temperature increase from 21°C to 38°C showed decreases in R_2^*. This decrease is consistent with lower R_2^* values observed *in-vivo* than fixed brains at room temperature. The ΔR_2^* value in CC was increased from 4.0±2.9 Hz at 21°C to 5.9±2.6 Hz at 38°C (Table2), which is also consistent with larger ΔR_2^* observed *in-vivo* [9]. These temperature-dependent changes in R_2^* and ΔR_2^* may have originated from changes in magnetic susceptibility and molecular motion.

Conclusion: In this study, we investigated the effects of magic angle and susceptibility on R_2^* and R_2 as well as effects of tissue iron and temperature. The results suggest that the B_0 orientation dependent R_2^* variation is better explained by the magnetic susceptibility-based model with susceptibility anisotropy. Extracting tissue iron did not reduce the orientation dependent R_2^* contrast, suggesting iron is not the origin of the contrast. This leaves susceptibility effects from myelin as the most probable origin of the contrast. Temperature showed large contribution on both R_2^* and orientation dependent R_2^* contrasts, explaining a portion of the contrast difference between the *in-vivo* and *ex-vivo* conditions.

References: [1] Wiggins C, 16th ISMRM,2008,#237 [2] Bender B, NMR Biomed,2010,23,1071 [3] Denk C, NMR Biomed,2011,27, 595 [4] Lee J, Neuroimage,2011,57,225 [5] Lee J, Neuroimage, 2012,59,3967 [6] Wei Li, Neuroimage,2012,59,2088 [7] Fullerton, G.D., Radiology,1985,155, 433 [8] Fukunaga M, PNAS, 2010,107,3834 [9] Wiggins G, 19th ISMRM,2011,#13

Magnetic Susceptibility Induced MR Signal Frequency Shift in White Matter - Experimental Comparison Between Lorentzian Sphere and Generalized Lorentzian Approaches

Jie Luo[1], Xiang He[2], Dmtriy A Yablonskiy[1]

[1]*Radiology, Washington University in St. Louis,* [2]*Radiology, University of Pittsburg*

Background/Purpose:

Phase images obtained by gradient echo MRI provide enhanced contrast of the brain anatomy [1]. Tissue magnetic susceptibility is usually considered as one of the main contributors to this contrast however the relationship between MR signal phase and underlying tissue magnetic susceptibility χ is still subject of debates. The concept of Lorentzian sphere factor allows evaluation of MR signal frequency shift, Δf in the isotropic systems: $\Delta f / f_0 = (4\pi/3)\chi$ [2], where f_0 is a base Larmor frequency. However it cannot explain the absence of phase contrast between WM and CSF [1,3].Recently, it was proposed in [3] that for anisotropic cellular structures such as axons in WM a Generalized Lorentzian Approach (GLA) should be used to account for the longitudinal distribution of magnetic susceptibility inclusions (myelin sheath, neurofilaments, etc.) at the cellular and sub-cellular levels. We are using ex vivo rat optic nerve as a representative white matter model to validate this theory.

Methods:

Optic nerves were obtained from three euthanized rats. One of the optic nerve from each rat was soaked in 1% phosphate buffered saline (PBS), and examined 2~3 hours after death. The other nerve was subsequently fixed with 10% formalin and examined 1~2 days later. They were then suspended in the NMR tube, filled with formalin or PBS, parallel to the tube axis. Experiments were performed on a Varian DirectDrive™ 4.7T MR scanner using a 1.5 cm diameter surface transmit/receive RF coil. Data was collected using multi-echo gradient echo sequence with 4 echoes, 1mm thick slice with 75x75 μm^2 in plane resolution. TR = 170 ms, first TE = 7.4 ms, echo spacing = 13.2 ms, FA = 30 deg, imaging matrix 128x128, 50 averages. The tube was first oriented parallel to the magnetic field B_0 and then rotated several times to subsequent perpendicular orientations. Localized shimming was performed on an imaging slice achieving linewidth ~5 Hz. For each rotation, imaging plane was oriented perpendicular to the NMR tube and the optic nerve.

Frequency shift around optic nerve: The in-plane frequency shift distribution due to the presence of the nerve is defined by Eq.[1], where χ_e is the magnetic

$$(\Delta f / f_0)\big|_{ext} = 2\pi(\chi - \chi_e)\sin^2\alpha(r_0/r)^2\cos(2\vartheta) \quad [1]$$

susceptibility of formalin solution, α- the angle between magnetic field B_0 and nerve direction, θ - an angle in the imaging plane, r – distance from the nerve center and r_0 – nerve radius. Maximum frequency shift outside the nerve was observed when α=90

Frequency shift inside optic nerve: Under Lorentzian sphere approximation, this frequency shift would be given by Eq.[2]. However, the result is different under GLA [4] as described by Eq.[3]. Here the magnetic susceptibility of the optic nerve is separated into two components $\chi = \chi_L + \chi_i$ that represent contribution from the longitudinal (neurofilaments, myelin sheath) and isotropic (cytoplasm) structures. While both components contribute to the external frequency shift, only susceptibility of isotropic component, χ_L, contributes to the frequency shift inside of the nerve. Testing the difference between Eqs. [2] and [3] as compared to the results obtained from Eq. [1], allows distinguishing between Lorentzain sphere and the GLA.

$$\Delta f / f_0\big|_{int} = -2\pi(\chi - \chi_e)\sin^2\alpha + (4\pi/3)(\chi - \chi_e) \quad [2]$$

$$\Delta f / f_0\big|_{int} = -2\pi(\chi_i - \chi_e)\sin^2\alpha + (4\pi/3)(\chi_i - \chi_e) \quad [3]$$

Results:

Figure on the right show phase images of the fixed optic nerve and surrounding formalin obtained at two orientations: 0° (a) and 90° (b). Frequency distribution outside of the nerve is uniform in parallel orientation and displays dipolar pattern in all other cases. The frequency of the surrounding media is obtained by averaging around the nerve along the blue dotted line Fig. b so that frequency bias created by the optic nerve is excluded. The angular dependency of the frequency shift inside optic nerve - frequency shift versus $\sin^2\alpha$– are shown in Plots A & C (Figure at left) for fresh and fixed nerve respectively. The result from fitting Eq.[1] to frequency distribution surrounding optic nerves, are illustrated in Plots B&D. If the Lorenzian approximation would be valid, the magnitude of the slopes in Plots A vs B and C vs D would have been the same, which contradicts with our measurement. To the contrary, Generalized Lorentzian approach provides a consistent explanation of our observations. The estimated χ_L are (-3.4±0.7) ppb for fresh nerve and (-1.6±0.5) ppb for fixed nerve. Anisotropic magnetic susceptibility of the lipid bilayers as part of white matter fiber tracts are also proposed to be important factors that would induce frequency shifts [5,6]. However this effect predicts multi-compartment behavior of MR signal, which is not obvious in our experimental data (plot E on right shows the phase evolution inside the optic nerve along echo time at different α). Experiments that can simultaneously determine contribution from GLA and the susceptibility anisotropy of lipid bilayers are needed.

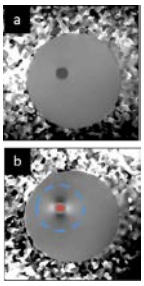

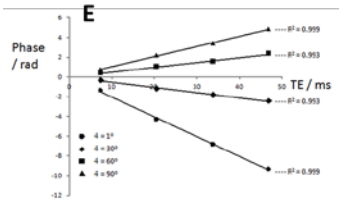

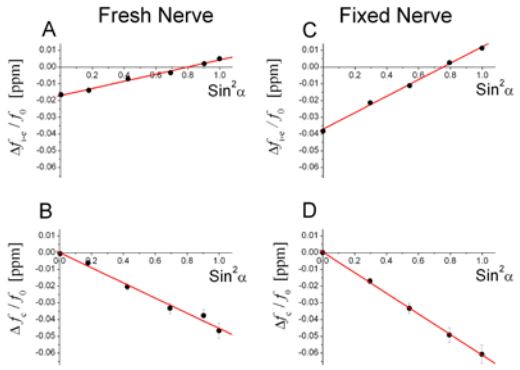

Conclusion: The GLA, accounting for the anisotropy and symmetry of the tissue geometry at the cellular level, provides adequate explanation of the MR frequency shifts in white matter. Freshly harvested and fixed nerves show different results for the χ_L, which calls for caution when projecting findings in phase data of fixed tissue to in vivo or freshly excised tissues.

References: **1**. Duyn, et al., PNAS, 2007, 104, 11796. **2**. Chu, et al., MRM, 1990, 13, 239. **3**. He and Yablonskiy, PNAS, 2009, 106, 13558. **4**. Wharton et al., PNAS, 2012, 109, 18559. **5**. Sukstanskii, et al, MRM, 2013, DOI 10.1002/mrm.24629.

On the role of neuronal magnetic susceptibility and structure symmetry on Gradient Echo MR signal formation

Alexander L. Sukstanskii and Dmitriy A. Yablonskiy
Washington University, St. Louis, Missouri, United States

Background/Purpose: Phase images obtained with gradient-recalled echo MRI provide new contrast in the brain at high magnetic fields that is distinct from that obtained with conventional T1- and T2-weighted images. However, the biophysical origins of the phase (frequency) contrast are not well understood yet. Myelin was proposed as one of the main contributors to MR signal phase in white matter (1-3). A traditional point of view relates MR signal frequency shift due to the presence of local magnetic susceptibility inclusions (iron, proteins, lipids, etc.) to their bulk magnetic susceptibility χ by means of Lorentzian sphere approximation: $\Delta f / f_0 = 4\pi\chi / 3$ (CGS units), where f_0 is the base Larmor frequency. However, as it was proposed in (4) and confirmed by computer simulations in (5), the local contribution to the MRI signal phase does not directly depend on the bulk magnetic susceptibility of the tissue, but on the "magnetic micro-architecture" of the tissue, i.e., on the distribution of magnetic susceptibility inclusions (lipids, proteins, iron, etc.) at the cellular and sub-cellular levels. This effect is especially important for anisotropically arranged cellular structures such as axons. For such structures, the Lorentzian sphere approximation is not valid and should be substituted by Generalized Lorentzian approach (GLA) (4)

$$\Delta f / f_0 = 4\pi \cdot \chi_{iso} / 3 + 2\pi \cdot \chi_L \cdot \sin^2\alpha \qquad [1]$$

where χ_{iso} is magnetic susceptibility of isotropically distributed components of cellular structure, χ_L is magnetic susceptibility of longitudinally arranged components (neurofilaments, myelin sheath , etc.) and α is the angle between $\mathbf{B_0}$ and orientation of neuronal fibers. One of the important consequences of Eq. [1] is anisotropy of phase contrast in WM – correlation between MR signal phase and orientation of neuronal fibers with respect to $\mathbf{B_0}$. Eq. [1] predicts anisotropic behavior of phase contrast due to cylindrical symmetry in the arrangement of WM fibers. Eq. [1] , however, does not take into account anisotropy of WM magnetic susceptibility suggested in (6,7). As shown in (8) for a spherical case and in (9) for a cylindrical case, the presence of a layer formed by highly radially-oriented long-chain lipoprotein molecules, surrounding a central compartment, leads to a non-zero frequency shift in this compartment. The goal of the present communication is to incorporate this effect in the GLA.

Theory We consider WM as a system comprising 3 water-containing compartments: extracellular, intracellular (axons), and myelin sheath. All the frequencies are referenced to the frequency of the extracellular compartment. The myelin sheath is modeled as a set of N ($N >> 1$) concentric lipid layers of thickness d, separated by aqueous layers of thickness d_w (see Figure). In an external magnetic field $\mathbf{B}_0$, the lipid layers are magnetized and induce the secondary inhomogeneous magnetic field. By solving Maxwell equations for this induced field and using results of the GLA (4), we find the following expression for the frequency shift inside the circular cylindrical axon surrounded by myelin sheath:

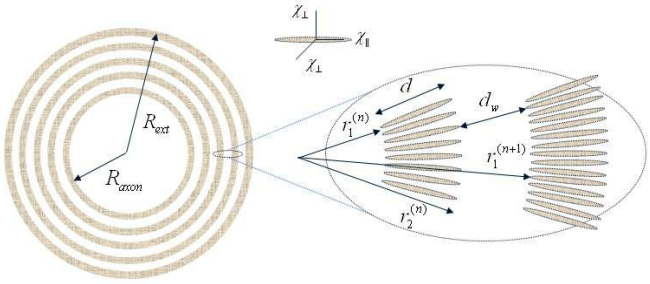

$$\frac{\Delta f_{axon}}{f_0} = 2\pi\sin^2\alpha \cdot \frac{d}{d+d_w}\Delta\chi \cdot \ln\left(\frac{R_{ext}}{R_{axon}}\right) + \left(-2\pi\sin^2\alpha + \frac{4}{3}\pi\right)\cdot \chi_{iso}^{(axon)} \qquad [2]$$

where $\Delta\chi = \chi_\parallel - \chi_\perp$, $\chi_\parallel$ and $\chi_\perp$ are longitudinal and transverse components of volume magnetic susceptibility of long molecules forming lipid layers of myelin sheath, respectively; $\chi_{iso}^{(axon)}$ describes magnetic susceptibility of isotropically distributed structures within the axon, R_{axon} is the axon radius, R_{ext} is the external radius of the myelin sheath. As in (4), longitudinally distributed structures within the axon (e.g., neurofilaments) do not contribute to this frequency shift. Importantly, the first term in Eq. [2] is solely due to the susceptibility anisotropy $\Delta\chi$ within the myelin sheath.

Our theory also predicts that the time course of the gradient echo (GRE) signal from myelin water cannot be described in terms of a simple T2* decay. It is Gaussian for short gradient echo times *TE*, whereas for long *TE* it might exhibit *sinc*-function-type oscillations. The phase of the MR signal from water inside the myelin sheath depends on *TE* nonlinearly. For short *TE*, it can be approximated as a linear function of *TE* with the frequency shift:

$$\frac{\Delta f_{myelin}}{f_0} = 2\pi\sin^2\alpha \cdot \Delta\chi \cdot \left[\frac{1}{2} + \frac{\rho^2 \ln\rho}{(1-\rho^2)}\right], \quad \rho = R_{axon}/R_{ext} \qquad [3]$$

Discussion Our results provide specific dependences of frequency shifts on myelin geometric parameters; hence they might be helpful in deciphering WM tissue microstructure and changes that take place in different diseases. For example, as demonstrated in (5), myelin structural disordering in MS leads to increase in MR signal frequency because of a "redistribution of contributions" to Lorentzian signal frequency shift in Eq. [1] – longitudinally arranged myelin becomes disordered and contributes to isotropic part of magnetic susceptibility. This effect can be enhanced due to an additional frequency shift described by the first term in Eq. [1] because it will also "disappear" if myelin sheath is structurally damaged.

Conclusions Our theoretical results show that both, anisotropy of neuronal tissue "magnetic micro-architecture" and anisotropy of myelin sheath magnetic susceptibility, are important for describing GRE signal phase and magnitude. Our model describes the GRE signal comprising of three compartments – axonal, myelin and extracellular. The myelin-induced frequency shifts reach extrema for axon oriented perpendicular to the magnetic field and are zeros in a parallel case. The myelin water signal is substantially non-T2* type.

References 1. Fukunaga M, et al, PNAS 107 (2010) 3834. 2. Liu CL, et al, Neuroimage 56 (2011) 930. 3. Lodygensky GA, et al, Neuroimage 59 (2012) 1979. 4. He X, Yablonskiy DA. PNAS 106 (2009) 13558. 5. Yablonskiy DA, et al, PNAS 109 (2012) 14212. 6 Lee J, et al, PNAS 107 (2010) 5130. 7. Liu CL. MRM 63 (2010) 1471. 8 . Lounila J, et al, Phys Rev Lett 72 (1994) 4049. 9. Wharton SJ, Bowtell R, PNAS 109(2012) 18559.

Quantitative susceptibility mapping (QSM) forward problem:

Magnetic dipole field, Lorentz correction, susceptibility and chemical shift

Yi Wang
Biomedical Engineering and Radiology, Cornell University, New York, USA

Introduction

The QSM physics is fairly subtle to physicists and likely confusing to non-physicists. We attempt here to clearly define the following key concepts in the QSM forward problem: Magnetic dipole field, Lorentz correction and susceptibility and chemical shift.

Magnetic dipole field

The field of a magnetic dipole can be modeled by a current loop of radius a. At the loop center,

$B = \frac{\mu_0}{4\pi}\frac{I2\pi a}{a^2} = \frac{2\mu_0}{3}m\frac{1}{(4\pi/3)a^3} \to \frac{2\mu_0}{3}m\delta(\boldsymbol{r})$ as $a \to 0$

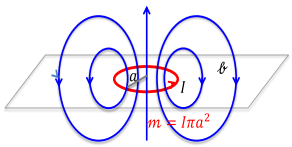

The magnetic field $\boldsymbol{b}(\boldsymbol{r})$ at a location $\boldsymbol{r}$ produced by a dipole $\boldsymbol{m}$ located at the origin $\mathbf{0}$ is:

$$\boldsymbol{b}(\boldsymbol{r}) = \frac{\mu_0}{4\pi}\frac{3(\boldsymbol{m}\cdot\hat{\boldsymbol{r}})\hat{\boldsymbol{r}}-\boldsymbol{m}}{r^3}\Big|_{\boldsymbol{r}\neq\mathbf{0}} + \frac{2\mu_0}{3}\boldsymbol{m}\delta(\boldsymbol{r}).$$

This can be derived from the Maxwell Equation for static magnetism:

$-\nabla^2\boldsymbol{A} = \mu_0\boldsymbol{j}$, $\boldsymbol{A}(\boldsymbol{r}) = \frac{\mu_0}{4\pi}\int\frac{\boldsymbol{j}(\boldsymbol{r}')}{|\boldsymbol{r}-\boldsymbol{r}'|}d^3\boldsymbol{r}'$, $\boldsymbol{m} = \frac{1}{2}\int\boldsymbol{r}'\times\boldsymbol{j}(\boldsymbol{r}')d^3\boldsymbol{r}'$, $\boldsymbol{A}(\boldsymbol{r}) = \frac{\mu_0}{4\pi}\frac{\boldsymbol{m}\times\hat{\boldsymbol{r}}}{r^2}$, $\boldsymbol{b} = \nabla\times\boldsymbol{A}$

Lorentz correction

The magnetic field observed by a proton in MRI does not include contribution from dipoles at the proton location.Classically, no two objects can occupy the same point at the same time, the field experienced by a proton (and other nuclei) at an observation point has to be generated by magnetic moments located away from the observation point. Quantum mechanically, two particles may occupy the same point, i.e., the electron cloud can penetrate into the space occupied by the observing proton with a probability according to the wave function, causing the hyperfine structure in atomic physics. However, it is a good approximation that the electron clouds of the biomaterial being magnetized in the B_0 field of MRI have zero probability to localize in the space of the protons in the nearby free water, which is consistent with classic physics. This is the Lorentz correction for the proton observed field by excluding the source at the proton location:

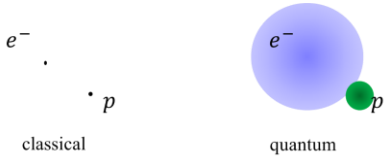

$$\boldsymbol{b}_l = \boldsymbol{b} - \frac{2\mu_0}{3}\boldsymbol{m} = \frac{\mu_0}{4\pi}\int_{\boldsymbol{r}'\neq\boldsymbol{r}}\frac{(\boldsymbol{m}(\boldsymbol{r}')\cdot\widehat{\boldsymbol{r}\boldsymbol{r}'})\widehat{\boldsymbol{r}\boldsymbol{r}'}-\boldsymbol{m}(\boldsymbol{r}')}{|\boldsymbol{r}-\boldsymbol{r}'|^3}d^3\boldsymbol{r}' = \mu_0\boldsymbol{d}(\boldsymbol{r})\otimes m(\boldsymbol{r}).$$

This "no-penetration" correction has been popularly interpreted as subtraction by a sphere of magnetization m, which has a uniform magnetic field $\frac{2\mu_0}{3}\boldsymbol{m}$ inside the sphere. It should be emphasized that in classical electromagnetism, the Lorentz correction is simply the exclusion of two particles at the observation point, and the spherical model may not be necessary.

Susceptibility and chemical shift

For an observation proton, the B_0-perturbed electron cloud of its home molecule generates the magnetic shielding or chemical shift; the B_0-perturbed electron clouds of all surrounding molecules generate the susceptibility field. Let's consider an observation proton (with magnetic moment $\boldsymbol{m}_p$ and mass $\mathfrak{m}_p$) at the origin for simplicity. The total energy (Hamiltonian) of the molecule system with the perturbed electron (spin $\boldsymbol{s}_a$ and mass $\mathfrak{m}$) cloud is the electron energy term (summing over all electrons) plus the proton energy term and the coupling of electron motion with the proton magnetic field,

$$\mathcal{H} = U(r) + \frac{\boldsymbol{p}_p^2}{2\mathfrak{m}_p} - \boldsymbol{m}_p\cdot\boldsymbol{B}_0 + \sum_a\frac{1}{2\mathfrak{m}}\left(\boldsymbol{p}_a + e\left(\frac{\boldsymbol{B}_0\times\boldsymbol{r}_a}{2} + \frac{\mu_0}{4\pi}\frac{\boldsymbol{m}_p\times\hat{\boldsymbol{r}}_a}{r_a^2}\right)\right)^2 + 2\mu_B\boldsymbol{s}_a\cdot\left(\boldsymbol{B}_0 + \frac{\mu_0}{4\pi}\frac{3(\boldsymbol{m}_p\cdot\hat{\boldsymbol{r}}_a)\hat{\boldsymbol{r}}_a-\boldsymbol{m}_p}{r_a^3|_{\boldsymbol{r}_a\neq\mathbf{0}}} + \frac{2\mu_0}{3}\boldsymbol{m}_p\delta(\boldsymbol{r}_a)\right).$$

Here $\frac{e^2}{8\mathfrak{m}}\sum_a(\boldsymbol{B}_0\times\boldsymbol{r}_a)^2$ generates a diamagnetic moment (electron cloud average, weak), $2\mu_B\sum_a\boldsymbol{s}_a\cdot\boldsymbol{B}_0$ generates a paramagnetic moment (only nonzero for unpaired electrons with total angular momentum J, thermal average needed, strong). Together they account for the molecular susceptibility:

$\chi \sim \frac{\mu_0 m}{B_0} = n_I\left(\frac{g^2J(J+1)\mu_B{}^2}{3k_BT} - \frac{N_e e^2 B_0}{6\mathfrak{m}} < r^2 >\right)$.

Proton MR signal comes from the energy term $\propto \mathfrak{m}_p B_0$:

$$-\boldsymbol{m}_p\cdot\boldsymbol{B}_0 + \frac{\mu_0}{4\pi}\frac{e^2}{2\mathfrak{m}}\sum_a\left(\frac{\boldsymbol{m}_p\times\hat{\boldsymbol{r}}_a}{r_a^2}\right)\cdot(\boldsymbol{B}_0\times\boldsymbol{r}_a) \equiv -\boldsymbol{m}_p\cdot(1-\Sigma_d)\boldsymbol{B}_0,$$

which defines the chemical shift tensor

$$\Sigma_d = \frac{\mu_0}{4\pi}\frac{e^2}{2\mathfrak{m}}\langle\sum_a\left(\frac{\mathbf{1}}{r_a} - \frac{\hat{\boldsymbol{r}}_a\otimes\hat{\boldsymbol{r}}_a}{r_a}\right)\rangle.$$

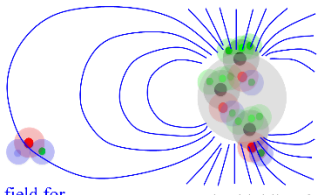

REFERENCES

1. Y. Wang, *Quantitative susceptibility mapping (QSM), tissue magnetism MRI*: http://www.createspace.com, 2013.
2. E. M. Lifshitz and L. D. Landau, *The classical theory of field*, 4th ed. Oxford: Butterworth-Heinemann, 1980.
3. J. D. Jackson, *Classical electrodynamics, third edition*: John Wiley and Sons, inc., 1999.
4. N. F. Ramsey, "Magnetic Shielding of Nuclei in Molecules," Phys. Rev., vol. 78, p. 5, 1950.

Consideration of Echo Dependent Center of k-Space Offsets in Phase Preprocessing

Petra Schmalbrock[1], Grant K Yang[1], Peter Wassenaar[1], Bradley D Clymer[2]
[1]*Departments of Radiology and* [2]*Electrical and Computer Engineering, The Ohio State University*

Background/Purpose:
It was shown that phase preprocessing has profound impact on QSM [1]. High pass filtering [2,3] will alter contrast, thus most recent works use phase unwrapping followed by Bo background phase removal using polynomial fitting [2], calculated Bo maps [4], PDF [5,6] or SHARP [1]. All assume that the measured phase is a sum of $\phi=(\phi_{int}+\phi_{ext})TE+\phi_{RF}+\phi_c$, such that B1 phase effects ϕ_{RF} and constant offsets ϕ_c can be removed by using multi-echo data, which also improve phase SNR [7], and allow for calculation of T2*. We show here that additional TE dependent phase shifts occur, and prevent background field removal from calculated [4] or measured Bo maps and may also degrade other phase preprocessing methods.

Methods:
Single and Multi- 3D gradient echo data of phantoms, 5 control subjects and longitudinal studies of 8 MS patients were acquired at 7T (Philips). The pulse sequence used alternating polarity readout gradients, and was done without flow compensation to allow for 4-6 echoes with TE=3-25ms and short TR/scan times. Multichannel receive coil data with SENSE-factor 2 were reconstructed using scanner software to create magnitude, real and imaginary image domain data. K-space data were generated by inverse FFT in IDL, and the origin of k-space was determined for each echo. Off-center k-space data were shifted in k-space and/or corrected in image space by subtracting a linear slope: $2\pi m_i/N_i$, where m_i is the offset in k-space and N_i is the matrix size in the ith direction. Phase maps were unwrapped using FSL prelude. For background field removal, we tested complex high-pass filtering, subtraction of measured Bo maps and PDF. Linear regression of the phase vs TE, subtraction of image domain phase maps for two TE, and/or complex division of data at two TE were used to remove non-TE dependent phase components, such as B1-field phase.

Results:
Significant shifts of the k-space center in the readout and AP phase encode directions was observed in all in vivo data, but not, or to a lesser extend in phantoms. These phase shifts increased with increasing TE from 1-3 pixels for the 1st echo to 10-15 pixels for the 4th echo (N=448). This creates significant linear phase offsets that are different for different TE, and prevents linear regression and likewise two-echo calculations to remove B1 field effects. Neglecting these linear phase shifts prevents background field removal using measured (or calculated) Bo maps, but also hinders the use of PDF.

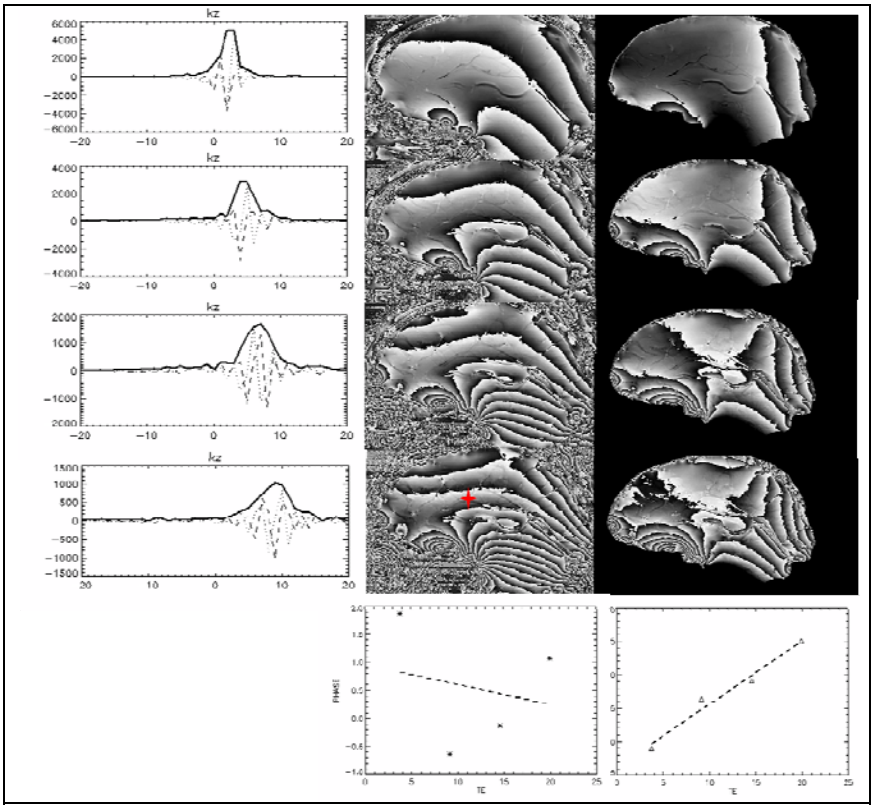

Figure: Shown are (left) the echo dependent k-space offsets in the slice encode direction for these axially acquired image and (middle) the wrapped phase maps. For demonstration purposes, a linear phase shift was applied only along the k_z-slice direction (right). Additional TE dependent shifts are seen in the AP direction. Plots of the phase vs TE for the unwrapped phase (bottom, middle) shows that phase shift correction is necessary for successful linear regression analysis (bottom right).

Conclusion:
Echo dependent 3D center of k-space shifts/ linear image domain phase shifts need to be corrected in phase preprocessing. These shifts may be due gradient imperfections, eddy currents and or patient motion.

References:
[1] Schweser, NeuroImg 11, [2] Rauscher, MRI 08, [3] Ng, MRM 11, [4] Neelavalli, JMRI 09, [5] Liu, NMR Biomed 11, [6] Wharton, MRM10, [7] Gilbert, MRI 12

High-temporal-resolution, simultaneous quantification of intravascular blood flow and oxygen saturation with BRISK k-space sampling

Zachary Rodgers[1], Lohith Kini[1], Varsha Jain[1], Michael Langham[1], Jeremy Magland[1], and Felix W Wehrli[1]
[1]Radiology, University of Pennsylvania, Philadelphia, PA, United States

Background/Purpose: Partial k-space updating strategies, including keyhole and projection-based imaging, allow for rapid, simultaneous quantification of intravascular blood flow and oxygen saturation. Such techniques have been used to quantify the cerebral metabolic rate of oxygen consumption ($CMRO_2$) in response to physiologic stimuli[1] and to characterize the severity of peripheral artery disease in a femoral occlusion-reperfusion model of reactive hyperemia.[2] Because these strategies assume dynamic information is bandlimited in k-space, they are not robust against motion and will tend to bias toward the reference data containing the outer k-space information. BRISK k-space sampling,[3] which updates outer k-space segments at decreasing frequency, has the potential to address these limitations while preserving temporal resolution.

Methods: A dual-echo phase contrast pulse sequence for rapid, simultaneous quantification of blood flow and blood oxygen saturation (OxFlow) was developed (Fig. 1a). Blood flow is quantified from the phase difference between images generated at echo 1 with toggled first gradient moment. Blood oxygen saturation ($\%HbO_2$) is quantified by modeling the vessel of interest as a long paramagnetic cylinder and measuring the phase accumulation of the intravascular signal between images generated at echoes 1&2.[4,5] Sequence parameters are: flip angle 15°, dwell time 15 μs, TE/ΔTE/TR 5.2/7.04/19.2 ms, venc 50 m/s, matrix 208×208x1, resolution 0.85×0.85×5mm.

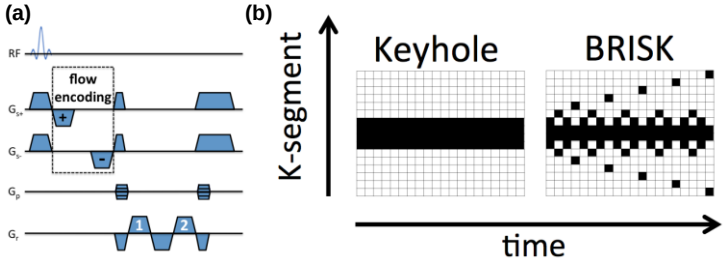

Figure 1: (a) dual-echo OxFlow pulse sequence for simultaneous flow and $\%HbO_2$ quantification; **(b)** schematic of BRISK and keyhole k-space sampling strategies

K-space sampling -- BRISK and keyhole versions of the OxFlow sequence were developed, both with phase encode reduction factors of 4 yielding a temporal resolution of 2 s. In BRISK sampling (Fig. 1b), images are reconstructed by interpolating across time points using the nearest (most recent or future) acquired data at each k-segment, effectively resulting in a sliding window reconstruction with a minimum width of 2 s for the inner 1/8th of k-space and 40 s for the outer half of k-space. In keyhole (Fig. 1b), the inner 1/4th of k-space is continuously updated, with outer k-space supplied from fully sampled reference images acquired at the beginning and end of the scan.

In Vivo Experiments -- To evaluate the sampling strategies, three experiments were conducted in a healthy 27 y/o male volunteer: 1) a motion paradigm with the subject asked to shift his head 1 min into a 2 min acquisition, repeated with BRISK and keyhole sampling at the level of the superior sagittal sinus (SSS), 2) a breath hold paradigm involving two 80 s breath holds, repeated with BRISK and full sampling at the SSS, and 3) a reactive hyperemia paradigm with an inflatable pressure cuff used to occlude femoral blood flow for four minutes before being released, repeated with BRISK and full sampling at the femoral vessels inferior to the cuff. All experiments were performed on a 3T Siemens Trio scanner with an 8 ch. head or 8 ch. knee coil.

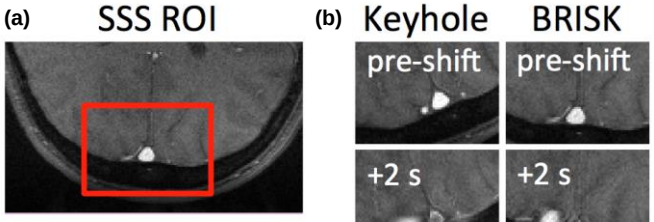

Figure 2: (a) magnitude image of the posterior brain with SSS ROI in red; **(b)** keyhole and BRISK magnitude images of same SSS ROI before, 2 s after, and 20 s after head shift

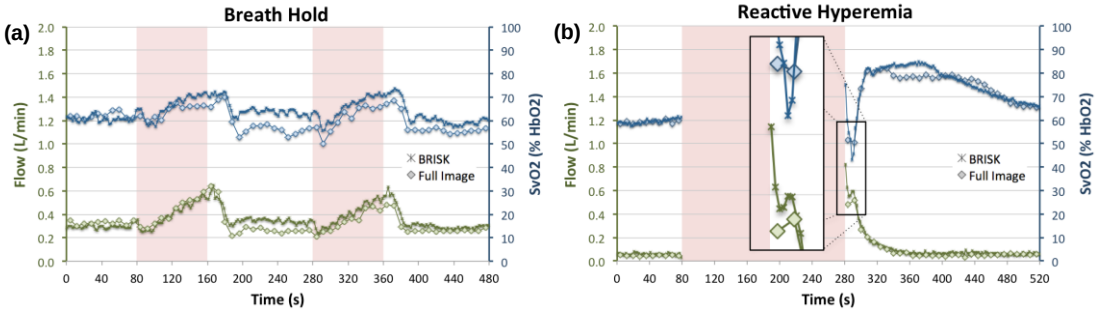

Figure 3: flow and SvO_2 curves for BRISK and full k-space sampling in response to **(a)** breath hold and **(b)** reactive hyperemia with red shading indicating periods of **(a)** breath hold or **(b)** cuff inflation

Results: Fig. 2 shows images of the SSS immediately before, 2 s after, and 20 s after head shift, using keyhole or BRISK k-space sampling. Fig. 3 shows SSS flow and SvO_2 values during breath hold (3a) or reactive hyperemia (3b) with data from BRISK and full k-space acquisitions displayed together.

Conclusions: In Fig. 2, the motion artifact persists in all post-shift keyhole images but quickly resolves in the BRISK images, demonstrating the reduced motion sensitivity of BRISK. In Fig. 3a, flow and SvO_2 increase in response to the hypercapnia and hypoxia that develop during breath hold. In Fig. 3b, the reactive hyperemic response is characterized by a rapid increase in blood flow, causing first a washout of deoxygenated blood followed by a persistent decrease in oxygen extraction. The improved temporal resolution of BRISK results in better resolution of these dynamic physiologic changes compared to full k-space acquisition, especially evident by the sharper peaks in the BRISK acquisition in Fig. 3b, shown in magnification. The data presented suggest BRISK k-space sampling applied to a dynamic OxFlow pulse sequence to be advantageous, allowing a 4x improved temporal resolution compared to full k-space acquisition with less motion sensitivity than keyhole. In ongoing studies, this technique is being used to measure $CMRO_2$ in response to an intermittent apnea paradigm in subjects with obstructive sleep apnea (OSA), with the goal of characterizing OSA disease progression and treatment response and better understanding the basis of OSA-associated neurologic pathology.

References: [1] Rodgers, et al., *ISMRM* 2012. [2] Langham and Wehrli, *JCMR* 13:66 (2010); [3] Doyle, et al., MRM 33:163-170 (1995); [4] Haacke et al., *Hum. Brain Map* 5:341-6 (1997); [5] Fernandez-Seara et al., *MRM* 55:967-73 (2006); **Grant Support: NIH R21-HD069390 / T32-EB000814.**

Multi-echo QSM using flyback readout gradients with z-shimming

Dongyeob Han[1], Yoonho Nam[1], Sung-Min Gho[1], and Dong-Hyun Kim[1]
[1]*Electrical & Electronic Engineering, Yonsei University, Seoul, Korea*

Background/Purpose: Quantitative susceptibility mapping (QSM) provides excellent contrast of susceptibility differences between tissues. However, since it is based on gradient echo (GRE) imaging, the inherent artifact of GRE due to the macroscopic B_0 field inhomogeneity is problematic in QSM. To solve this problem, we propose a 3D multi-echo GRE pulse sequence with z-shim gradient during the flyback gradient portion where normally no information is gained.

Methods: To acquire the macroscopic B_0 field inhomogeneity compensated phase images, z-shim gradients (G_{zs}) were applied between each frequency encoding gradients (G_x) and flyback gradients (Fig 1). The z-shimmed echoes are acquired by adding ADC during flyback gradients. The amount of G_{zs} was set to the maximum phase encoding (G_z) gradient value. The duration (t_{zs}) for z-shim gradient was 0.3 ms, hence the TR increase was only 3 ms. Scan was performed in 3T (Siemens Tim Trio) with 52 slices/slab, voxel size: 1x1x2mm^3, TR: 42.5ms, 1st TE: 3.96ms, ES: 3.215ms, flip angle: 18^o, BW for conventional echo: 240 Hz/Px, BW for z-shimmed echo: 1021 Hz/Px. A total of 11 echoes were acquired (6 conventional echoes and 5 z-shimmed echoes).

Because of the high readout bandwidth during z-shimmed echoes, low pass filtering was applied for denoising. Phase combine process was performed similar to the method proposed in [1]. This method can handle the additional phase difference due to z-shimming, hence undesired additional phase due to both z-shimming and the flyback gradient were successfully removed. We used the PDF method [2] for background field removal and L1 regularized method for QSM reconstruction [3]. For comparison, we applied same phase combine, PDF and QSM process using only the conventional echo data set (i.e., odd echoes).

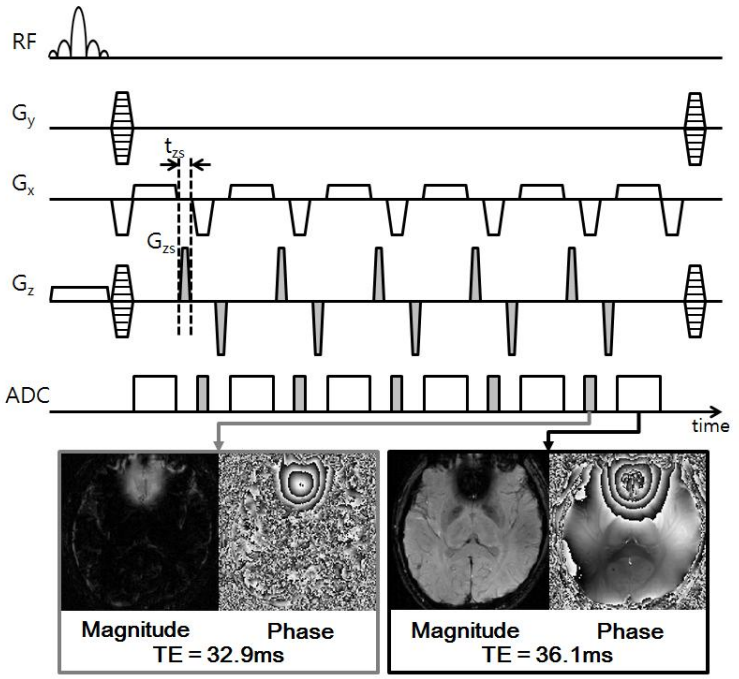

Figure 1. The proposed pulse sequence timing diagram during one TR. G_{zs} represents the applied z-shim gradient and t_{zs} is its duration. Below images are the acquired magnitude, phase images of the z-shimmed echo in flyback gradient and conventional echo.

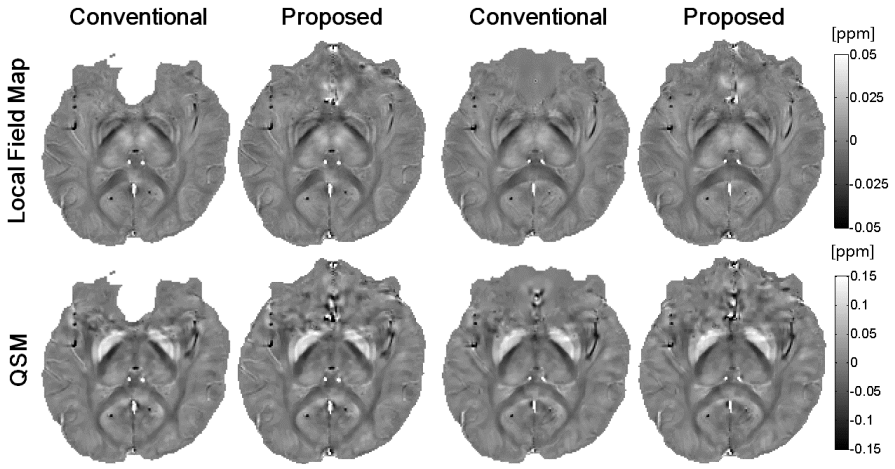

Figure 2. Local field maps (1st row) and QSM (2nd row) of two different slices. Left columns of each set are the result of using conventional echo set (odd echoes) and right columns are the result of using our proposed method.

Results: Below images in Fig 1 shows that the acquired z-shimmed echo successfully restores phase in addition to magnitude signal at the macroscopic B_0 inhomogeneity dominant region. Fig 2 shows in vivo results comparing conventional multi-echo versus our proposed method. In 1st row, the field map after background field removal is presented while QSM results are shown in 2nd row. The hollow regions due to the poor SNR caused by the macroscopic B_0 field inhomogeneity are recovered using our proposed method.

Conclusion: We presented a macroscopic B_0 field inhomogeneity compensated QSM using 3D multi-echo GRE with z-shimming during the flyback gradients. This method would be particularly useful for investigating QSM in the frontal region or subjects who need to increase slice thickness since the effect of the macroscopic B_0 field inhomogeneity becomes worse.

References: 1. D Han et al. ISMRM Saltlake City, USA, 2013; 3852, 2. T Liu et al. NMR in Biomed 2011; 24:1129-1136, 3. B Bilgic et al. Neuroimage 2012; 59:2625-2635

Flow Compensated Quantitative Susceptibility Mapping in Vessel Imaging

Bo Xu[1,2], Tian Liu[2], Pascal Spincemaille[2], and Yi Wang[1,2]
[1]*Biomedical Engineering of Cornell University;* [2]*Radiology of Weill Cornell Medical College*

Purpose: We investigated the phase behavior of moving spins in the multi-echo scan for QSM and proposed a data acquisition and reconstruction method to correct the flow artifacts of vessels in QSM. This enables more accurate vessel susceptibility measurement to allow venous oxygenation level measurement with QSM.

Methods: MR signal equation (considering flow) is written as:

$$s(t) = \int \rho(\mathbf{r}(0)) e^{-i(\psi + \gamma \int_0^t \delta B(\mathbf{r}(\tau))d\tau)} e^{-i\gamma \int_0^t \mathbf{G}(\tau)\bullet\mathbf{r}(\tau)d\tau} d\mathbf{r} = \int \rho(\mathbf{r}(0)) e^{-i\phi 1} e^{-i\phi 2} d\mathbf{r}$$

where $s(t)$ is acquired signal at time t; $\mathbf{r}(t)$ is the spin position; $\rho(\mathbf{r})$ is the spin density at $\mathbf{r}$; ψ is an initial phase after a RF pulse; γ is the gyromagnetic ratio; $\delta B(\mathbf{r})$ is the field inhomogeneity; $\mathbf{G}(\tau)$ is the gradient field at time $0 < \tau < t$. Assume the spin velocity $\mathbf{v}(\mathbf{r}(\tau))$ is constant and $\delta B(\mathbf{r})$ is linearly varying locally, i.e., $\mathbf{r}(\tau) = \mathbf{r}_0 + \mathbf{v}(\mathbf{r}_0)\tau = \mathbf{r}_{TE} + \mathbf{v}(\mathbf{r}_0)(\tau - TE)$ and $\delta B(\mathbf{r}+d\mathbf{r}) = \delta B(\mathbf{r}) + \nabla \delta B(\mathbf{r}) \bullet d\mathbf{r}$. With Taylor expansion of ϕ_1 and ϕ_2 at TE:

$$\phi_1 = \psi + \gamma \cdot \delta B(\mathbf{r}_{TE}) \cdot TE - \tfrac{1}{2} \cdot \gamma \cdot \mathbf{v}(\mathbf{r}_0) \bullet \nabla \delta B(\mathbf{r}_{TE}) \cdot TE^2 \quad [1]$$

$$\phi_2 = 2\pi \cdot \mathbf{r}_{TE} \bullet \mathbf{k}(TE) + \gamma \cdot \mathbf{v}(\mathbf{r}_0) \bullet \mathbf{M}(TE) \quad [2]$$

where $\mathbf{k}(TE)$ is the k-space position and $\mathbf{M}(TE)$ is the first moment of $\mathbf{G}(\tau)$ at time TE. **Based on the equation, we proposed two steps to correct the phase error in QSM. 1) Add first moment nulling gradient to all echoes in the pulse sequence to eliminate the extra phase in ϕ_2 from M(TE)[1,2]. 2) When fitting ϕ_1 and TE, we use a quadratic fit in vessels and linear fit in static regions. Field map δB is the linear term coefficient of the corresponding fit.** This is referred here as adaptive-quadratic fit (or A-Q fit). After obtaining the field map, MEDIN[3] is used to perform the dipole inversion and calculating QSM. A phantom experiment of flowing contrast agent was performed to valid the proposed method. In vivo brain scan (N=8, TE_{first}/TE_{last}/ =3.7/43.8ms, Necho=7, voxel size=0.7×0.7×0.7mm^3) and calf scan (N=5, TE_{first}/TE_{last}/ =3.5/49.0ms, Necho=11, voxel size=1×1×1mm^3) were performed on a 3T GE scanner to demonstrate improved visibility and susceptibility quantification of vessel.

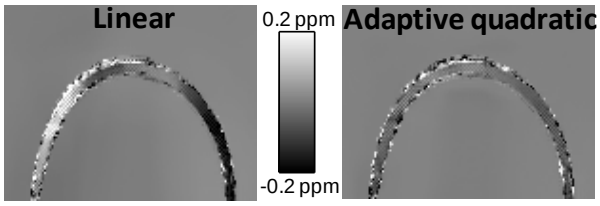

Fig. 1 QSM error map of flowing contrast agent

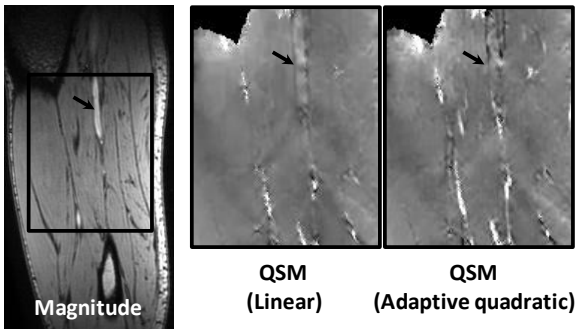

Fig. 2 Calf scan results. Shown are the magnitude and QSM reconstruction images

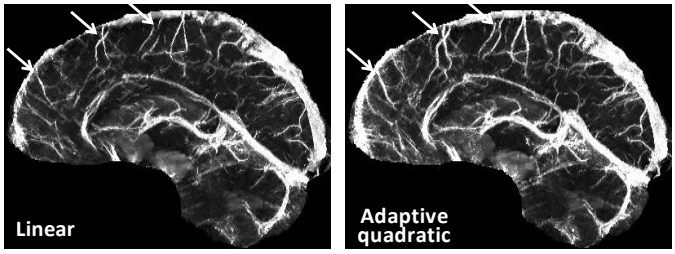

Fig. 3 Brain QSM (Sagittal MIP)

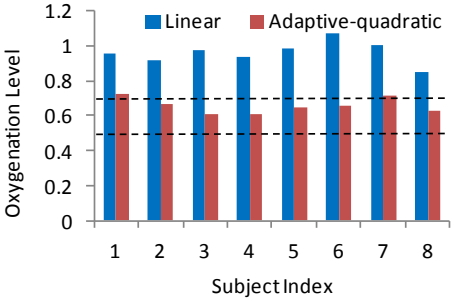

Fig. 4 Venous oxygenation level in 8 volunteers

Results: In phantom experiment, reference QSM is reconstructed with flow turned off. Contrast agent flow at 40cm/s is imaged and QSM reconstructed with linear and A-Q fit are compared with the reference. The error images are show in Fig.1. A-Q fit QSM shows smaller error compared with linear fit. Fig.2 shows a similar comparison in the calf scan. In A-Q fit QSM, more veins are visualized. In addition, the susceptibly of the common peroneal artery (arrow) in A-Q fit QSM is close to the surrounding tissue which agrees with the fact that artery has a high oxygenation level. In contrast, the artery susceptibility in linear fit QSM is higher than surrounding tissue. In the brain scan (Fig.3), A-Q fit QSM exhibits more cortical veins that are connected and with sharp edges (Arrow indicated). Figure 4 shows average venous oxygenation (fO_2) in the cortical veins for each volunteer, according to $\chi_{blood}=Hct(1-fO_2)\Delta\chi_{do}$, where Hct=0.4 and $\Delta\chi_{do}$=2.26ppm. fO_2 from A-Q fit QSM lies in the 50%~70% range from invasive measurements, while fO_2 from linear fit QSM is very likely over-estimated.

Conclusion: A flow-compensated multi-echo sequence with adaptive-quadratic fit is proposed to correct the flow induced field map error in QSM reconstruction. Phantom and invivo experiments demonstrated the improved susceptibility measurement accuracy and QSM image quality. This will enable the measurement of venous oxygenation measurement with QSM.

References: [1] Nishimura et. al, Magn Reson Med 1991;22(2):481-492. [2] Deistung et. al, J Magn Reson Imaging 2009;29(6):1478-1484 [3] Liu et. al, MRM 2013 69(2):467-76

Direct Visualization of Short T_2^* Phase (ViSTa Phase)

Daeun Kim and Jongho Lee
Department of Radiology, Perelman School of Medicine, University of Pennsylvania, USA

***Background/Purpose*:** Myelin water imaging (MWI) measures water signals in the gap of neighboring myelin layers (1). This water has been shown to have shorter T_2 and T_2^* than axonal or interstitial water (1,2). In conventional MWI, T_2 or T_2^* distribution is estimated by fitting multiple exponential functions to multi-echo decays using non-negative least-square (NNLS) algorithm. However, the fitting process is ill-conditioned and the result is sensitive to noise and artifacts (Fig. 2A; ref. 3). Recently, we have proposed a novel approach of directly visualizing short T_2^* signal (ViSTa) (4). This method exploits T_1 difference among the water components (5) and suppresses long T_1 signal using a double inversion RF scheme (Fig. 1). After the suppression, the remaining signal has signal fraction (~ 6%) and T_2^* (~ 10 ms) in the range of myelin water and shows sensitivity to demyelination (Fig. 2C) suggesting the origin of the signal as myelin water. ViSTa images show substantially improved image quality (Fig. 2A *vs*. 2B). In this study, we investigated the characteristics of ViSTa phase. The results demonstrate a good match with a recently proposed hollow cylinder model in white matter (6) confirming the signal origin of ViSTa as myelin water.

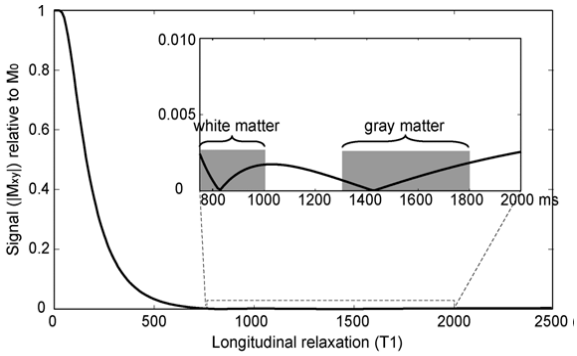

Fig.1: Long T_1 suppression using double inv. RF.

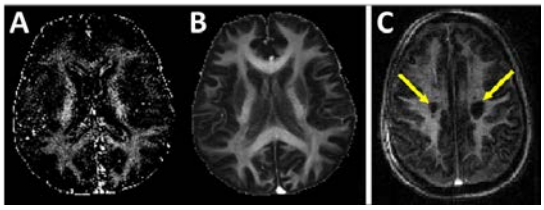

Fig.2: (A) SE-MWI (B) ViSTa (C) MS patient.

***Methods*:** Data were collected at 3T using multi-echo GRE and multi-echo ViSTa with voxel size = 1.72 × 1.72 × 5 mm^3, and TE = 3.11:3:45.11 ms (16 echoes). For GRE, the scan parameters were TR = 97 ms, FA = 28°, and 6 averages. For ViSTa, $TI_1/TI_2/TD$ = 560/220/380 ms (4), TR = 1160 ms, FA = 90°, and 3 averages. After data acquisition, the phase images were unwrapped, and high-pass filtered. Additionally, sixth-order polynomials were fitted and removed to reduce low frequency variation. The magnitude data were analyzed for the multi-component T_2^* distribution using the regularized NNLS algorithm. An ROI was drawn in splenium whose fiber orientation is perpendicular to B_0 field. Myelin Water Fraction (MWF) was calculated ($T_{2\ myelin\ water}^*$ < 20 ms). An averaged ViSTa phase image was generated by averaging the first five echo (phase-corrected) complex images and taking the phase of the image. An averaged ViSTa magnitude image was generated by averaging the first five echo magnitude images.

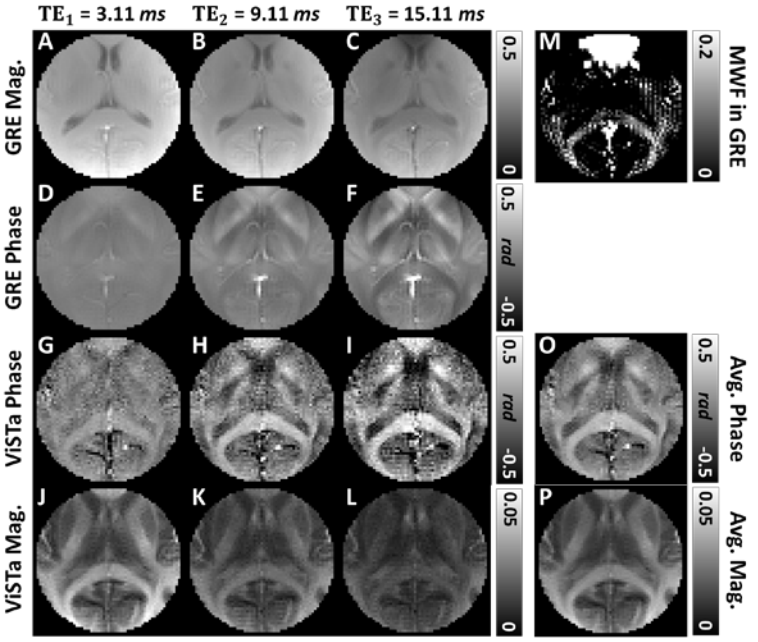

Fig.3: Magnitude images and Phase images in GRE (A-F) and in ViSTa (G-L). (M) MWF in GRE. (O) Avg. ViSTa phase (P) Avg. ViSTa magnitude

***Results*:** Figure 3 shows magnitude and phase images of GRE and ViSTa. The ViSTa phase in splenium reveals positive phase whereas the GRE phase shows negative phase. This agrees with the hollow cylinder model (6). The ViSTa phase increases approximately linearly in the first five echoes but plateaus afterward due to the fast decaying myelin water signal (red line in Fig. 4A). The GRE phase shows a nonlinear phase evolution which was explained by the opposing phase between fast decaying myelin water signal and lasting axonal water signal (6,7) (blue in Fig. 4 B). The T_2^* decays show that the ViSTa signal decays much rapidly than that of GRE (Fig. 4B). The T_2^* distribution confirms the ViSTa signal has only a single short T_2^* component (T_2^* ~ 10 ms) whereas GRE shows two peaks with myelin water fraction of 8.6% (Fig. 4C). These results including the phase results consolidate that the ViSTa signal is from myelin water. The averaged ViSTa magnitude image (Fig. 3P) shows much better image quality than the GRE-MWF map (Fig. 3M). The averaged ViSTa phase (Fig. 3O) shows a large contrast in fibers perpendicular to B_0.

Discussion and Conclusion:

In this work, a phase image from myelin water is generated. The image shows the opposed contrast to GRE phase in fibers perpendicular to B_0 agreeing with the recent model (6). The averaged ViSTa phase image does not require any data fitting and may provide sensitive information of myelination change in white matter. The image (Fig. 3O) suggests that it may have unwanted susceptibility weighting from other origins (e.g. iron).

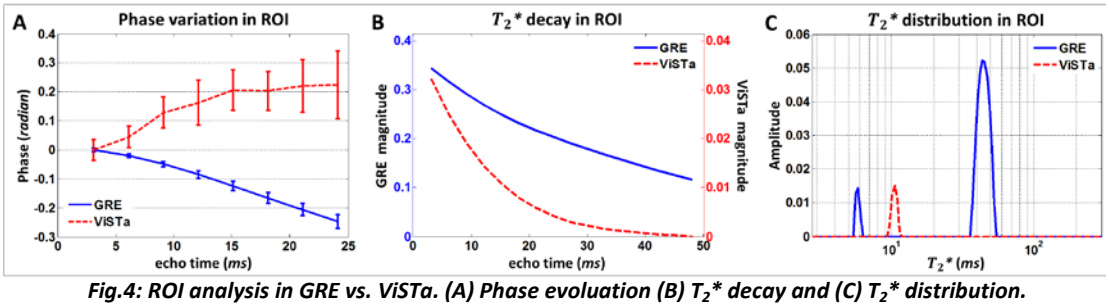

Fig.4: ROI analysis in GRE vs. ViSTa. (A) Phase evoluation (B) T_2* decay and (C) T_2* distribution.

***References*:**[1] Mackay A, MRM, 1994, 673-677 [2] Du YP, MRM, 2007, 865-870 [3] Whittall KP, JMR, 1989, 134-152 [4] Oh SH, ISMRM, 2013, p867 [5] Labadie, MRM 2013, available online [6] Wharton, PNAS, 2012, 18559-18564 [7] Schweser, ISMRM, 2011, p1428

Radio Frequency (RF) effects in Quantitative susceptibility mapping (QSM)

Sung-Min Gho, Narae Choi, Dong-Hyun Kim
Electrical and Electronic Engineering, Yonsei University, Seoul, Republic of Korea

Background/Purpose: Susceptibility imaging techniques including quantitative susceptibility mapping (QSM) relies on the acquired signal phase for image reconstruction. Conventionally, the signal phase is retrieved from the echo signal using a gradient echo sequence. However, it is known that this signal phase also includes the phase due to radio frequency (RF) effects (often called the B1 phase), which in theory cannot be eliminated by harmonic filtering [1]. A simple approach of eliminating this component is to perform a linear extrapolation of the TE=0 phase value using a multi-echo gradient echo (GRE) acquisition [2]. Here, we sought to quantify QSM accuracy in the presence of RF phase effects and determine how much accuracy is gained by removing the phase effects. An electro-magnetic (EM) simulation is performed to estimate the RF phase distribution and its influence on QSM. Furthermore, in vivo studies are done to qualitatively compare the effects of this removal process.

Methods: Using an EM simulation software (REMCOM XFDTD ver.7.1), a 128^3 3D simulation brain model composed of 6 regions (cerebral spinal fluid (CSF), gray matter (GM), white matter (WM), thalamus (TH), hypo-thalamus (HT), and hippo-campus (HC)) was built. The phase effects due to RF pulse were simulated assuming dielectric properties. A 16-rung birdcage head coil was assumed for the simulations. The phase distribution at TE=0 was determined by the EM simulator while phase distribution afterwards were implemented using a Fourier based rapid approach under a given susceptibility distribution (The susceptibility values of the above mentioned regions were assigned 0, 0.02, 0.05, -0.05, 0.035, and -0.005 ppm, respectively) [3]. We used the projection-onto-dipole fields method to remove the background phase [4]. Afterwards, L1 norm regularization method was performed to estimate QSM [5]. Similar procedure was performed for in vivo imaging as well.

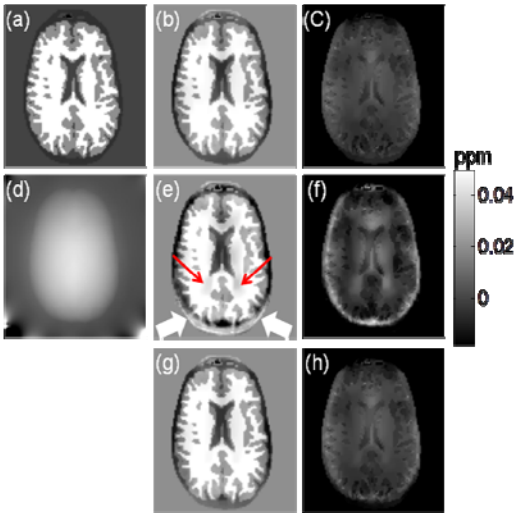

Figure 1: Reconstructed simulation results. (a) reference QSM, (b) reconstructed QSM with TE=0 phase removal, (c) difference map between (a) and (b), (d) TE=0 phase, (e) reconstructed QSM at TE=10ms without TE=0 phase removal, (f) difference map between (a) and (e), (g) reconstructed QSM at TE=40ms without TE=0 phase removal, and (h) difference map between (a) and (g).

In vivo data was collected from a healthy volunteer using 3T Siemens Tim Trio MRI scanner. A 3D multi-echo GRE sequence was applied for obtaining multi-echo QSM data. The scan parameters as follows: TR = 100ms, first TE = 7.1ms, echo spacing = 4.2ms, flip angle = 25^o, FOV = 192 x 192 mm^2, voxel size = 1 x 1 x 1 mm^3, number of slices = 112, number of echo = 7. We used PRELUDE for phase unwrapping [6] and linear extrapolation was used to these unwrapped phase for estimate the TE=0 phase.

For both simulation and in vivo case, the effect on QSM due to the presence of TE=0 phase were investigated by performing QSM with and without TE=0 phase removal.

Results: Figure 1 represents the reconstructed simulation results at different TEs. Reconstruction with the TE=0 phase removed (Fig 1b) shows better results as compared to reconstruction with TE=0 phase added (Fig 1e). The artifacts from remained TE=0 phase are clearly shown in the pointed regions (Fig 1e). As echo time becomes longer (Fig 1g), the TE=0 phase effects reduces in the final image. Susceptibility differences between reference (i.e. no TE=0 phase added) and reconstructed QSM at various regions through different TEs are shown in Fig 2. As expected, reconstruction results at longer TEs have smaller susceptibility differences compare to the results at short TEs since the RF phase effect becomes less dominant. TE=0 phase removed QSM results shows the smallest differences over all regions. The overall differences in the QSM values were within the range of tens of ppb range. Note that due to imperfect QSM reconstruction such as streaking artifacts, even at relatively long TEs susceptibility differences remains compared to true values. Reconstructed QSM using in vivo data also shows similar results compared to simulation phantom (Fig 3).

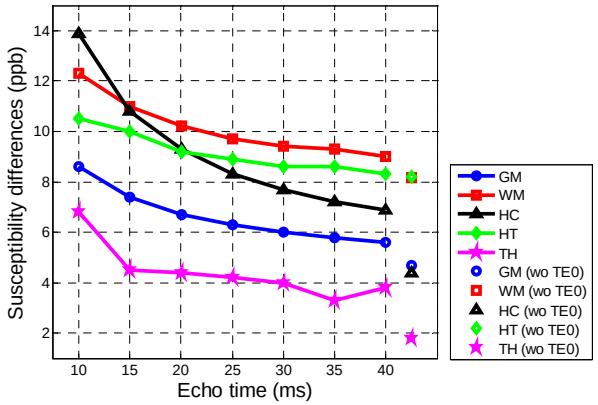

Figure 2: Estimated susceptibility differences at various regions through the different TEs. (The marked values represent the TE=0 phase removed cases)

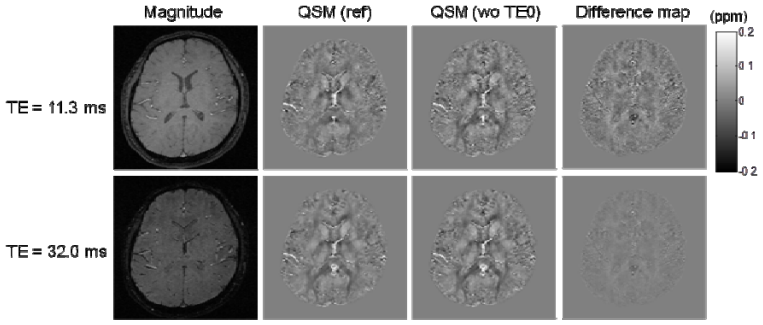

Figure 3: Reconstructed QSM using in vivo data.

Conclusion: We investigated the effects of the RF induced phase in QSM. Under-estimation of the true susceptibility was observed when RF phase effects were present. The TE=0 phase removal can reduce these estimation errors especially at the short TE images. Further methods to optimize the TE=0 phase removal process is needed.

References: 1. F Schweser et al. 1st Intl. Workshop on MRI Phase Contrast and QSM, Germany, 2011. 2. F Schweser et al. NeuroImage 54:2789-2807, 2011. 3. KM Koch et al. Physics in medicine and biology 51:6381-6402, 2006. 4. T Liu et al. NMR in Biomedicine 24:1129-1136, 2011. 5. B Bilgic et al. NeuroImage 59:2625-2635, 2012. 6. M Jenkinson. MRM 49:193-197, 2003.

Simulated and measured T_1, T_2* and Quantitative Susceptibility Maps (QSM) of human brain tissue

C Stueber[1], A Schäfer[1], M Waehnert[1], D Spemann[2], K Reimann[1], S Geyer[1], R Turner[1]

[1] Max Planck Institute for Human Cognitive and Brain Sciences, Dept. Neurophysics, Leipzig, Germany
[2] LIPSION Laboratory, Institute of Nuclear Solid State Physics, University of Leipzig, Leipzig, Germany

Background / Purpose:
We apply Particle-Induced X-ray Emission (PIXE) to reliably and simultaneously map elemental iron, phosphorus and sulphur concentrations in brain tissue. Because most brain phosphorus and a large fraction of brain sulphur is located in myelin, the simultaneous acquisition of these elements can provide a quantitative index of myelin density, given some plausible assumptions. The maps obtained of iron and inferred myelin density allow quantitative testing of the linear dependence between them and T_1, T_2* and QSM tissue contrast [1,2]. These results enable realistic simulation of all three of these tissue contrasts using only the two variables of iron and myelin content.

Methods:
Fixed excised blocks (occipital lobe and precentral/postcentral gyrus) of human cadaver brains were scanned with a 7 Tesla MR scanner (MAGNETOM 7T, Siemens Healthcare Sector, Erlangen, Germany). Scanning was performed with an MP2RAGE sequence (TR=3 s, TE=3.17 ms, TI_1=300 ms, TI_2=900 ms) which provides quantitative T_1 maps, and a FLASH-3D sequence (TR=50 ms, TE=11.1 ms, 0.2 mm isotropic) giving T_2*-weighted complex images. Quantitative maps of T_2* were calculated, and susceptibility maps (QSM) were derived from the phase images. Subsequent to scanning, the blocks were sectioned at 30 µm, and sections were mounted on frames and scanned using PIXE. The element concentrations were calculated using GeoPIXE II. After precise alignment of these PIXE elementary maps with the MR images, SPSS and Matlab code were used to determine their voxel-by-voxel correlations and the linear regression coefficients. Inverting the general linear model, maps of iron and myelin were simulated from the MRI data and compared with the measured elementary iron and inferred myelin map.

Results:
The iron and inferred myelin maps show striking grey-white matter contrast (Fig. 1). The simulated T_1, T_2* and QSM-maps and their measured equivalents are closely similar. Grey/white matter contrast and cortical laminar structure are both well reproduced. Surprisingly, the cortex has a thicker appearance both in acquired and simulated QSM-maps, which may be attributable to iron-rich U-fibers within white matter close to the white-grey matter boundary. The scatter plot shows a good agreement between measured and simulated bulk susceptibility (r=0.812) (Fig. 2).

Conclusions:
We have simulated MR-tissue contrast of T_1, T_2* and QSM maps by a combination of measured iron and inferred myelin maps. The successful simulation demonstrates a linear relationship between magnetic susceptibility and the concentrations of myelin and iron in cortical regions (Fig.2), even though the well-established orientational dependence of magnetic susceptibility was not taken into account.

References:
[1] Rooney et al. 2007, *Magn Reson Med* **57**(2), 308-318
[2] Schweser et al. 2012, *ISMRM* **20**, 409

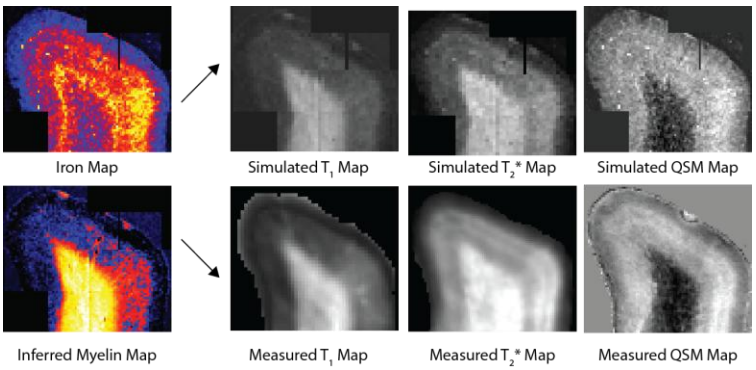

Fig. 1

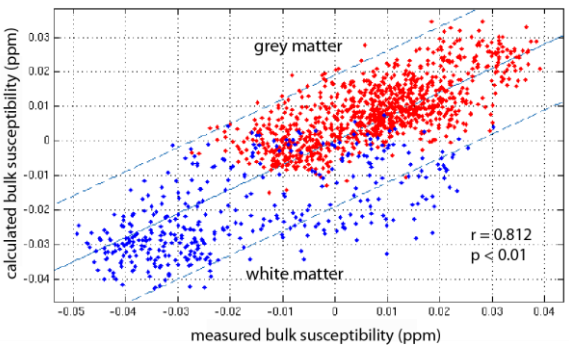

Fig. 2

An Improved Susceptibility Weighted Imaging Method using Multi-Echo Acquisition

Sung Suk Oh[1,2], Se-hong Oh[1], Yoonho Nam[3], Dongyeob Han[3], Randall B. Stafford[1], Jinyoung Hwang[4], Dong-Hyun Kim[3], HyunWook Park[2], and Jongho Lee[1]

[1]*Department of Radiology, University of Pennsylvania,* [2]*Department of Electrical Engineering, KAIST, Korea,* [3]*Department of Electrical and Electronic Engineering, Yonsei University, Korea,* [4]*R&D Group, HME Business, Samsung Electronics, Korea*

Background/Purpose: Susceptibility weighted imaging (SWI) emphasizes the magnetic susceptibility differences between brain tissues [1]. However, the method is also sensitive to non-local susceptibility effects from background field inhomogeneity, particularly in areas near air-tissue interfaces. These large-scale effects often manifest as signal artifacts in areas such as the frontal and temporal lobes. In this article, new acquisition and post-processing approaches are proposed to remove background field inhomogeneity artifacts in both magnitude and phase data for improved SWI coverage.

Methods: For the new SWI, a sequence with *z*-shimming was developed (Fig. 1). The sequence is based on a flow-compensated 3D GRE. Instead of acquiring a single echo, three echoes are acquired. Among them, the 2nd echo is the main echo that has the same TE as conventional SWI. To compensate for flow artifacts, the 2nd echo was flow-compensated. Before the 3rd echo, a *z*-shim gradient (G_c) was applied to compensate for the field inhomogeneity induced signal dropout. ***Phase processing*:** The 2nd echo phase was first unwrapped using Laplacian unwrapping [2] and then fitted with a Gaussian model to remove large scaled field variation. After that, a conventional homodyne high-pass filter was used to refine the phase image. Then a phase mask was generated. ***Magnitude processing*:** The brain was divided into two regions: Region 1 is without the artifacts and Region 2 is with the susceptibility artifacts. An unwrapped phase image was thresholded to divide the regions. For Region 1, the 2nd echo image was used for the magnitude image. In Region 2, the signal was estimated from three echo magnitude images using a signal decay model and iterative fitting [3]. Once the magnitude images were generated in each region, they were summed to generate a final image. Since the magnitude signal drop out area has no phase information, the resulting SWI region has no reliable phase mask. In our method, the phase mask in this area was separated generated from the 1st echo phase using the same phase processing. Then, this phase mask was used for Region 2 whereas the phase mask from the 2nd echo was used for Region 1. Finally, SWI image was calculated from the multiplication of the magnitude image and 4th power of the phase mask. The MR images were obtained at a 3T scanner (ISOL, Korea). The imaging parameters were as follows: TR = 50 ms, TE = [8.7, 25.0, 32.1] ms, matrix size = 220 x 220 x 48, FOV = 220 x 220 x 57.6 mm^3. For the comparison, a conventional and phase artifact corrected SWI images were generated using the magnitude and phase images from the 2nd echo.

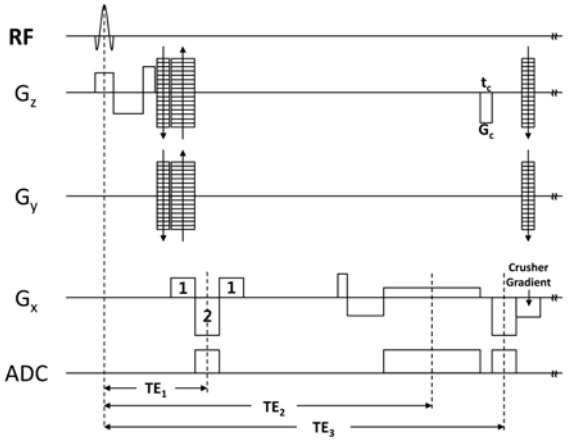

Figure 1 Proposed SWI sequence

Results: Figure 2 shows SWI and mIP representative images using the conventional (left column), the phase-artifact corrected (middle column) and the proposed (right column) methods. The SWI and mIP images generated by the conventional method show substantial artifacts in the frontal and temporal brain regions (left column of Fig. 2). Once phase artifacts are removed using the proposed phase processing, artifact regions are reduced. However, signal dropout in the magnitude images persists resulting in the artifacts in the SWI and mIP images (middle column of Fig. 2). These artifacts are successfully removed in the SWI and mIP images generated by the proposed method with magnitude compensation as shown in the right column of Fig. 2. Outside of these artifact-prone regions, all three methods show similar SWI contrast. In the proposed method, large veins that are invisible in the conventional method are visible (red arrow).

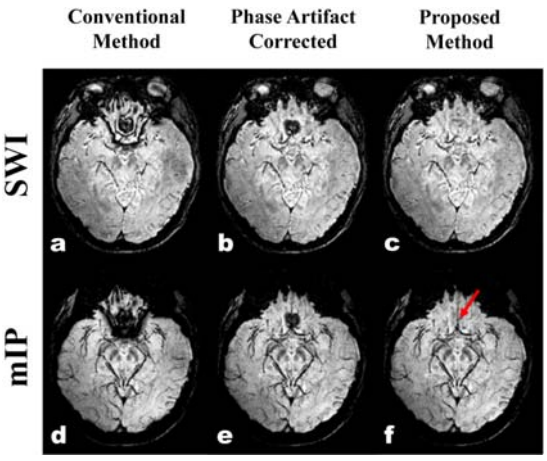

Figure 2 SWI and mIP images. SWI images (a) and mIP images (d) from the conventional method. Phase artifact corrected SWI images (b) and mIP images (e). The proposed phase post-processing method was used for the phase artifact correction. SWI images (c) and mIP images (f) generated by the propose method. Additional veins are visible in the proposed method (red arrow)

Conclusion: The proposed method reduces image artifacts in SWI improving the spatial coverage. Compared to other SWI approaches suggested to compensate for field inhomogeneity artifacts, our method compensates not only phase artifacts but also magnitude artifacts. This technique may have important applications in detecting hemorrhage and cerebrovascular disease in the frontal and temporal lobes.

References: [1] Haacke et al., MRM, 2004, [2] Schofield and Zhu, Opt Lett, 2003, [3] Nam et al., NeuroImage, 2012

Robust high resolution MR phase measurement

Joseph Dagher[1] and Ali Bilgin[1,2]
[1] Department of Electrical and Computer Engineering, The University of Arizona, Tucson, AZ,
[2] Department of Biomedical Engineering and the BIO5 Institute, The University of Arizona, Tucson, AZ

Background/Purpose: Numerous imaging methods require accurate quantitation from MR phase in order to extract important information about the underlying physiology. Whether the MR images are acquired at one or multiple echo times [1], there exists inherent ambiguities about the desired phase signal. A common class of "spatial phase regularization" algorithms, such as phase unwrapping and de-noising, attempt to resolve these ambiguities. Phase unwrapping attempts to recover ambiguities due to large phase build-up whereas de-noising methods attempt to recover those ambiguities due to small phase accumulation. Ultimately, these spatial regularization methods reduce the resolution of the underlying phase measurements [2]. In a recently published paper [3], we rigorously formulated the problem of phase estimation and proposed a solution which achieves robust estimates over large dynamic range of phase values, at high spatial resolutions. Our in vivo results demonstrated improved performance as compared to existing techniques. A key feature of our proposed method (Maximum AmbiGuity distance for Phase Imaging, MAGPI) is that it does not require the use of any spatial-domain processing, such as phase unwrapping or smoothing.
The purpose of this abstract is to extend MAGPI to handle (a) rapid Multi Echo Gradient Echo (MEGE) sequences and (b) full flow compensation. In these scenarios, the challenges of phase quantitation are exacerbated by longer echo time spacings (due to MEGE and flow compensation) and lower SNR relative to single GRE acquisitions. This contribution is an important step to transition our fundamental treatment of the MR phase measurement problem into scenarios relevant to QSM and SWI.
Theory: The theory behind our method could be summarized as follows. The measurement obtained using a fully flow compensated spin-warp sequence at a channel (receiver) element c could be written as:

$$g(x,y;c,\mathrm{TE}_k) = f^c(x,y;\mathrm{TE}_k)\exp\left\{i(\phi_0^c(x,y)+2\pi\Delta B(x,y)\mathrm{TE}_k)\right\}+\mathbf{w}(x,y), \quad (1)$$

where the magnitude term $f^c(x,y;\mathrm{TE}_k)$ is the spin density at echo time TE_k modulated by the sensitivity of channel c, $\Delta B(x,y)$ is the field offset value (in Hz) at location (x,y) and $\phi_0^c(x,y)$ is the spatially-varying phase offset for channel c. The noise random variable (RV) $\mathbf{w}(x,y)$ is complex with $w(x,y) = w_R(x,y) + iw_I(x,y)$, $w_R, w_I \sim \mathcal{N}(0,\sigma_w)$. We define as the "phase signal" $\Delta B(x,y)$ the offset that results from any deviation from the desired magnetic field, which is caused by B0-field inhomogeneity, chemical shift or susceptibility-induced inhomogeneity. The phase signal estimate computed from two echoes TE_0 and TE_1 can be written as:

$$\widehat{\Delta B}_{0,1} = \frac{\angle\left(\sum_c g(x,y;c,\mathrm{TE}_0)(g(x,y;c,\mathrm{TE}_1))^*\right)}{2\pi\Delta\mathrm{TE}_{0,1}}, \quad (2)$$

where $\Delta\mathrm{TE}_{0,1} = \mathrm{TE}_1 - \mathrm{TE}_0$ is the echo spacing. We can easily show that the overall error in this estimate can be written as $\mathbf{E}_{0,1} = \widehat{\Delta B}_{0,1} - \Delta B = \frac{\mathbf{n}_{0,1}+(\boldsymbol{\xi_1}-\boldsymbol{\xi_0})/2\pi}{\Delta\mathrm{TE}_{0,1}}$ where $\boldsymbol{\xi_i}$ is the noise random variable (in Hz) at echo time TE_i, and $\mathbf{n}_{0,1}$ denotes a phase wrapping integer which is non-zero whenever $2\pi(\Delta B\Delta\mathrm{TE}_{0,1} + \boldsymbol{\Delta\xi_{0,1}})$ falls outside $[-\pi,\pi)$. The probability density function (PDF) of $\mathbf{E}_{0,1}$ completely describes the uncertainty (ambiguity) about the original phase slope value. We can show that this PDF is given by: $P(\mathbf{E}_{0,1}=e) = \sum_k \left(f_{\xi_0}(e-\frac{k}{\Delta\mathrm{TE}_{0,1}}) * f_{\xi_1}(e-\frac{k}{\Delta\mathrm{TE}_{0,1}})\right)\Pr(\mathbf{n}_{0,1}=k)$, where * denotes a convolution operation, f_{ξ_i} is the PDF of the noise at echo time TE_i and $\Pr(\mathbf{n}_{0,1}=k)$ is the probability of obtaining a given wrapping integer k when the echo spacing is $\Delta\mathrm{TE}_{0,1}$. We derive a closed form expression for the noise and phase wrapping PDFs but omit them here for space constraints. The PDF $P(\mathbf{E}_{0,1}=e)$ (which we refer to hereafter as the Phase Ambiguity Function, PAF) describes the ambiguity about the original phase value when estimated from echoes TE_0 and TE_1. The PAF captures the underlying trade-off in the choice of echo times: a large echo time spacing gives rise to increased wrapping error contributions, while a short echo time spacing suffers from increased noise amplification. We can show (proof in [3]) that this ambiguity and its trade-offs can be resolved with the acquisition of a third echo, TE_2. Repeating the same analysis as above using echo pair (TE_0,TE_2), we obtain a second PAF. We argue that if the PAFs were completely identical, then this third acquisition would add no additional information about the phase. Thus, we formulate an optimization routine which choses three echo times such that the resulting PAFs are maximally distinct. We formulate this problem numerically, using the derived closed-form PAF expressions. This optimization is run offline, and only requires prior-knowledge of the maximum dynamic range of the phase signal and the minimum expected SNR in the image. It is important to emphasize that the optimized echo times should be constrained to possess a minimum spacing, as achievable with the sequence utilized. In our case here, the minimum echo time spacing required by the high resolution, flow compensated MEGE sequence is large enough to violate the aliasing cutoff needed for measuring a phase signal with a modest dynamic range (e.g., $\pm$50Hz). This highlights the capability of our novel paradigm which handles this challenge by "engineering" the aliasing error in the PAFs so as to be uniquely invertible. We presented in [3] an example of a straightforward numerical estimation method which is able to efficiently disambiguate the original phase value from the images acquired at the 3 optimal echo times. The estimation algorithm only requires prior-knowledge of the designed PAFs.
Methods: We present data collected on a 3T Siemens Trio scanner from a healthy human volunteer using a 2D flow compensated MEGE sequence. We acquire three echoes at an in-plane resolution of $0.68\times 0.68\mathrm{mm}^2$, 1.5mm slice thickness, bandwidth of 430Hz/pxl, FOV of 220mm, and TR of 361ms. The minimum echo spacing allowed by such parameters is 9.64ms. In accordance with this constraint, our MAGPI paradigm chooses the optimal echo set of TE_0 = 15.58ms, TE_1 = 5.92ms and TE_2 = 27.68ms. **Results:** Figure 1a shows the field map obtained in one slice using our method, MAGPI. As a reference, we acquired 12 individually flow compensated GRE images closely separated by 1.5ms. We then applied a Least Squares (LS) fit for each voxel, across the temporal direction. The resulting offset map is shown in Figure 1b. Both Figures 1a and 1b are scaled to display the range of $\pm$200Hz. Magnified and windowed ($\pm$20Hz) portions of these figures are shown in Figures 1c and 1d, respectively. We also plot in Figure 1e two profiles through the brain for each of MAGPI (red line) and the 12-point LS method (blue and green lines). We immediately note the following: (1) overall, MAGPI achieves a similar $\Delta B(x,y)$ estimate as compared to the reference scan, (2) the MAGPI map is more robust (less noisy) than the reference scan (Figures 1c and 1d), (3) MAGPI is able to image high resolution features at high contrast (Figure 1e, Profile 2), (4) the MAGPI map was generated using only 3 echoes from an MEGE sequence, which is substantially faster than the 12 GRE echoes obtained with the reference scan. We should also emphasize that, despite using echo times spaced by 9.64ms, MAGPI was able to reconstruct phase signal values in a range up to $\pm$200Hz without the use of any spatial phase unwrapping routines. Traditionally, a 9.64ms echo spacing constrains the phase signal's dynamic range within $\pm$52Hz before incurring phase aliasing. This implies a gain in dynamic range of a factor of 4 with our method.
Conclusion: We introduced a novel framework for robust estimation of phase signals over a large dynamic range, under extreme constraints imposed on minimum echo spacing by flow compensation and rapid MEGE acquisitions. We observed that our paradigm substantially improves the accuracy of the estimated signal, particularly at high resolutions. No phase unwrapping, smoothing, or regularization was employed with MAGPI. We plan to investigate the impact of such benefits on SWI and QSM studies. **References:** [1] Robinson S, Grabner G, Witoszynskyj S, and Trattnig S, MRM 2011, 65: 16381648. [2] Funai AK, Fessler JA, Yeo DTB, Olafsson VT, and Noll DC, IEEE Trans Med Imaging 2008, 27: 1484-1494. [3] Dagher J, Reese T, and Bilgin A, MRM 2012, (early view).

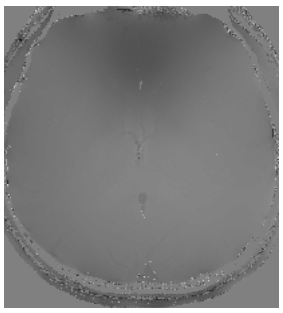
Fig. 1a - MAGPI

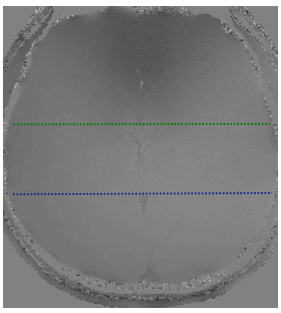
Fig. 1b - 12-echo LS


Fig. 1c - MAGPI


Fig. 1d - 12-echo LS

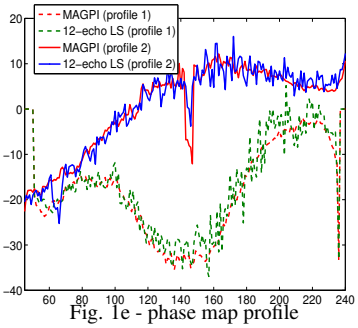

Fig. 1e - phase map profile

Enhancement of Brain Structures by Combining Quantitative Susceptibility Mapping and Relaxometry

Andreas Deistung, Ferdinand Schweser, Jürgen R. Reichenbach
Medical Physics Group, IDIR I, Jena University Hospital – Friedrich Schiller University Jena, Jena, Germany

PURPOSE: Multi-echo gradient-recalled echo (GRE) sequences provide quantitative information about the effective transverse relaxation rate, R_2^*, (magnitude of the signal) and magnetic field perturbations caused by the tissue susceptibility distribution (phase of the signal). They also reveal information of the magnitude signal immediately after the rf-pulse, S_0, which depends on tissues' spin density and T_1 as well as on the flip angle.[1] The complex GRE information is, for instance, employed in susceptibility weighted imaging (SWI), a heuristic approach for combining magnitude and phase of the GRE signal into a composite image to enhance the contrast of cerebral veins and brain lesions.[2,3] While SWI is today established in hospitals throughout the world a considerable drawback of SWI is that the visualization of veins depends on the orientation of the vessels with respect to the main magnetic field. This is reflected in sometimes ambiguous representations of veins, in particular in sagittal and coronal views, and impedes accurate segmentation of cerebral veins and quantification of their radii. Automatic generation of 3D models of the venous vasculature based on SWI is also hampered because the inter-hemispheric fissure is hypointensely displayed, just like veins. In this contribution, we present a supervised approach for creating image contrast that enhances specific structures of interest. We apply linear discriminant analysis (LDA) to optimally combine multiple image contrasts generated from complex-valued multi-echo GRE information (magnetic susceptibility, R_2^*, and S_0) to yield a novel contrast with increased venous vessel contrast.

THEORY: LDA[4] is a technique for feature extraction and dimension reduction. LDA projects data onto a lower-dimensional vector space such that the ratio of the between-class distance to the within-class distance is maximized, thus achieving maximum discrimination. Volumes of interest (VOIs) were identified in 4 subjects and the means and standard deviations of magnetic susceptibility, R_2^*, and S_0 were assigned as features. VOIs were divided into two classes: vein (central and cortical veins, sinus rectus) and remaining tissue (arteries, cerebrospinal fluid (CSF), white matter (WM), cortical gray matter (GM), deep GM structures, interhemispheric fissure). LDA was applied to these data (training step) and the resulting base vectors were then applied to other GRE data (evaluation step) to generate composite images.

METHODS: Dual-echo GRE data sets (TOF-SWI-sequence,[5] $TE_1/TE_2/TR/FA/TA$=3.5 ms/25.4ms/15°/13:31min:sec, voxel size = 0.45mm × 0.45mm × 1.2mm) were acquired from six healthy volunteers on a 3T MR scanner. Four data sets were employed to find the optimal base vectors using LDA (training step) which were then evaluated on the remaining two data sets (evaluation step). Maps of R_2^* (in ms^{-1}) and S_0 were computed using mono-exponential fitting of the magnitude signal decay. Aliasing in phase images was resolved by 3D phase unwrapping[6] and background phase contributions were eliminated with the SHARP method.[7] Homogeneity enabled incremental dipole inversion[8] of the background-corrected phase images yielded quantitative susceptibility maps. To reduce inter-subject variability, the magnetic susceptibility was normalized with respect to frontal white matter ($\Delta\chi$), and the range of S_0 values was adjusted to be between 0 and 1. For comparison, SW images were created from magnitude and phase images according to the SWI standard processing scheme (i.e., 4-fold multiplication of the linearly weighted high-pass filtered phase images with the magnitude images).[2,3] Venous vessel visibility was assessed by computing the contrast-to-noise ratio (CNR) of 5 veins for the different contrasts according to $CNR = |(S_v - S_t)/\sigma_t|$, where S and σ denote the mean and standard deviation of a VOI and the subscripts v and t indicate whether the VOI represents a vein or tissue.

RESULTS: Mean R_2^* values were plotted against mean magnetic susceptibility differences (Fig. 1). Although the majority of veins were characterized by high susceptibilities, certain deep GM structures (globus pallidus, substantia nigra, and red nucleus; black points in Fig. 1) yielded similar susceptibility and R_2^* values, resulting in a slight overlap between the two classes. LDA yielded maximum separation if $\Delta\chi$ and R_2^* were merged according to: 0.447 $ppm^{-1} \cdot \Delta\chi + 0.894\ s \cdot R_2^* - 0.049$ and if $\Delta\chi$, R_2^*, and S_0 were combined according to 0.325 $ppm^{-1} \cdot \Delta\chi + 0.907\ s \cdot R_2^* - 0.27 \cdot S_0 - 0.013$. The LDA-combined images are presented in Fig. 2e and f. In these images the apparent intensity of CSF increased (blue arrow in Fig. 2) and of highly myelinated regions decreased (red arrow in Fig. 2) compared to the magnetic susceptibility map. Furthermore, the inter-hemispheric fissure was displayed isointense on LDA-combined images (black arrows in Fig. 2e and f). The sinus veins were accurately displayed in the composite image, whereas hypointensities around veins were observed in SW images (red arrows in Fig. 3). The average CNR was highest for the LDA-combined image based on $\Delta\chi$, R_2^*, and S_0 (CNR=6.46). The CNR of the remaining contrasts were: 4.70 for magnetic susceptibility, 4.46 for R_2^*, 4.31 for the magnitude, 5.12 for SWI, and 6.01 for the LDA-combined data based on $\Delta\chi$ and R_2^*.

DISCUSSION: Base vectors derived from discriminant analysis of training data allowed the combination of multiple contrasts into composite images that yielded increased venous contrast compared to the magnetic susceptibility and R_2^* maps alone. The base vectors can also be transferred to data collected with different acquisition parameters because magnetic susceptibility is nearly independent of acquisition parameters and the dependence of acquisition parameters on R_2^* can be considered. The venous contrast, in particular in deep GM regions, may be further improved by incorporating additional features obtained after post-processing of GRE data (e.g., application of vessel enhancing diffusion filtering[10] to magnetic susceptibility images) or additional MRI scans as well as employing non-linear discriminant analysis.[11] The presented approach may be applied as a pre-processing step in order to segment veins from GRE data using image-based approaches, such as active contours, or the base vectors obtained by discriminant analysis may be interpreted as classifier.

CONCLUSION: Discriminant analysis provides base vectors for optimized combination of multiple contrasts. The technique can be easily adjusted to emphasize other tissue properties in composite images by changing the class definition in the training step to yield, e.g., improved delineation of pathologies such as cortical lesions.

REFERENCES: [1] Haacke EM et al. *Magnetic Resonance Imaging: - Physical Principles and Sequence Design*. 1999. John Wiley & Sons, Inc. [2] Reichenbach JR et al. *Radiology* 1997;204(1):271-7. [3] Haacke EM et al. *Magn Reson Med*. 2004;52(3):612-8. [4] McLachlan GJ. *Discriminant Analysis and Statistical Pattern Recognition*. 1992. John Wiley & Sons, Inc. [5] Deistung A et al. *J Magn Reson Imaging*. 2009;29(6):1478-84. [6] Abdul-Rahman HS et al. *Appl Opt*. 2007;46(26):6623-3. [7] Schweser F et al. *NeuroImage*. 2011;54(4):2789-807. [8] Schweser F et al. *NeuroImage*. 2012;62(3):2083-100. [10] Mannieshing R et al. *Med Image Anal*. 2006;10(6):815–825. [11] Baudat G and Anouar F. *Neural Computation*, 12(10):2385–2404, 2000.

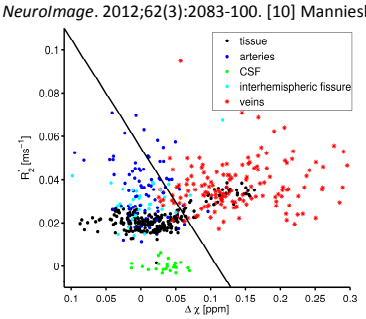

Figure 1: *R_2^* plotted against magnetic susceptibility differences (Δχ) with respect to frontal WM. The principle axis obtained by LDA (black line) provides the best separation between the two groups (veins vs. remaining tissue [tissue, arteries, CSF, inter-hemispheric fissure]).*

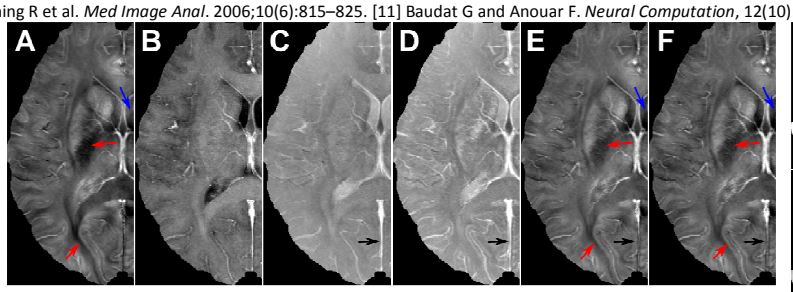

Figure 2: *Transverse average intensity projections over 6 mm of magnetic susceptibility maps (a), R_2^* maps (b), magnitude (c; TE=25.4ms), SWI (d), composite image based on magnetic susceptibility and R_2^* (e), and composite image based on magnetic susceptibility, R_2^* and S_0 (f), respectively. Blue and red arrows indicate CSF and regions with high myelin content, respectively. The black arrows point to the inter-hemispheric fissure that is isointense on the composite images (e,f) and hyperintense on the inverted SWI (d). For ease of comparison the contrast of the magnitude and SW images are inverted.*

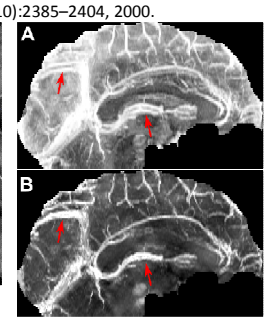

Figure 3*: Sagittal maximum intensity projection across 12 mm at the level of inter-hemispheric fissure of inverted SWI and the LDA-combination based on magnetic susceptibility, R_2^* and S_0 are shown in (a) and (b).*